Brain MR Image Segmentation Using Markov Random Field Model and Tabu Search Strategy

Thesis

Submitted in Partial Fulfillment of the Requirements
for the Degree of

DOCTOR OF PHILOSOPHY

by
DIPTI PATRA

Thesis Advisor
Prof. P. K. Nanda

Department of Electrical Engineering

NATIONAL INSTITUTE OF TECHNOLOGY
ROURKELA

2005

Certificate

This is to certify that the thesis entitled "**Brain MR Image Segmentation Using Markov Random Field Model and Tabu Search Strategy**", being submitted to the National Institute of Technology, Rourkela, India by **Dipti Patra** for the award of the degree of **Doctor of Philosophy** is a bonafide research work carried out by her under my supervision and guidance. To the best of my knowledge this work has not been submitted in part or full to any other university or institution for the award of any degree.

Rourkela
Date:

Dr. P.K.Nanda
(Professor)
Department of Electrical Engineering
National Institute of Technology
ROURKELA

Abstract

The problem of image segmentation has been investigated with a focus on brain Magnetic Resonance (MR) image segmentation. Brain tissue is a complex structure and hence proper diagnosis of many brain disorders greatly depends upon accurate segmentation of the three brain tissues namely, white matter (WM), grey Matter (GM), and cerebrospinal Fluid (CSF) in brain MR image. The prime objective of this thesis work is to devise novel strategies and methodologies for an automated brain MR image segmentation scheme.

This problem has been addressed in the literature, still many key open issues remain to be investigated. As an initial stride in this direction, brain MR image segmentation is achieved in supervised framework. The problem is formulated as a pixel labeling problem. Gauss Hidden Markov Random Field (GHMRF) models have been used to model the tissue class of the observed degraded image. The *a priori* class labels are modeled as Markov Random Field (MRF) model. These MRF and GHMRF model parameters are assumed to be known in the supervised framework. The image label estimation problem is cast in Bayesian framework using *Maximum a Posteriori* (MAP) criterion. A Hybrid Tabu Search (HTS) algorithm is proposed to obtain the MAP estimates of the image labels and thus accomplish segmentation. The performance of the algorithm is compared with that of Simulated Annealing (SA) and Iterated Conditional Mode (ICM) algorithm.

In order to make the scheme viable from a practical stand point, the problem is addressed in a unsupervised framework. In this framework, it is assumed to have no knowledge of number of classes, the model parameters and the image labels. In this work, the number of classes, GHMRF model parameters and the image labels are assumed to be unknown. But, it is assumed to have the *a priori* knowledge of MRF model parameters used to model the unknown class labels. This problem, being

an incomplete data problem, is cast in Expectation-Maximization (EM) framework. Earlier scheme proposed by Zhang *et al.* [95] is found to be sensitive to the initial set of model parameters. This has been overcome by proposing a Tabu-EM (TEM) algorithm that does not require to have a proper choice of initial parameters. Hence, the algorithm could be successfully tested with an arbitrary set of initial model parameters. The results obtained by the proposed algorithm are compared with that of Zhang's approach and the results are quite comparable to the later ones.

A new notion of model learning based image segmentation is introduced. The unknown class labels are modeled as MRF model. The MRF model learning is carried out for a given image derived from a *class of images*. The term learning is used to convey the learning of the parameters associated with the model. Thus, the learning problem is reduced to the model parameter estimation problem. This problem is formulated in Maximum Conditional Pseudo Likelihood (MCPL) framework, and the estimates of the parameters are obtained using homotopy continuation method. Having learnt a given image, the model is validated for images assumed to be derived from the same class to which the training image belongs. A Parallel Hybrid Tabu Search (PHTS) Algorithm is proposed to obtain the label estimates while validating the image model for images other than the training image. The performance of the PHTS and HTS algorithm is compared with that of SA algorithm. This notion could be validated for real indoor, outdoor and brain MR images.

Acknowledgments

I have been very fortunate to have Dr. Pradipta Kumar Nanda, Professor, Department of Electrical Engineering, National Institute of Technology, Rourkela as my thesis supervisor. He introduced me to the field of Image Processing and Computer Vision, educated me with the methods and principles of research and, guided me patiently throughout this thesis work. He is the whole Philosopher and Guide behind this thesis. I am highly indebted and express my deep sense of gratitude to him for his invaluable guidance, constant inspiration and motivation with enormous moral support during my difficult phase to complete this work. I am extremely thankful to him for his incredible contribution in writing the manuscript despite his busy schedule as the Head of the Department. Working with him, a person with commitment and positive attitude is highly rewarding experience.

I am extremely grateful to Prof. Sunil Kumar Sarangi, Director, N.I.T. Rourkela, for his inspiring words and supports in completion of the thesis. I humbly acknowledge the creative criticism and constructive suggestions of Prof. K.K. Mishra, Prof. J.K. Satapathy, Prof. S. Ghosh and, Prof. B. Majhi, committee members, while scrutinizing my research work.

Many thanks to all the people whose friendship and companionship has given a lot of encouragement during my research work. I want to express my sincere appreciations to Dr.Susmita Das for extending her helping hand and support during my difficult period. Inspirations and support from Mrs Sucheta Panda, Dr. Suprava Pattnaik and K.R.Subhashini are highly encouraging. I also want to extend my profound appreciations to my relatives who have supported and encouraged me over the years specially to my cousin Lipu for his significant contribution in managing the home front efficiently during this period.

This work was made thoroughly enjoyable by the friendly and congenial atmo-

sphere of the Image Processing and Computer Vision (IPCV) Laboratory of Electrical Engineering Department. I express my sincere thanks to all the past and present members of this Lab. I acknowledge with thanks the help rendered by Priyadarshi Kanungo for spending his valuable time to assist me in preparing the thesis and presentation slides. My thanks are also due to Parthajit Mohapatra and Umesh Chandra Samal for their valuable contribution in preparing this manuscript.

I am highly indebted to N.I.T. Rourkela for providing me the facilities like library, computational facility and Internet access, without which it could not have been completed in time.

I am extremely thankful to all the staff members of the Department of Electrical Engineering, N.I.T. Rourkela for their encouragement and co-operations throughout this period.

Finally, I owe my largest debt to my family. I am highly indebted to my parents, sister, brother and my loving kids for their love, affection, constant encouragement and invaluable support throughout this difficult period. Son Debabrata and daughter Akankshya have been the pillars of strength and support behind me in spite of many constraints, adjusted to my long working hours with proper understanding. I also want to extend my sincere thanks to my husband Anil for motivating me to initiate the research work. I dedicate this work to all of them.

Contents

List of Figures

List of Tables

List of Acronyms

Algo.	Algorithm
AR	Autoregressive
CPL	Conditional Pseudo Likelihood
CSF	Cerebro Spinal Fluid
CT	Computed Tomography
EM	Expectation-Maximization
EPI	Echo Planar Imaging
FCM	Fuzzy C-Means
FID	Free Induction Decay
FLASH	Fast Low Angle Shot
GA	Genetic Algorithm
GD	Gibbs Distribution
GHMRF	Gauss Hidden Markov Random Field
GM	Gray Matter
GRF	Gibbs Random Field
HMM	Hidden Markov Model
HMRF	Hidden Markov Random Field
HTS	Hybrid Tabu Search
hybd.	hybrid
ICE	Iterated Conditional Estimation
ICM	Iterated Conditional Mode
MAP	Maximum a Posteriori
MCL	Maximum Conditional Likelihood
MCMC	Markov Chain Monte Carlo
MCPL	Maximum Conditional Pseudo Likelihood

ML	Maximum Likelihood
MRF	Markov Random Field
MRI	Magetic Resonance Imaging
NMR	Nuclear Magnetic Resonance
NMRI	Nuclear Magnetic Resonance Imaging
PD	Photon Density
PHTS	Parallel Hybrid Tabu Search
prll.	parallel
RF	Radio Frequency
SA	Simulated Annealing
SNR	Signal to Noise Ratio
TEM	Tabu-Expectation-Maximization
TS	Tabu Search
WM	White Matter

Nomenclatures

X	Random field associated with the labels of the original image.
X_i	Random variable of i^{th} site of the original image.
Y	Observed random field.
Y_i	Random variable of the i^{th} site of the observed image.
x	Realization of X.
y	Realization of Y.
f	Random field associated with line field.
θ	Parameter associated with image model.
θ_l	Parameter of each class with Gaussian distribution.
μ	Mean value of Gaussian distribution.
σ	Standard deviation of Gaussian distribution.
μ_l	Mean value of each class label with Gaussian distribution.
σ_l	Standard deviation of each class label with Gaussian distribution.
L	Set of class labels.
l	Class label variable.
$P(.)$	Probability.
$P(.\|.)$	Conditional probability.
S	A rectangular image lattice.
(i, j)	A pixel of an image lattice.
$(M \times N)$	Size of the image lattice.
$\eta_{(i,j)}$	Neighbourhood of pixel (i, j).
η^m	m^{th}-order neighbourhood.
$U(.)$	Energy function of Gibbs distribution.
Z	Partition function.
T	Temperature parameter.

T_{in}	Initial temperature.
c	A clique.
C	Collection of all cliques.
ϕ	Clique parameter vector.
$\text{dist}(A, B)$	Euclidian distance between A and B.
$V_c(.)$	Clique potential of MRF model.
x^*	True and unknown labeling configuration.
$\hat{x}$	Estimate for x^*.
K	Length of Tabu array.
α	External field parameter of clique potential.
β	Internal field parameter of clique potential.
$U_p(.)$	A posteriori energy function.
h_{ij}	Horizontal linefield in the energy function.
v_{ij}	Vertical linefield in the energy function.
q_t	Actual state at time t.
$a_{i,j}$	State transition probability of states S_i and S_j.
$h(.,.,.)$	Homotopy map.
$f(.)$	system of functions to be solved.
$g(.)$	system of functions with known solutions.
λ	Homotopy continuation Parameter.
$\vec{M}$	Stationary magnetisation vector.
$\vec{M}_r$	Rotating magnetisation vector.
ω	Transverse angular frequency.
ω_0	Angular frequency.
$\vec{H}$	Net effective magnetic field.
H_0	Strength of the external magnetic field along z-direction.
r	Spatial location vector in the spinning nuclei system.

$\vec{H}_r(r)$	Net magnetization field vector.
$\vec{M}(r,t)$	Net magnetization vector.
$v(t)$	Raw NMR signal.
$\phi(t)$	Magnetic flux through RF coil.
$T1$	Longitudinal relaxation time.
$T2$	Transverse relaxation time.
$\rho(x,y,z)$	Echo signal density.
$\rho_0(x,y,z)$	Initial spin density function.
G	Strength of the gradient field.
d	Diameter.
$\vec{m}$	Magnetic moment.
$\vec{J}$	Spin angular moment.
γ	Gyromagnetic ratio.
T_E	Time for echo formation.
T_R	Cycle repetition time.
ΔH	Maximum deviation of H over imaging volume.
$\triangleq$	By definition.

Chapter 1

Introduction

Segmentation and analysis of underlying structures in an image is of importance in a variety of image analysis and computer vision applications including robot vision, pattern recognition and biomedical image processing. The segmentation of an observed image into an unknown number of regions with distinct homogeneous behaviour is a fundamental issue in all the above fields. It can be viewed more generally as a critical early process providing input to the higher level processing schemes of a computer vision system. The problem of image segmentation have gone through many stages of development and refinement in the last few decades [1, 4]. However, any individual image segmentation tool is not likely to achieve reliable results under all circumstances. The bulk of existing work on image segmentation can be classified into three basic approaches: region based approach, boundary based approach and pixel classification approach [2, 3, 4, 8, 12, 15]. The segmentation technique heavily depends on the type of features (image attributes) used, reliability with which these features are extracted and the criteria used for merging pixels based on the similarity of their features. Region based method depends on the homogeneity of spatially densed localized features and other pixel statistics. Simple thresholding is the most easiest region based segmentation method [1, 4, 5]. However, even after a careful choice of threshold, for most practical images that are noisy, thresholding produces poor results. Often, this problem is viewed as a pixel classification problem and

hence formulated as a pixel labeling problem [9, 11, 14]. Each pixel in the observed image is assigned a label designating the region or class to which it belongs. The model based approaches can be broadly categorized as either *supervised* or *unsupervised* problem. The problem consists of (i) modeling the image pixel labels (ii) development of an estimation strategy for the associated unknown model parameters, and (iii) label estimation for each pixel of the image. Statistical methods are a popular choice for image segmentation because they involve image features that are simple to interpret by using a model and the methods are firmly rooted in statistical inference [6, 10].

1.1 Image models

In recent years, stochastic models have become more popular in image processing. Out of the various stochastic models, Markov Random Field (MRF) model provides a better framework for many complex problems in image segmentation [16, 17, 18, 30, 49]. This is due to the fact that, MRF model is based on the notion of neighbourhood structure and therefore, helps in understanding global interaction through local spatial interactions. Moreover, the global interaction is governed by Gibbs distribution [14]. Following the seminal work of Geman and Geman, the potentiality of the model was enhanced further by incorporation of line processes [11] that attributes to the edge preserving property, MRF based methods have been widely used by researchers [13, 15, 19, 22, 29, 42, 47, 87, 122]. Another popular stochastic model, Hidden Markov Model (HMM) [25, 26, 27, 52] is a doubly embedded stochastic model and has been extensively used for speech recognition. This model is specifically useful where the data is hidden and the observed sequence is a stochastic function of the hidden and unobserved state sequence. This hidden sequence is assumed to be a Markov process. HMM has also been successfully applied

combined with AR model for 2-D shape classification [28], for character recognition [34]. In image processing literature, a special version of HMM, applied to 2-D, named Hidden Markov Random Field (HMRF) model has been used recently [45, 46, 53, 51, 95]. In this model, the hidden field is modeled as a Markov random field instead of a Markov chain.

1.2 Supervised Image Segmentation

In supervised framework, the model parameters are assumed to be known *a priori* or assumed on an ad hoc basis. These model parameters are subsequently used for estimation of pixel labels in segmentation framework. Often, the pixel labeling problem, using MRF model, has been formulated using Maximum a Posteriori (MAP) criterion and Bayesian framework [11, 13, 15, 18]. Segmentation of noisy images including textured images using MRF model could be formulated in supervised manner successfully [18, 24]. Bouman *et al.* proposed multiscale random field and sequential MAP estimator for supervised image segmentation [41]. Nanda *et al.* [42] have proposed a supervised image segmentation method where the MRF model parameters are estimated using homotopy continuation method and MAP estimate of the image labels are obtained by SA algorithm. By and large, in supervised framework, the MAP estimates are obtained by Simulated Annealing algorithm. However, Tabu Search strategy, which is described later could be an alternate tool for such kind of problems. In this thesis, the notion of Tabu Search is exploited to obtain the MAP estimation of image labels.

1.3 Unsupervised Image Segmentation

In unsupervised framework, the number of classes, the class labels and the model parameters are assumed to be unknown. Hence, simultaneous estimation of image

labels as well as model parameters is required. Since, the image label estimation depends upon the optimal set of parameters, and vice versa, the unsupervised image segmentation may be viewed as an incomplete data problem. To handle such incomplete data problem, an iterative scheme namely expectation maximization (EM) algorithm has been suggested in the literature [39, 36, 54].

As an initiative in this direction, Besag [15] has suggested a recursive parameter estimation in the MPL framework and iterated conditional mode (ICM) algorithm for image label estimation. In the sequel, Zhang *et al.* [37, 38, 40] has suggested an unsupervised scheme which alleviates the difficulty in computing expectation in EM algorithm for general models. In order to accomplish this objective, he has proposed a Monte Carlo averaging scheme and a scheme related to Besag's ICM algorithm. A spatially variant mixture model for pixel labeling was also addressed by Sanjay *et al.* [7] with assumption of number of class labels. Zhou *et al.* [43] had developed a general method for estimating the ML hyper parameter for Gibbs prior from incomplete data. Fabien *et al.* [50] introduced the fuzzy logic in HMM and implemented iterated conditional estimation (ICE) for segmentation. Assuming the number of classes to be known, the scheme could yield proper segmentation results. Many image segmentation problems, using MRF model, are also addressed in unsupervised framework [22, 23, 47]. In [22], a hierarchical MRF model is used as the image model and Markov Chain Monte Carlo (MCMC) algorithm is used to sample the posterior distribution. The model parameters as well as image labels are simultaneously estimated in each scan. An unsupervised image segmentation scheme based upon the notion of energy splitting is proposed by Deng *et al.* [47]. Usually, the above mentioned energy is splitted into two components namely (i) feature component and (ii) region label component. The segmentation process depends on the proper weightage of these components and the weighting parameters corresponding to the two components are varied in accordance with the annealing

schedule to obtain proper segmentation.

1.4 Tabu Search Technique

The conventional optimization algorithm suffers from the problem of local minima trapping. This problem is circumvented by the stochastic optimization algorithms such as Simulated Annealing (SA) and Genetic Algorithm (GA). Usually, the stochastic optimization algorithms are computationally intensive. One of the reasons could be attributed to the revisiting of the candidate solutions already visited in the search space. Tabu Search, proposed by Glover [55, 56, 57] may be viewed as a strategy to solve combinatorial optimization problems and is an adaptive procedure which overcomes the limitations of local optimality. Tabu Search based algorithms have been successfully used for clustering data [58], digital filtering [59], switching networks [62] and, image processing [60, 114]. Recently evolutionary Tabu Search has been proposed for cell image segmentation [61]. The proposed algorithm in [61] has been shown to outperform GA. A comparison between SA, GA and Tabu Search has been presented in [63]. Hybrid Tabu Search algorithms have been proposed in [114] to obtain MAP estimate of the image labels. In [114], specifically a parallel hybrid Tabu Search based algorithm is proposed to reduce the computational burden and the performance of the proposed algorithm was compared with that of the Simulated Annealing algorithm. Tabu Search and MRF models have also been used for region extraction [87], where MRF is defined using polar co-ordinate system and Tabu Search has been employed to explore the radial sites due to this polar co-ordinates.

1.5 Brain MR Image

The rapid development of imaging technologies now routinely allows living organs and organisms to be explored non-invasively [67, 68]. Medical images are obtained for various applications which includes image guided surgery, surgical simulation, neuroscience studies and therapy evaluation. When working with medical images, i.e. Magnetic Resonance Images (MRI), X-Ray, ultrasound and Computed Tomography (CT) images etc., it is often to delineate the areas and volumes of interest. Medical experts face the task of finding or characterizing abnormalities within such images. The rapid development of different kinds of highly equipped medical instruments and more use of such images have made it difficult for the medical experts to interpret and infer correct diagnosis. Complicated image features, eye fatigue are the factors that may cause an expert to miss an abnormality in an image. Hence, there is a great need for robust methods that process with the interpretation of huge amounts of data with greater accuracy. To alleviate these difficulties in clinical diagnosis, segmentation of medical images provides the potentiality for increasing the diagnostic accuracy [94].

Magnetic Resonance Imaging (MRI) is a well established non-invasive diagnostic medical imaging technique based on the nuclear magnetic resonance phenomenon [66]. Although qualitative image analysis is often sufficient for diagnosis of diseases, quantitative analysis is necessary for many applications, for which segmentation is a primary step[79, 80]. Segmentation of MR Images is a challenging problem due to its complexity as well as to the absence of models of the anatomy that fully capture the possible deformations in each structure. Conventional MRI relies on a difference in a weighted average of spectral and temporal information from tissue to tissue to make a diagnosis. The intensity of the MR image of human tissue is homogeneous and the structure of each tissue is connected, but is difficult to separate the adja-

cent tissue due to the small intensity changes and smoothed boundaries between tissues. Further, the lack of clearly defined edges includes intra- and inter-observer variability, which deteriorates the significance of the analysis [89, 90]. Brain tissue is a complex structure. The diagnosis of many brain disorders involves accurate tissue segmentation of brain MR images. Manual delineation of the three brain tissues, white matter (WM), grey matter (GM) and Cerebrospinal fluid (CSF) in brain MR image by an human expert is too difficult. Thus, segmentation of brain MR images is an important step for the same, and has attracted the attention of many researchers for the last decade [77, 78, 80, 85].

1.6 Brain MR Image Segmentation

The segmentation of brain MRI is a challenging problem that has received an enormous amount of attention lately by various researchers [48, 70, 73, 76, 81, 82, 95, 96, 98, 99, 100, 101, 102, 103, 105, 106, 107, 108, 111]. The methods in the boundary based approach suffer from spurious edges. The methods in the pixel classification and region based approaches are limited by the difficulties due to intensity inhomogeneities and partial volume effects [78, 79, 104, 113]. Furthermore, all methods are degraded by noise perturbations in low contrast and low signal-to-noise-ratio images. To start with, an adaptive threshold based segmentation technique using the structural information of brain MRI was proposed in [76]. The method depends upon a sequence of histogram analysis. Many of the proposed schemes are unsupervised in nature and have used the Expectation Maximization (EM) algorithm to obtain the solution. EM algorithm, first proposed by Dempster [36], handles incomplete data problem and the estimated model parameters are the likelihood estimates. Since the model based unsupervised brain image segmentation problem is often viewed as an incomplete data problem, EM algorithm has been used to obtain the proper

segmentation [64, 72, 73, 96, 86, 99, 101]. Wells *et al.* [99] have proposed an adaptive brain MR image segmentation scheme in EM framework. They have also taken into account the spatial intensity inhomogeneity and have estimated the bias field. The tissue class is modeled as Gaussian distribution. The results of Wells *et al.* [99] were improved by Guillemaud *et al.* [101] by considering uniform probability density for some other classes besides the Gaussian distribution. The EM algorithm is modified appropriately to take care of the mixture models. Here, the bias field is also estimated. Held *et al.* [100] refined the adaptive segmentation algorithm. Leemput *et al.* [109, 110] developed a generalized EM algorithm for tissue classification and bias field correction. They used the variable parameters of Gaussian which changes in the algorithm. Marroquin *et al.* [102] adopted a new Bayesian method for automatic segmentation of brain MRI. They use a variant of the EM algorithm making the whole procedure computationally efficient. All of the above statistical approaches need good initialization of tissue class. Ahmed *et al.* [112, 113] presented a modified Fuzzy C-Means algorithm for bias field estimation and segmentation of brain MRI. They proposed a modification to the standard FCM objective function by introducing a term that allows the labeling of a voxel to be influenced by the labels in its immediate neighborhood. This modification to accommodate neighborhood blurs the edge of tissues and hence produces the segmenting errors. Siyal *et al.* [97] presented a modified FCM algorithm formulated by modifying the objective function of the standard FCM and uses a special spread method for classification of tissues.

MRF model and its variants have been successfully used for brain MR image segmentation [82, 95, 96]. Recently, Hidden Markov Random Field (HMRF) model has been proposed by Zhang *et al.* [95] to achieve brain MR image segmentation. The segmentation obtained by Zhang's approach greatly depends upon the proper choice of initial model parameters. This problem of proper selection of initial pa-

rameters has been alleviated by Nanda et al. [115] by proposing a Tabu Search based EM algorithm. Tabu Search algorithm has the global converging attribute and hence satisfactory results could be obtained using the proposed Tabu EM algorithm. Yong Yang et al. [70] have proposed an improved EM algorithm with the region growing approach, specifically, to reduce the space complexity. Reducing time and space complexity is also accomplished by Shu-Kay NG [48] where a multiresolution k_d tree structure is adopted in performing the E-step. The proposed algorithm is claimed to outperform other variants of EM . A fuzzy Markov Random Field model is used for segmentation of brain MR images [82]. The associated model parameters are estimated using a stochastic gradient algorithm and, in the sequel, the segmentation is carried out using ICM algorithm. Jagath Rajapakse et al. [86] have proposed a greedy algorithm based on ICM algorithm to determine the image labels. Very recently, automatic segmentation of MR images of the developing new born brain has been addressed [98] using the notion of graph clustering and parameter estimation for finding the initial intensity distributions. These distributions together with the spatial priors are subsequently used for bias correction. It is to be noted that EM algorithm yields solution at the cost of high computational burden. In order to overcome this bottleneck, J.L.Marroquin et al. [20] have proposed a new class of probabilistic model, called Hidden Markov Measure Field model, that solved the complex segmentation problem by minimization of differentiable energy function. The performance of these models was found to be superior to that of MRF model. All the above mentioned models are homogeneous in nature. In the context of segmentation, in order to capture the class label information, an inhomogeneous HMRF model is adopted by Gu et al. [96]. An EM algorithm is developed [96] for parameter estimation of both prior and likelihood probabilities to achieve proper segmentation.

1.7 Summary of the thesis

In this thesis, attempts are made to address the problem of image segmentation in both supervised and unsupervised framework. In both these frameworks, the focus is on brain MR image segmentation. In the supervised framework, the notion of model learning is introduced to investigate the problem in the supervised learning paradigm. In all the cases, the observed degraded image is assumed to be corrupted with white Gaussian noise. Analogously in brain MR images, the MR image is assumed to be corrupted. The brain MR images used in this thesis are taken from the site "www.med.harvard.edu/AANLIB/info.html" of *Harvard Medical School.*

In order to handle such complex degraded images, the problem is cast as pixel labeling problem. Inspired by the work of Wells *et al.* [99], Brady *et al.* [101] and Zhang *et al.* [95], the model based approach is adhered for segmentation. Specifically, the unknown *a priori* class labels are modeled as MRF while the observed degraded images are modeled as GHMRF model. In supervised framework, these model parameters are assumed to be known *a priori.* The image labels are estimated using these known model parameters. The image label estimation is formulated in Bayesian framework using MAP criterion. Hybrid Tabu Search (HTS) algorithm is developed to obtain the MAP estimate and its performance is compared with SA and ICM algorithm.

It is observed that the selection of MRF and GHMRF parameters becomes a tedious task. with increase in the number of classes. This problem could be circumvented by addressing it in unsupervised framework where both the model parameters and image labels are estimated together. This problem can be viewed as an incomplete data problem and hence the problem is formulated in EM framework. Zhang *et al.* [95] have developed EM based algorithm for brain MR image segmentation, but the performance of the algorithm greatly depends upon the selection of initial model

parameters. In this thesis, in EM framework, a Tabu Search based TEM algorithm is proposed that does not require to have proper choice of initial model parameters. The proposed algorithm yielded satisfactory results starting from different arbitrary initial conditions.

A new notion of model learning is introduced for image segmentation in supervised framework. Here, MRF model is employed to model the class labels and the MRF model learns a given training image from a class of images. The model having learnt is validated for other images from the same class as the training image. Motivated by the work of Nanda *et al.* [42], these model parameters are estimated using homotopy continuation algorithm. This model learning notion could be successfully tested for indoor, outdoor and brain MR images. The HTS algorithm is parallelized to obtain the segmented images and its performance is compared with HTS and SA algorithm. The major contributions of the thesis can be summarized as follows.

- A Hybrid Tabu Search (HTS) based supervised image segmentation scheme is proposed and the performance is found to be better than the schemes using SA and ICM algorithm. The algorithms could be validated in case of synthetic as well as brain MR images.

- In the unsupervised case, a new scheme is developed based on the proposed Tabu-EM (TEM) algorithm in Expectation Maximization (EM) frame work. Gauss Hidden Markov Random Field (GHMRF) model and the MRF models are used as the image models.

- The proposed scheme does not require to have proper choice of initial model parameters which in turn greatly affects the process of segmentation. The proposed algorithm could be successfully tested with noisy images. The results obtained by our approach are quite comparable to that of Zhang's approach [95].

- A new notion of MRF model learning using homotopy continuation method is also introduced. Attempts have been made to make the MRF model learn for a class of images as opposed to a single image. Out of the given class of images, one image is selected and used as the training image for the MRF model learning. With proper learning, the same model could be used for the class of images from which the training image is derived.

- This learning attribute could be exploited while estimating the image labels. A Parallel Hybrid Tabu Search (PHTS) algorithm is proposed and employed to obtain the *maximum a posteriori* (MAP) estimates of the image labels besides the above mentioned HTS algorithm. The performance of these algorithms are compared with that of Simulated Annealing (SA) algorithm and it is observed that the proposed algorithms converge faster than that of SA.

1.8 Organization of the Thesis:

The thesis is organized into the following chapters.

Chapter 1 deals with the formal description of the problem of segmentation, brain MR image segmentation, supervised and unsupervised image segmentation, Tabu Search technique, MRF model and the related research work already carried out in the above directions. The problem addressed in this thesis is also included.

The basic notion of Magnetic Resonance Imaging and the techniques used are described in Chapter 2. A brief description about brain MRI as well as the tissue structure of the brain is also depicted here. Background on Markov Random Field and Gibb's Random Field which includes the description on line field and Gibb's sampler is presented in Chapter 3. Hidden Markov Models are also focused in this chapter. Basic notions of Tabu Search procedure, and the basic Tabu Search algorithm are developed in Chapter 4.

In Chapter 5, the problem of image segmentation is addressed in a supervised framework followed by the detail formulation of Hidden Markov Random Field (HMRF) model. The problem is cast as a pixel labeling problem which is formulated in *Maximum A Posteriori* GHMRF framework. The proposed HTS algorithm is developed and is used for image label estimation. The performance of the algorithm is compared with that of Simulated Annealing(SA) and Besag's Iterated Conditional modes algorithm(ICM). Simulation results are presented for synthetic as well as brain MR images.

Chapter 6 deals with the problem of image segmentation in unsupervised framework. The joint parameter estimation and label estimation is formulated in EM framework. The proposed HTS algorithm is used in E-step to estimate the pixel labels and hence form the complete data set. Tabu-EM algorithm is proposed for the unsupervised image segmentation. The proposed TEM algorithm starts from an arbitrary starting point. The performance of the algorithm is compared with the results obtained by Zhang's [95] approach. Simulation results are presented for synthetic as well as brain MR images.

Chapter 7 begins with a brief background on Homotopy Continuation method. In the sequel, MRF model parameter estimation based on homotopy continuation method is formulated. The problem of model learning is also explained. The image segmentation problem using the estimated parameters is formulated in Bayesian framework. The MAP estimates of the image labels are obtained by the proposed HST algorithm. A parallel hybrid Tabu (PHTS) algorithm is proposed with a view to reduce the computational burden and hence making feasible for real time implementation. The performance of HTS and PHTS algorithms are compared with that of SA algorithm. Simulation results for different class of real images are presented. Conclusions drawn on various issues are presented in Chapter 8 and the scope for future work is also outlined here.

List of Publications

1. D.Patra and P.K.Nanda, "Tabu Search based Brain MR Image Segmentation using Hidden Markov Random Field Model," *Proceedings of 1st International Conference on Frontier Technologies- Need for the Industry, Business and Education*, pp. 350-354,2006.

2. P.K. Nanda, D. Patra and A. Pradhan, "Brain MR Image Segmentation using Tabu Search and Hidden Markov Random Field Model," *Proceedings of 2nd Indian International Conference on Artificial Intelligence (IICAI-05)*, pp. 3143-3160, 2005.

3. P. K. Nanda and D. Patra, "Image Segmentation using Parallel Tabu Search Algorithm and MRF Model," *Proceedings of National Conference on Communications (NCC-2005)*, pp. 336-340, 2005.

4. P.K. Nanda and D. Patra, "Parallel Hybrid Tabu Search algorithm for Image Restoration," *Proceedings of International Conference on Communications, Devices and Intelligent Systems*, pp. 532-535, 2004.

5. P. K. Nanda, D. Patra and A. Pradhan, "Unsupervised Image Segmentation Using Tabu Search and Hidden Markov Random Field Model," *Proceedings of National conference on Recent Advances in Power, Signal Processing and Control*, pp. 133-139, NIT Rourkela, Nov. 16-17,2004.

6. P. K. Nanda, D. Patra and B. Nayak, "A Tabu Search and Simulated Annealing based hybrid Algorithm for Image Restoration using Markov Random Field Model," *Proceedings of National Seminar on Application of Evolutionary Strategies to Power, Signal Processing and Control*, pp. 41-45, NIT Rourkela, Feb 14-15,2002.

Chapter 2

Magnetic Resonance Imaging

2.1 Introduction

The advent of medical imaging modalities such as X-ray, ultrasound, Computed Tomography (CT) and Magnetic Resonance Imaging (MRI) has greatly improved the diagnosis of various human diseases. The most common procedure to analyze imaging data is visual inspection on printed support. In the last decade, computer-aided medical image analysis techniques have been employed to provide a better insight into the acquired image data.

Magnetic Resonance Imaging (MRI) has become a leading technique, widely used for imaging human soft tissue anatomy [66, 67, 69, 68]. Its applications are extended over all parts of the human body and it represents the most common visualisation method of human brain. It has several advantages over other imaging techniques, enabling it to provide three dimensional (3-D) data with high contrast between soft tissues [66, 117, 118].

Felix Bloch and Edward Purcell discovered the magnetic resonance phenomenon independently in 1946 and both were awarded the Nobel Prize in 1952. Magnetic Resonance Imaging (MRI) is based on the principles of Nuclear Magnetic Resonance (NMR), a spectroscopic technique used by scientists to obtain microscopic chemical and physical information about molecules. The technique was called Magnetic Res-

onance Imaging rather than Nuclear Magnetic Resonance Imaging (NMRI) because of the negative connotations associated with the word nuclear in the late 1970's. In the period between 1950 and 1970, NMR was developed and used for chemical and physical molecular analysis. In 1971, Raymond Damadian showed that nuclear magnetic relaxation times of tissues and tumors differed, thus motivating scientists to consider magnetic resonance for the detection of diseases.

2.2 MRI Principles

The principles of NMR is based on the absorption and emission of energy in the radio frequency range of the electromagnetic spectrum. The basic objective of MR imaging is to map the spatial location and associated properties of specific nuclei or protons present in the object being imaged [66, 67]. The content of the human body is primarily fat and water which have many hydrogen atoms that make the 63% of human body [119]. Hydrogen nuclei have a NMR signal. So, MRI primarily images the NMR signal from the hydrogen nuclei. A fundamental property of nuclei with odd atomic weight and/or odd atomic numbers is the possession of angular moment called spin. These protons carry an electric charge and spins around their axes. Because of the spinning, the charged protons create a magnetic field around them and thus act like tiny magnets, possessing both angular moment and magnetic moment. The magnetic moment is proportional to the spin angular moment and is related through a constant called the gyro-magnetic ratio, a quantum property of the proton. Thus the relationship between the spin angular moment J and the magnetic moment m, is given by

$$m = \gamma J \tag{2.1}$$

where γ is gyro-magnetic ratio defined in MHz/T. The gyro-magnetic ratio of hydrogen proton is 42.58 MHz/T, providing a corresponding magnetic moment, that

is excellent for imaging the human body under an external field of 0.5T to 1.5T.

The spinning protons with both angular and magnetic moment possess a specific spin quantum number that characterizes their orientations and corresponding energy levels with or without the presence of an external magnetic field. In the absence of an external magnetic field, the direction of the magnetic moments of spinning protons or nuclei is completely random. In the presence of an external magnetic field, the magnetic moments of nuclei result in a nuclear paramagnetic polarization with specific orientations and energy levels as characterized by their spin quantum number. Again, the interaction between the magnetic moment of nuclei with the external magnetic field causes the spinning nuclei to process similar to the wobbling of a spinning top under a gravitational field. The spin quantum number of hydrogen proton is 1/2. When this nuclei is placed under an external magnetic field, it is either aligned along the external magnetic field or against the magnetic field. The energy level of nuclei aligning themselves along the external magnetic field is lower than the energy level of nuclei aligned against the external magnetic field. Upon establishing a thermal equilibrium in the presence of an external magnetic field, the total number of nuclei aligned along the external magnetic field is slightly larger than the number of nuclei aligned against the external magnetic field. This results in a net magnetization vector in the direction of the external magnetic field. However the precession phase is still random, providing a net zero vector in the transverse direction.

Using the principle of classical mechanics, the torque generated by the interaction of magnetic moment of a proton and the external magnetic field is equal to the rate of change of angular momentum and is given by the equation of motion for isolated spin is as

$$\frac{d\vec{J}}{dt} = m \times \vec{H}_0 = m \times H_0\vec{k} \tag{2.2}$$

since $\vec{m} = \gamma \vec{J}$

$$\frac{d\vec{J}}{dt} = \gamma J \times H_0 \vec{k} \tag{2.3}$$

where H_0 is the strength of the external magnetic field and $\vec{k}$ is the unit vector along z-direction. The solution of the above equation leads to an important relationship that provides angular frequency, ω_0 of nuclear precession as

$$\omega_0 = \gamma H_0 \tag{2.4}$$

The above relationship in Equation(2.4) is known as the Larmor Equation. Thus, the precession frequency depends on the type of nuclei with a specific gyro-magnetic ratio and the intensity of the external magnetic field. This is the frequency on which the nuclei can receive the Radio Frequency (RF) energy to change their states for exhibiting nuclear magnetic resonance. The excited nuclei return to the thermal equilibrium through a process of relaxation emitting energy at the same precession frequency ω_0.

During nuclear magnetic resonance, upon receiving the RF energy at the Larmor frequency, the nuclei spinning with an orientation along the external magnetic field can flip to the orientation against the magnetic field. As a result of the change in orientation of the excited nuclei, the net longitudinal vector is no longer in the direction of the external magnetic field (z-direction). It starts moving away from the z-direction. The RF energy pulse required to flip the net longitudinal magnetization vector by 90 degrees and 180 degrees respectively are called "90-degree pulse" and "180-degree pulse" respectively. After the completion of the 90-degree pulse, all of the nuclei precess in phase, and therefore form a net non-zero transverse vector that rotates in the x-y plane perpendicular to the direction of the external magnetic field. The longitudinal vector flips over with a 180-degree clockwise shift in the direction against the external magnetic field after the completion of the 180-degree pulse. The

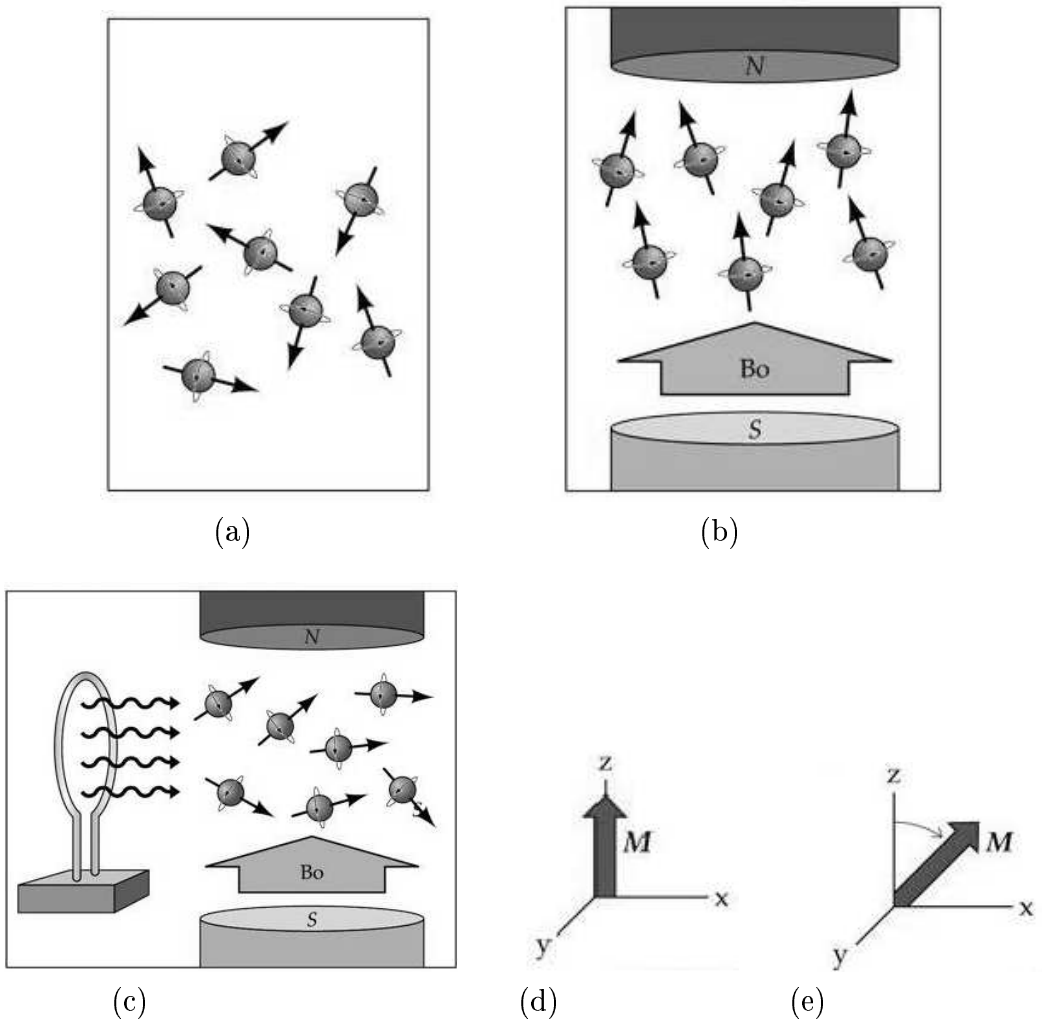

Figure 2.1: *Behaviour of spinning protons during nuclear magnetic resonance; (a) No external field (b) External field applied, (c) Radio-frequency pulse given, (d) Net magnetisation vector M for (b), (e) Net magnetisation vector for (c)*

spinning behaviour of protons as well as the orientation of net magnetisation vector is shown in Figure 2.1.

The RF energy is provided by a RF electromagnetic coil that transmits an oscillating RF wave at the Larmor frequency to cause nuclear excitation. After the RF pulse is turned off, the excited nuclei go through a relaxation phase emitting the absorbed energy at the same Larmor frequency that can be detected as an electrical signal, called the Free Induction Decay (FID). Under this phase, the net longitudinal

magnetization vector returns to its original state in the thermal equilibrium and the net transverse magnetization vector disappears due to de-phasing of the nuclei. The free induction decay of the electromagnetic signal in the RF coil is the basic signal, that is used to create MR images and can be acquired through the same RF coil tuned at the Larmor frequency.

Assuming N to be the total number of spinning nuclei in the object being imaged, a stationary magnetization vector $\vec{M}$ can be defined from the available magnetic moments as

$$\vec{M} = \sum_{n=1}^{N} \vec{m}_n \tag{2.5}$$

If $\vec{M}$ and $\vec{M}_r$ are stationary magnetization vector and rotating magnetization vector respectively and can be defined as follows.

$$\vec{M} = M_x\vec{i} + M_y\vec{j} + M_z\vec{k} \tag{2.6}$$

$$\vec{M}_r = M_{x'}\vec{i'} + M_{y'}\vec{j'} + M_{z'}\vec{k'} \tag{2.7}$$

the relationship between them can be expressed as

$$\frac{d\vec{M}}{dt} = \frac{\partial\vec{M}_r}{\partial t} + \omega \times \vec{M}_r \tag{2.8}$$

where ω is the angular frequency at which the transverse plane rotates. From the above formulation, the rate of change in the net stationary magnetization vector can be expressed as (Bloch Equation)

$$\frac{d\vec{M}}{dt} = \gamma\vec{M} \times \vec{H} \tag{2.9}$$

where $\vec{H}$ is the net effective magnetic field. Considering the total response of the spin system in the presence of an external magnetic field along with the RF pulse for nuclear excitation followed by the nuclear relaxation phase, the change of the net magnetization vector can be expressed as

$$\frac{d\vec{M}}{dt} = \gamma\vec{M} \times \vec{H} - \frac{M_x\vec{i} - M_y\vec{j}}{T2} - \frac{(M_z - M_z^0)\vec{k}}{T1} \tag{2.10}$$

where M_z^0 is the net magnetization vector in thermal equilibrium in the presence of H_0 only. $T1$ and $T2$ are the longitudinal(spin-lattice) and transverse(spin-spin) relaxation times respectively in the nuclear relaxation phase when excited nuclei return to their thermal equilibrium state. The magnetic flux $\phi(t)$ through the RF coil can be given as

$$\phi(t) = \int_{object} \vec{H_r}(r)\vec{M}(r,t)dr \tag{2.11}$$

where r= spatial location vector in the spinning nuclei system

$$r = x\vec{i} + y\vec{j} + z\vec{k} \tag{2.12}$$

where $\vec{H_r}(r)$ = net magnetization field vector and $\vec{M}(r,t)$ = net magnetization vector. The voltage induced in the RF coil, $v(t)$ is the raw NMR signal. Using Faraday's Law of electromagnetic induction

$$v(t) = -\frac{\partial\phi(t)}{\partial t} = -\frac{\partial}{\partial t}\int_{object} \vec{H_r}(r)\vec{M}(r,t)dr \tag{2.13}$$

The realization of spatial location dependent signal $v(t)$ in Equation (2.13) is responsible to create an MR image that maps the magnetic resonance response of the spinning nuclei available in that location. The spatial locations within the object that is placed inside a large magnet producing the static external magnetic field can be viewed as small volumes containing nuclei that can be excited using different RF frequencies. NMR signals generated by specific excited volumes within the object can thus be discriminated with respect to the individual RF frequencies. Access to the small volumes within the object to generate corresponding NMR signals is obtained through spatial encoding techniques. These techniques utilize different gradient methods for frequency and phase based spatial encoding. Once the spatial locations with an object being imaged are accessed, the corresponding NMR signals are acquired using specific RF pulse sequences for image reconstruction.

2.3 MR Parameters

Magnetic Resonance is an extremely useful tool despite its limited sensitivity. The great utility of MR is derived from many contrast mechanisms that are contained in the MR signal. The conventional MR images take advantages of three common parameters of nuclei :

1. Spin density (density of nuclei)
2. Longitudinal relaxation time $T1$
3. Transverse relaxation time $T2$

The challenge in using MR is selecting spin system preparative methods that present advantageous contrast. Sometimes these are combinations of the various basic contrasts and at other times, they may be a single and pure contrast. The three contrast MR images are displayed in Figure 2.2.

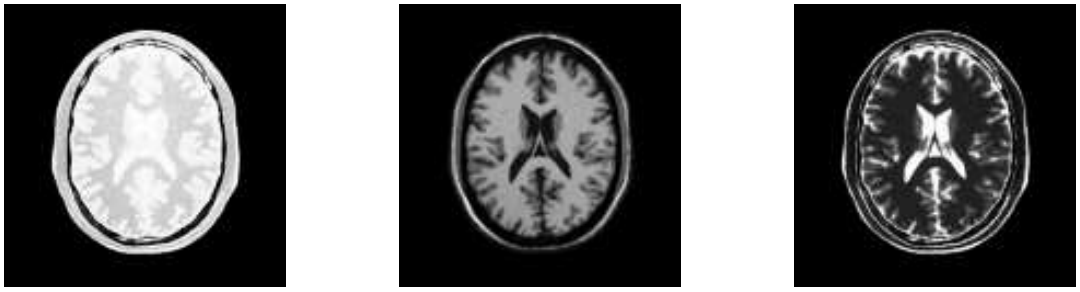

(a) (b) (c)

Figure 2.2: *The MR images using specific imaging techniques (a) Spin Density, (b) T1-weighted, (c) T2-weighted*

Spin Density

Spin density or Photon Density (PD) is the most like Computed Tomography (CT) of all the MR contrast parameters. The spin density is simply the number of spins in the sample that can be detected. The observed spin density in medical imaging is

always less than the actual spin density due to the fact that many spins are bound and lose signal before they can be observed.

$T1$ Relaxation

$T1$ represents the return of net magnetization vector in z-direction to its thermal equilibrium state. After the spins are tipped into the transverse plane, the spin vector $M_z(t)$ is depleted. If the spins are not tipped into the transverse plane again, the M_z^0 signal will regrow exponentially with a time constant $T1$:

$$M_z(t) = M_z^0(1 - e^{t/T1}) + M_z(0)e^{-t/T1} \tag{2.14}$$

where $T1$ is the longitudinal relaxation rate. The $M_z(t)$, called longitudinal magnetization, is the source of the signal. If $M_z(t) = 0$, the next repetition of the experiment will yield no signal because there will be no $M_z(t)$ to rotate into the transverse plane. The $M_z(t)$ vector is 99% of its equilibrium value M_z^0 when the t is five times $T1$. The mechanism for relaxation is the interaction between the excited spins and the stationary spins, referred to as lattice. The amount of interaction with the lattice is the determining factor in $T1$. In biological systems, water molecules come into frequent contact with the lattice and thus have relatively short $T1$ times. The $T1$ times for biological tissues tend to increase as the inverse square of the field strength. The $T1$ times of a sample increases as H_0 increases.

$T2$ Relaxation

The transverse relaxation time $T2$ represents the loss of coherence or de-phasing of spin leading to the net zero vector in the x-y plane. The transverse magnetization vector with respect to the relaxation times in the actual stationary coordinate system can be given by

$$M_{x,y}(t) = M_{x,y}(0)e^{-t/T2}e^{-i\omega_0 t} \tag{2.15}$$

$M_{x,y}(0)$ represents the initial transverse magnetization vector with the time set to zero at the end of the RF pulse of duration τ_p.

2.4 MR Image Encoding Techniques

To obtain MR images, a spatial encoding has to be established between the object and image coordinate systems. The spatially encoded locations or volumes are first excited through RF pulses and then accessed to acquire the FID signal during the relaxation phase for image reconstruction. Various sequences of RF pulses for spatial encoding and signal acquisition have been designed for MR imaging. The encoding of the NMR signal has to be performed in all three dimensions to scan the object and reconstruct its 3-D images. The NMR has two basic features: the frequency and the phase. There are two basic methods of spatial encoding in MR imaging: Frequency Encoding and Phase Encoding.

Frequency Encoding

In frequency encoding, a linear gradient is applied throughout the imaging space along a selected direction. The Larmor frequency is dependent on the net magnetic field at the location of the spinning nuclei. If a linear gradient is superimposed on the stationary magnetic field of the external magnet, the net magnetic field is spatially encoded along the direction of the gradient and consequently the effective Larmor frequency of spinning nuclei is spatially encoded along the same direction. Thus a linear gradient is used along the z-direction for slice selection for axial imaging after which x- and y-directions are to be spatially encoded for 3-D imaging. This is accomplished by further encoding the phase of the spinning nuclei along the x-direction of the selected slice whereas the spatial encoding in the y-direction is provided by another linear frequency encoding gradient along the y-direction.

Phase Encoding

The phase encoding gradient is applied as a constant step gradient in the direction in which all of the spinning nuclei are spinning with the same Larmor frequency. A fixed magnitude of the gradient changes the phase of the spinning nuclei by a respective fixed amount. Since the spatial encoding in two directions is provided by linear frequency-encoding gradients, a step function based gradient field is applied in the third direction for pulse encoding to acquire NMR signals for 3-D scanning and imaging. The phase encoding is applied in steps with repeated cycles.

2.5 MR Imaging Techniques

Spin Echo Imaging

Spin Echo is a most commonly used method in MR Imaging. The given slice of the brain in object coordinate system is selected by applying a linear frequency-encoding gradient in the z-direction. Along with the gradient, a 90-degree pulse can be applied to cause nuclear excitation in the entire slice volume. The 90-degree pulse causes the spinning nuclei to precess in phase. The spinning nuclei start dephasing in the transverse direction while the net longitudinal magnetization vector start returning to the state of thermal equilibrium. A 180-degree pulse is applied along the z-direction before the spinning nuclei lose their coherence. The transverse magnetization vector is flipped in the reverse direction and the spinning nuclei start re-phasing themselves to produce an echo after the time lag between the 90-degree and 180-degree pulses. The time for echo formation, T_E is defined between the application of the 90-degree pulse and the formation of echo (re-phasing of nuclei). The spinning nuclei are provided some time for longitudinal and transverse relaxations to bring close to thermal equilibrium before the next pulse sequence for echo formation is started. The time period between the applications of two consecutive

spin echo pulse sequences is called cycle repetition time, T_R. The manipulation of T_E and T_R provides different weighting of $T1$ and $T2$ relaxation times. $T2$ weighted MR imaging requires a long T_R and long T_E based spin echo pulse sequence. On the other hand, a short T_R and a short T_E based spin echo pulse sequence provide $T1$ weighted MR imaging. The long T_R and short T_E based spin echo pulse sequence provide spin-density MR images. A short T_R and long T_E based spin echo pulse sequence is not used for MR imaging. The echo signal density can be expressed as

$$\rho(x, y, z) = \rho_0(x, y, z)\{e^{-\frac{T_E}{T2}}\}\{1 - e^{-\frac{T_R}{T1}}\} \tag{2.16}$$

where $\rho_0(x, y, z)$ is the initial spin density function. $T1$ weighted, $T2$ weighted and spin density MR images of the same slice provide different tissue contrast in the respective images. This is a very useful feature in diagnostic radiology for lesion detection and characterization.

Echo Planar Imaging

Echo Planar Imaging (EPI) is a single-shot fast scanning method for 2-D and 3-D MR imaging. Multiple echoes are obtained with a single 90-degree RF selective pulse through an oscillating gradient rather than through application of a 180-degree phase reversal pulse as done in the spin-echo pulse sequences. This method creates a trajectory in the k-space to provide raw data points. The trajectory creates sub-sampling of the frequency space. However the entire image can be obtained in a single shot. Due to the signal decay by the $T2$ relaxation time, the number of sampling points in the k-space is limited. This limitations causes low-resolution images with some degradation.

Gradient Echo Imaging

Gradient echo imaging method is applied to FLASH (Fast Low Angle Shot) imaging pulse sequences. Flash pulse sequence uses a low flip-angle (as low as 20 degrees) RF

selective pulse for nuclear excitation. The frequency encoding gradient is applied along the z-direction for slice selection. The slice selection gradient G_z is inverted after the RF pulse to help re-phasing of spinning nuclei. Multiple echoes are created in repeated cycles to collect the data required for reconstruction. Thus there are more sampling points in the k-space available to reconstruct images at higher resolution. The entire pulse sequence time is much shorter than the spin echo pulse sequence, typically in the range of 10-20 msec.

2.6 Factors affecting MR signal

There are several factors that affect the MR signal acquisition causing artifacts or degradation in the reconstructed image. These factors include field inhomogeneities, flow of nuclei and change in resonance parameters due to chemical shifts within the object.

- Magnetic field inhomogeneities and gradient fields cause a direct de-phasing effect to the transverse relaxation process. The effective transverse relaxation time $T2^*$ from the field homogeneities can be expressed as

$$\frac{1}{T2^*} = \frac{1}{T2} + \frac{\gamma \Delta H}{2} \tag{2.17}$$

  where ΔH are the field inhomogeneities representing the maximum deviation of the field strength over the imaging volume. When a spatial encoding gradient is applied along any direction to localize the distribution of nuclei, the transverse relaxation time is further reduced to $T2^{**}$ and can be expressed as

$$\frac{1}{T2^{**}} = \frac{1}{T2^*} + \frac{\gamma G d}{2} \tag{2.18}$$

  where G is the strength of the gradient field applied over the region of diameter d.

- Magnetic susceptibility caused by the presence of other substances in the imaging medium is another important factor influencing the relaxation times.

- The presence of a molecular or chemical environment that can change the characteristic magnetic influence on the protons called Chemical Shift, can cause minor deviations in the Larmor frequency of spinning protons depending on their molecular environment. To minimize artifacts caused by chemical shift phenomenon, larger bandwidth frequency encoding is done in MR pulse sequences with short echo times.

2.7 Brain Anatomy and MRI

The application of Magnetic Resonance Imaging (MRI) has evolved rapidly since its clinical development in the early 1980s for diagnosis of various diseases [66, 67]. One of the least accessible and most complex organs, the human brain is a primary beneficiary of this new medical imaging technique. MRI, with its excellent soft tissue contrast, non-invasive character, high spatial resolution and easy slice selection at any orientation, is a powerful imaging technique for studying brain disorders such as Alzheimer's disease, multiple sclerosis, schizophrenia, congenital abnormality, visual loss, hearing loss, brain tumor etc. Brain contains three main soft tissue classes such as White matter (WM), Grey matter (GM) and Cerebrospinal fluid (CSF) [117, 118]. It is necessary to measure the amount of Grey matter, white matter and cerebrospinal fluid as well as their spatial distribution and temporal changes for diagnosis of various brain illness [118]. A quantitative MRI study shows that brain GM and WM volume loss accelerates with aging in chronic alcoholics [117]. Similarly men and women have different volumes of GM and WM which helps to study the sex difference from the percentage and asymmetry of the principal tissue volumes [117]. The three tissue classes of the brain is illustrated in Figure 2.3.

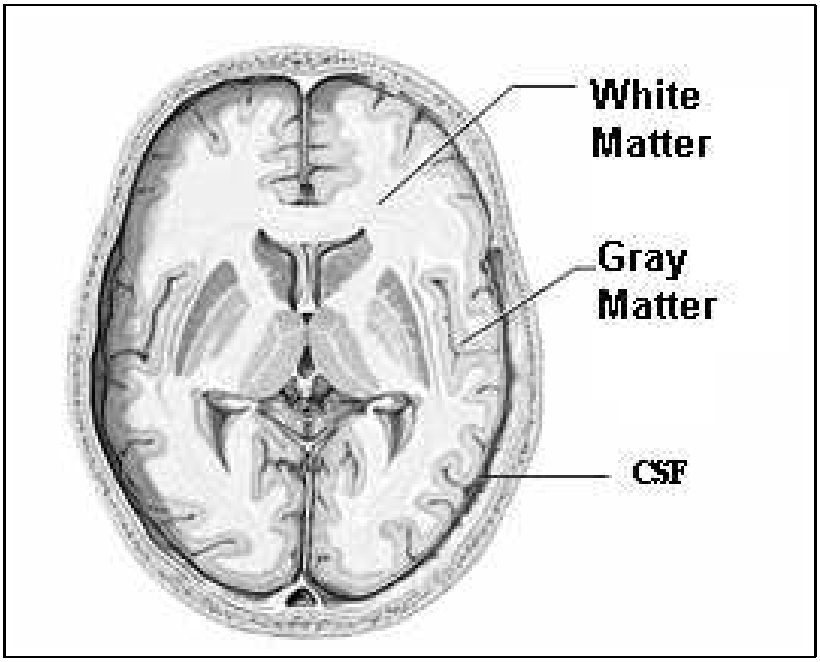

Figure 2.3: *A view of Brain illustrating the brain tissues; GM, WM and CSF*

- White matter in the brain consists mostly of axons with their envelope of myelin. Axons are extensions of neurons that reside within the Grey matter of the brain. The myelin sheath has an alternating layers of proteins and lipid. The ratio of lipid to protein is quite high, ranging from 70% to 80% lipid and 20% to 30% protein. As a result myelin is relatively dehydrated. It results more signal intensity on T2-weighted and less signal intensity on T1-weighted images.

- Outer layer of the brain is known as Gray matter which is formed by multiple neuron cell bodies. It covers the white matter. It is composed of 80% water, 10% protein and 10% phospholipid. Thus, in T1-weighted images, grey matter appears darker than white matter. In T2-weighted images, the white matter appears darker than grey matter [116].

- Cerebrospinal fluid is a clear and colourless fluid within the brain that cushions and supports the brain from jolts inside the skull. It consists of glucose,

(a) (b) (c)

Figure 2.4: *Brain MRI viewed from three directions; (a) Axial view, (b) Sagittal view, (c) Coronal view*

salts, enzymes and few white blood cells. As CSF has a very high water concentration, it appears dark and bright in T1-weighted and T2-weighted images respectively [116].

As the relative contrast between brain tissues is not constant in MR imaging, the choice of the strength and timing of the radio frequency pulses highlights some type of tissues or image over others, according to the clinical application. T1-weighted MRI offers the highest contrast between the brain soft tissues. On the contrary, T2-weighted and Photon Density (PD) images exhibit very low contrast between GM and WM, but high contrast between CSF and brain parenchyma.

Brain MRI can be viewed in three different planes such as axial plane, sagittal plane and coronal plane as depicted in Figure 2.4. Axial or transverse views (taken from the top of the head) are generally best for evaluating abnormal signal or morphology in the brain. Coronal (viewed from the back of the head) and sagittal (viewed from the side of the head) planes are suitable for evaluating posterior fossa of the brain. The coronal images allow right and left symmetry and mid-line structures to the best advantage.

Chapter 3

Background on Markov Random Field and Hidden Markov Model

3.1 Introduction

Image Segmentation techniques using spatial interaction models like Markov Random Field (MRF) and Gibbs Random Field (GRF) to model the image have become very popular recently. The use of contextual information is indispensable in low level as well as high level Image Processing. Markov Random Field theory provides a convenient and consistent way of modeling the entities with contextual constraints. This is achieved through characterizing mutual relationship among such entities such as pixels of an image and other spatially correlated features using MRF probabilities. MRF forms a probabilistic model for a set of variables that interact on a lattice structure. This started with the influential work of Geman & Geman [11] who linked via statistical mechanics between mechanical systems and probability theory. The distribution for a single variable at a particular site is conditioned on the configuration of a predefined neighbourhood surrounding that site.

The use of hidden Markov model (HMM) is a powerful modern statistical technique that has been found to be extremely useful for a wide spectrum of applications in ecology, crypt analysis, image understanding, speech and handwriting recognition. Formally, a hidden Markov model, as defined by Rabiner [26], is a doubly embedded

stochastic process with an underlying process that is not observable (it is hidden), but can only be observed through another set of stochastic process that produce the sequence of observations. It is a statistical model where the system being modeled is assumed to be Markov process with unknown parameters, and the challenge is to determine the hidden parameters, from the observable parameters, based on the assumption. This chapter gathers together the background information of Markov Random Field and Hidden Markov Model.

3.2 Markov Random Field

Let consider a collection of random variables $\{X_{ij}\}$, that is a random field defined over a finite discrete rectangular lattice S of size $(M \times N)$. The lattice S is defined as $S = \{(i,j) : 1 \leq i \leq M, 1 \leq j \leq N\}$, where site (i,j) corresponds to each pixel of the discrete image lattice structure. A neighbourhood system η on this rectangular lattice S can be defined as follows.

Definition 1 *A collection of subsets of S described as $\eta = \{\eta_{i,j} : (i,j) \in S, \eta_{i,j} \subset S\}$ is a neighborhood system on S if and only if $\eta_{i,j}$, the neighborhood of pixel (i,j), is such that*

1. a site is not neighboring to itself : $(i,j) \notin \eta_{ij}$
2. the neighboring relationship is mutual : If $(k,l) \in \eta_{ij}$, then $(i,j) \in \eta_{kl}$ for any $(i,j) \in S$

The neighbor set of η_{ij} is defined as the set of nearby sites within a radius r such that $\eta_{ij} = \{(k,l) \in S \mid \{dist((i,j),(k,l))\}^2 \leq r, (i,j) \neq (k,l)\}$, where dist$(A,B)$ denotes the Euclidean distance between A and B, r takes an integer value. A hierarchically ordered sequence of neighborhood systems is shown in Figure 3.1. where η^1, η^2, η^3.... are the "first-order", "second-order", "third-order"..... neighborhood

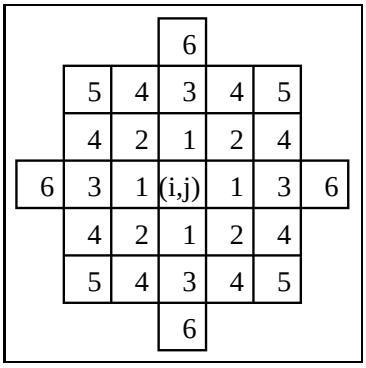

Figure 3.1: *Hierarchically arranged neighborhood system of Markov Random Field*

systems respectively and are denoted by numbers 1,2,3....as shown in Figure 3.1 Due to the finite lattice used, the neighborhood of pixels on the boundaries are necessarily smaller unless a toroidal (periodic) lattice structure is assumed. A nearest neighborhood dependence of pixels on an image lattice is obtained by going beyond the assumption of statistical independence. The neighborhood systems that can be defined over S are neither limited to the hierarchically ordered sequence of neighborhood systems, nor they have to be isotropic or homogeneous.

Definition 2 *Let η be a neighborhood system defined over lattice S. A random field $X = \{X_{i,j}\}$ defined over lattice S is a Markov Random Field (MRF) with respect to the neighborhood system η if and only if*

1. All of its realizations have nonzero probabilities:

   $P(X = x) > 0$ for all x (property of Positivity)

2. Its conditional distribution satisfies the following property:

   $P\{X_{ij} = x_{ij} \mid X_{kl} = x_{kl}, (k,l) \in S, (k,l) \neq (i,j)\}$

   $= P\{X_{ij} = x_{ij} \mid X_{kl} = x_{kl}, (k,l) \in \eta_{ij}\}$ for all $(i,j) \in S$ (property of Markovianity)

where x_{ij} is the configuration corresponding to the random variable X_{ij} and so on.When the positivity condition is satisfied, the joint probability $P(X)$ of any

random field is uniquely determined by its local conditional probabilities [14].

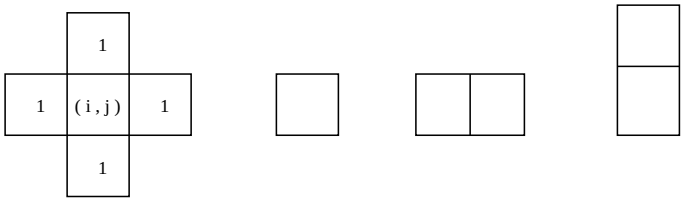

Figure 3.2: *Cliques associated with first-order neighbourhood system*

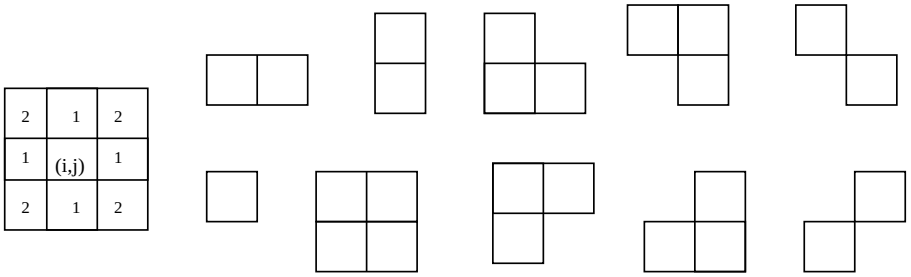

Figure 3.3: *Cliques associated with second-order neighbourhood system*

The Markovianity depicts the local characteristics of X which is characterized by the conditional distributions. The *Definition 2* says that the image value at a pixel does not depend on the image data outside its neighborhood, when the image data on its neighborhood are given. Hence, the most attractive feature of MRF is that *"images tend to have a degree of cohesiveness: pixels located near to each other tend to have the same or similar colours"* [11]. It does not constitute a theoretical restriction either, because all random field satisfy *Definition 2*, with respect to a large enough neighborhood system, e.g. $\eta_{i,j} = S$ for all $\eta_{i,j} \in S$. On the other hand, MRF models, even with respect to small neighborhood systems such as η^2 prove to be very flexible and powerful. Let us define the *clique* associated with (S, η), a lattice neighborhood system pair:

Definition 3 A *clique of the pair* (S, η) *denoted by* c *is a subset of* S *such that*

1. c *consists of a single pixel, or*

2. *for* $(i,j) \neq (k,l)$, $(i,j) \in c$ *and* $(k,l) \in c$ *implies that* $(i,j) \in \eta_{k,l}$

The collection of all cliques of (S,η) is defined by $C(S,\eta)$. The clique types associated with first-order and second-order neighborhood systems are shown in Figure 3.2 and Figure 3.3 respectively.

3.3 Gibbs Random Field

Gibbs Distribution (GD) or equivalently the Gibbs Random Field (GRF) can be defined as follows.

Definition 4 *Let* η *be a neighborhood system defined over a finite lattice* S. *A random field* X *is said to be a Gibbs Random Field (GRF) on lattice* S *with respect to a neighborhood system* η *if and only if its configuration obey a Gibbs distribution which has the following form*

$$P(X = x) = \frac{1}{Z} e^{-\frac{1}{T}U(x)} \tag{3.1}$$

where,

$$Z = \sum_{x} e^{-\frac{1}{T}U(x)} \tag{3.2}$$

is the partition function. Z is simply a normalizing constant so that the sum of the probabilities of all realizations, x becomes one. T is a constant analogous to temperature which shall be assumed to be 1 unless otherwise stated and $U(x)$ is the energy function or Hamiltonian of a Gibbs distribution, which can be expressed as follows

$$U(x) = \sum_{c \in C} V_c(x) \tag{3.3}$$

Hence, energy is sum of clique potentials $V_c(x)$ over all possible cliques C. $V_c(x)$ are a set of potential functions depending on the values of x at the sites in the clique c. Thus, the key functions in determining the properties of the distribution are the potential functions $V_c(x)$. $P(x)$ measures the probability of the occurrence

of a particular configuration x. The more probable is a particular configuration, has lesser energy. This is so because the energy is computed as a measure of the distance between the model and the raw image data. The potential functions are chosen to reflect the desired properties of the image so that the more likely images have a lower energy and are thus more probable. The temperature T controls the sharpness of the distribution. When the temperature is high, all configurations tend to be equally distributed and when it gradually decreases to zero, global energy minima is achieved. Gibbs energy formalism has the added advantage that if the likelihood term is given by an exponential, and the prior is obtained through a MRF model, the posterior probability continues to be a Gibbsian. This makes the MAP estimation problem equivalent to an energy minimization.

3.4 Markov-Gibbs Equivalence

Markov Random Field (MRF) is characterized by its local property (the Markovianity) whereas Gibbs Random Field (GRF) is characterized by its global property (the Gibbs distribution). Hammersley-Clifford's famous theorem [14] (unpublished by the original authors) states that "*given the neighbourhood structure η of the model, for any set of sites within the lattice S, their associated contribution to the Gibbs energy function should be non zero, if and only if the sites form a clique; a random field's having the Markov property is equivalent to its having a Gibbs distribution*". This theorem establishes the equivalence of these two types of properties and provides a very general basis for the specification of MRF joint distribution function. Many have been used throughout the literature [9]. The difficulties inherent in the MRF formulation are eliminated by use of this equivalence which are as follows:

1. Readily availability of joint distribution of random field

2. Obtaining local characteristics regardless of inconsistency

3. Characterizing the Gibbs Distribution model with few parameters

By use of this equivalence MRF theory provides a mathematical foundation for solving the problem of making a global inference using local information. It follows from the above equivalence that the local characteristics of the MRF are readily obtained from the joint distribution in 3.1 as

$$\begin{aligned} P(X_{i,j} = x_{i,j} \mid X_{k,l} = x_{k,l}\ (k,l) \in S,\ (k,l) \neq (i,j)) \\ = P(X_{i,j} = x_{i,j} \mid X_{k,l} = x_{k,l},\ (k,l) \in \eta_{i,j}) \\ = \frac{e^{-\sum_{c \in C} V_c(x)}}{\sum_{x_{i,j} \in S} e^{-\sum_{c \in C} V_c(x)}} \end{aligned} \tag{3.4}$$

3.5 Line Process

Smoothness is a generic assumption in MRF models [11, 17] which characterizes the spatial coherence and homogeneity of image lattice. However improper imposition of it can lead to undesirable, over-smoothed solutions. It is necessary to take care of discontinuities when using smoothness prior. To avoid the problem of over-smoothing Geman and Geman [11] proposed combining the underlying MRF (intensity process) with an additional "line process".

The line process is neither a data nor the target of estimation. Rather, it is an auxiliary process which is coupled to the intensity process in such a manner that the joint probability distribution of intensity function is locally smooth with line process for discontinuities. The prior on the line process is often selected to emphasize continuous lines and to reject spurious edge elements. Such a model has the desirable property of promoting structure within the image without causing over-smoothing. A couple of MRFs are defined on the image lattice, one is for intensity or label field , other is the dual lattice for the edge field or "line field" which are depicted in Figure 3.4. A line process comprises a lattice S' of random variable

$f \in F$, whose sites $i' \in S'$ corresponded with vertical and horizontal boundaries between adjacent pixels of the image lattice. It takes the values from $\{0, 1\}$ which signifies the absence or occurrence of edges. $f_{i'} = 1$ of the line process variable indicates that a discontinuity is detected between neighbouring pixels j and i ,i.e. $V_{(i,j)}(x_i, x_j)$ is considered as 0 or the bond between two pixels is 0; $f_{i'} = 0$ indicates continuity between above two pixels and $V_{(i,j)}(x_i, x_j)$ is taken same as before.

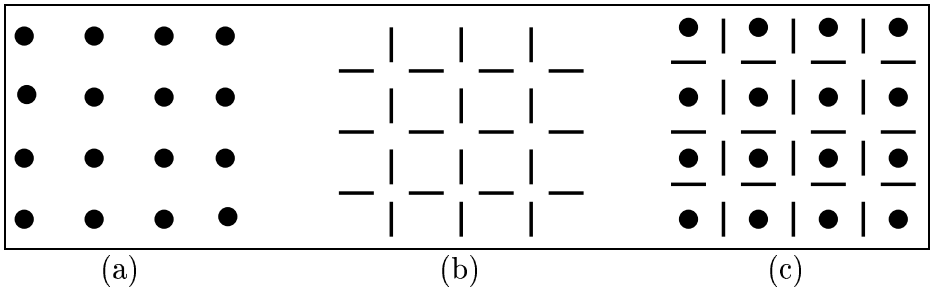

Figure 3.4: *A realization of a binary line field: (a) label field, (b) line field, (c) MRF with line field*

Another neighborhood N is defined over the dual lattice S' for line sites. Each pixel has four line site neighbors. Image lattice can be represented as $S \; U \; S'$. The (3.1) can be represented with the incorporation of line field as

$$P(X = x, F = f) = \frac{1}{Z} e^{-\frac{1}{T}U(x,f)}. \tag{3.5}$$

The resulting MAP estimation can therefore be defined using a Gibbs posterior distribution whose prior energy function is

$$U(x, f) = U(x|f) + U(f). \tag{3.6}$$

Assignment of line field is preferred as it results in smaller energy and better estimation. The fundamental concepts underlying a line process were further addressed by Geman and Reynolds [13]. They suggested the proper potential function for cost measurement, giving a prior on the line process, to provide the ability to model rapid transitions in gray level.

3.6 Gibbs Sampler

To implement the Relaxation algorithm, Geman and Geman [11] developed the Gibbs Sampler to explore the energy surface. The interpretation of the Theorems derived by them are as follows.

- The interpretation of the **Theorem A** is *"At a constant temperature, if each site of an image lattice is visited infinite times, as time to infinity, the configuration X will be a sample from the Gibbs distribution and this distribution is independent of the initial configuration".*

- The interpretation of **Theorem B** is *"To reach equilibrium state with lowest energy, the temperature is forced to decrease slowly. As time to infinity, X will be a sample from the Gibbs distribution at temperature absolute zero degree or the Gibbs distribution with minimum energy".*

The Gibbs sampler works by updating each random variable individually, but conditional on the states of the surrounding sites. The sequential implementation corresponding to a raster scan is used for Gibb's sampler. The state of image evolves by discrete changes. So for convenience time is discretized, say $t = 1, 2, 3.....$ At a given time, each site $x_{i,j}$ is represented by a random variable $X_{i,j}(t)$ with values in $G = 0, 1, 2...., n-1$. Hence the total configuration of the image is $X(t) = \{x_{i,j}(t)\};\ i, j \in S$. The starting configuration $X(0)$ is arbitrary and at any time t, the total configuration $X(t)$ evolves due to state change of individual site. At any instant of time only one site undergoes (possible) change. So the state at any two consecutive instant of time t and $t-1$ can differ by at most one coordinate. If $n_1, n_2, ...$ be the sequence in which the sites are visited for replacement; thus $n_t \in S$ and $X_{i,j}(t) = X_{i,j}(t-1), i \neq n_t$. For replacement at each site a sample is drawn from its local characteristics. In other words, a state $x \in Gn_t$ is chosen from the

conditional distribution of X_{n_t}. Given the observed states of the neighboring sites. All other sites remaining unchanged, the change in total energy is the changes due to change at site n_t with respect to its neighborhood. Let $U(t-1)$ is the old energy and $U(t)$ be the new one. If $U(t)$ is found to be less than $U(t-1)$, then the change is accepted; otherwise it is accepted with a probability to avoid the sampling to stuck in a local minimum. When all the sites of the image are visited once, one iteration is said to be completed.

3.7 Hidden Markov Model (HMM)

HMM is a finite set of states, each of which is associated with a (generally multidimensional) probability distribution. Transitions among the states are governed by a set of probabilities called transition probabilities. In a particular state an outcome or observation can be generated, according to the associated probability distribution. It is only the outcome, not the state visible to an external observer and therefore states are "hidden" to the outside; hence the name Hidden Markov Model. Basically it is an extension of observable Markov Model. The observation is a probabilistic function (discrete or continuous) of a state. All observations are dependent on the state that generated them, not on the neighboring observations. Considering an Image restoration problem, Figure 3.5 depicts the hidden Markov random field $\{X_i\}$ which represents the true, unknown image and we observe the random field $\{Y_i\}$, which is the observed degraded image. Hidden Markov models exploit the "locality" of physical properties of a system. They are often used to construct models of physical systems when the information about the system is gathered using an apparatus that distorts the physical reality being observed in some manner. Markov Random Field (MRF) theory provides a basis for modeling contextual constraints. It is commonly accepted that the pixel intensities in an image exhibit high spatial statistical

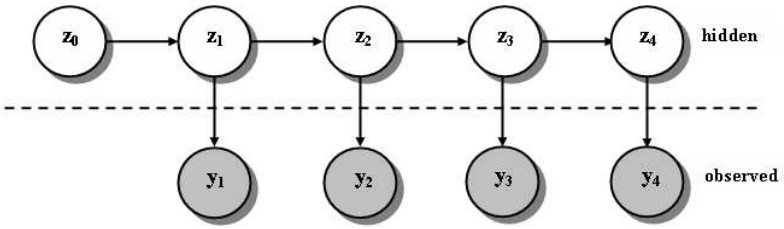

Figure 3.5: *Hidden Markov Model*

interdependence, i.e., background pixels have a high probability of occurring next to other background pixels. Likewise, pixels generally lie adjacent to other pixel. The key assumption is that a high spatial interdependence present in the image field can be easily incorporated into a MRF model. A description of MRF is given in section **3.1** before.

MRF is a multidimensional extension of Markov chain, but the generalization is complicated by the lack of a natural ordering of pixels in multidimensional space. Hidden Markov fields are a natural generalization of the HMM that have proved essential to the development of modern speech recognition, but again the multidimensional nature of the signals makes them inherently more complicated to handle. This added complexity contributed to the long time required for the development of successful methods and applications. Here, the output of the process is the set of states at each instant of time, when each state corresponds to an observable event and also the output in any given state is not random (deterministic). Consider a system having N distinct states as $S_1, S_2, ..., S_N$ which is illustrated in Figure 3.6 (with $N = 5$). At regularly spaced discrete times, the system undergoes a change of state (possibly back to the same state) according to a set of probabilities associated with the state. Let time instants associated with state changes as $t = 1, 2, ...$, and the actual state at time t is q_t. The probabilistic description depends on specification of the current state (at time t), as well as all predecessor states. For the special case of a discrete, first order, Markov chain, this probabilistic description is truncated to

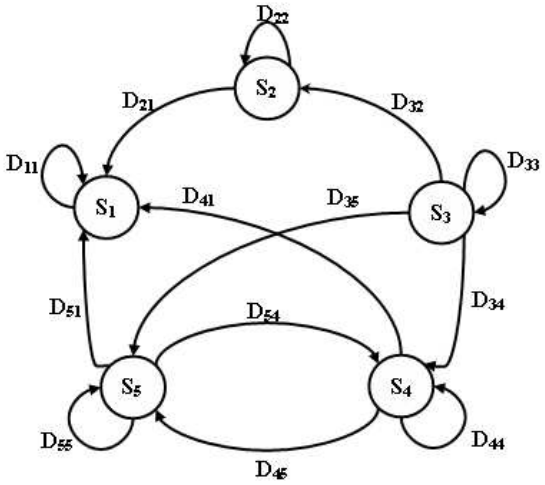

Figure 3.6: *State diagram of HMM*

just the current and the predecessor state, i.e.

$$P(q_t = S_i \mid q_{t-1} = S_{i,q_{t-2}} = S_{k,\ldots}) = P(q_t = S_j \mid q_{t-1} = S_i) \tag{3.7}$$

3.7 is independent of time and its set of state transition probabilities is

$$a_{i,j} = P(q_t = S_j \mid q_{t-1} = S_i), 1 \leq i, j \leq N \tag{3.8}$$

State transition coefficients obey standard stochastic constraints having the properties:

- $a_{i,j} \geq 0$
- $\sum_{j=1}^{N} a_{i,j} = 1$

The above stochastic process could be called an observable Markov model since the output of the process is the states at each instant of time, where each state corresponds to a physical (observable) event. In this section we extend the concept of Markov models to include the case where the observation is probabilistic function of the state, i.e. stochastic process with an underlying stochastic process that is not observable (hidden), but can only be observed through another state of stochastic

processes that produce the sequence of observations. Here, an example is produced for an better insight into the theory of Hidden Markov model.

Example: Coin Toss Model: Let a person X is performing a coin (or multiple coins) tossing experiment and another person Y is present in the room with a barrier through which he cannot see the event. The person X will not tell the person Y anything about the mode of experiment; rather tell only the result of each coin flip. Thus a sequence of hidden coin tossing experiments is performed, with the observation sequence consisting of a series of heads and tails. In this situation, the problem of interest is how to build an HMM to explain (model) the observed sequence of heads and tails. The first problem is to decide what the states in the model correspond to, and then to decide how many states should be in the model. One possible choice would be to assume that only a single biased coin was being tossed. In this case the situation is modeled with a 2-state model where each state corresponds to a side of the coin (head or tail). This model is depicted in Figure 3.7(a). Here, Markov model is observable and the only issue for complete specification of the model would be to decide on the best value for the bias (the probability of head or tail). An equivalent HMM to that of Figure 3.7(b) would be a degenerate l-state model, where the state corresponds to the single biased coin and the unknown parameter is the bias of the coin. A second form of HMM for explaining the observed sequence of coin toss outcome is given in Figure 3.7(b). In this case there are two states in the model and each state corresponds to a different, biased, coin being tossed. Each state is characterized by a state transition matrix. The physical mechanism which accounts for how state transitions are selected could itself be a set of independent coin tosses, or some other probabilistic event. A third form of HMM for explaining the observed sequence of coin toss outcomes is given in Figure 3.7(c). This model corresponds to using 3 biased coins, and choosing from among the three is based on some probabilistic event.

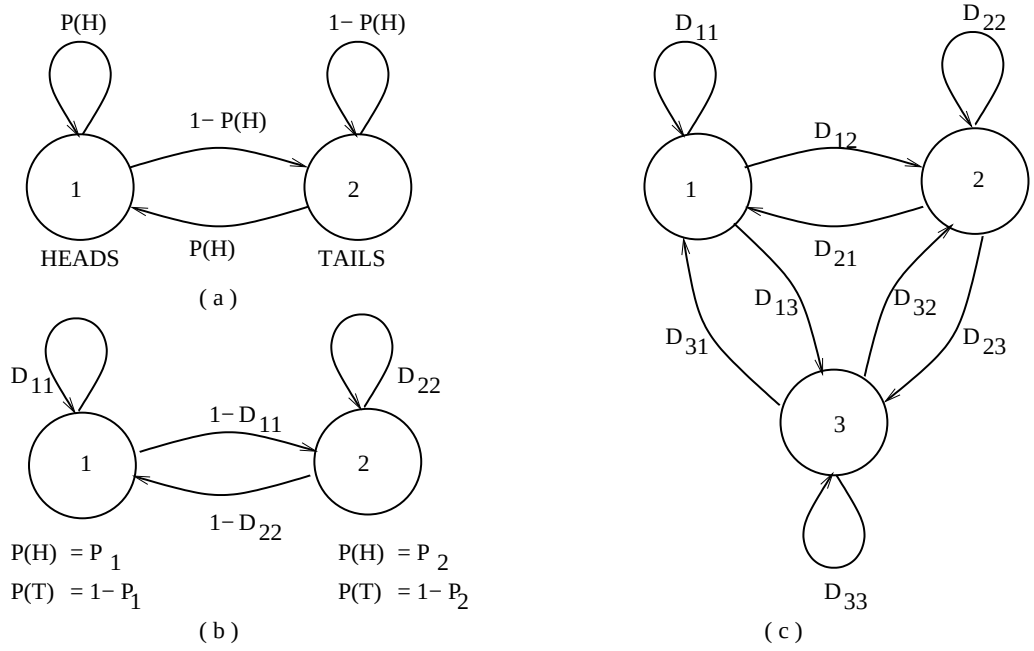

Figure 3.7: *Three Possible Markov Models which can account for the results of hidden coin tossing experiments: (a) 1-coins model, (b) 2-coins model, (c) 3-coins model*

STATE

$P(H)$	P_1	P_2	P_3
$P(T)$	$(1-P_1)$	$(1-P_2)$	$(1-P_3)$

Given the choice among the three models shown in Figure 3.7 for explaining the observed sequence of heads and tails, a natural question would be which model best matches the actual observations. It should be clear that the simple 1-coin model of Figure 3.7(a) has only 1 unknown parameter; the 2-coin model of Figure 3.7(b) has 4 unknown parameters; and the 3-coin model of Figure 3.7(c) has 9 unknown parameters. Thus, with the greater degrees of freedom, the larger HMMs would seem to inherently be more capable of modeling a series of coin tossing experiments than would equivalently smaller models. Although this is theoretically true, but practical considerations impose some strong limitations on the size of models that can be considered. Furthermore, it might just be the case that only a single coin is being tossed. Then using the 3-coin model of Figure 3.7(c) would be inappropriate,

since the actual physical event would not correspond to the model being used i.e., we would be using an underspecified system. A HMM is characterized by the following:

1. Although the states are hidden, for many practical applications there is often some physical significance attached to the states or to sets of states of the model. Hence, in the coin tossing experiments, each state corresponded to a distinct biased coin. Generally the states are interconnected in such a way that any state can be reached from any other state. We denote the individual states as $S = S_1, S_2, ..., S_N$ (assuming the model with N states) and the state at time t as q_t.

2. Assuming the number of distinct observation symbols per state as M, the observation symbols correspond to the physical output of the system being modeled. For the coin toss experiments the observation symbols were simply heads or tails, We denote the individual symbols as $V = V_1, V_2, ..., V_M$

3. The State transition probability distribution $A = a_{i,j}$ where

$$a_{ij} = P(q_t = S_j \mid q_{t-1} = S_i), 1 \leq i, j \leq N. \tag{3.9}$$

4. The observation symbol probability distribution in state $j, B = b_j(k)$, where

$$b_j(k) = P(V_k t \mid q_t = S_j), 1 \leq j \leq N, 1 \leq k \leq M. \tag{3.10}$$

5. The initial state distribution $\pi = \pi_i$ where $\pi_i = P(q_1 = S_i), 1 \leq j \leq N$.

Given appropriate values of N, M, A, B and π, the HMM can be used as a generator to give an observation sequence $O = O_1, O_2, ..., O_T$ where each observation Q_t, is one of the symbols from V_i, and T is the number of observations in the sequence.

- Choose an initial state $q_1 = S_i$ according to the initial state distribution π.

- Set $t = 1$.

- Choose $Q_t = V_k$ according to the symbol probability distribution in state S_i, i.e.,$b_j(k)$.
- Transit to a new state $q_{t+1} = S_j$ according to the state transition probability distribution for state S_i i.e., a_{ij}.
- Set $t = t+1$; return to third step if $t < T$; otherwise terminate the procedure.

It can be seen from the above discussion that a complete specification of a HMM requires specification of model parameters, specification of observation symbols and the specification of the three probability measures A, B, and π. For convenience, we use the compact notation $\lambda = (A, B, \pi)$ to indicate the complete parameter set of the model. Following are the basic problems of a HMM.

1. Given a model, how do we compute the probability of an observation sequence ?
2. Given a model as well as a set of observations, how do we find the best state sequence ?
3. Given a model and a set of training observation sequence, how do we find the parameters that maximize the probability of the model ?

Problem 1 can be viewed as the evaluation problem; how well a given model matches a given observation sequence. *Problem 2* can be viewed as the decoding problem; to find the optimal state sequence or to uncover the hidden part of the model for which an optimality criterion is imposed. *Problem 3* can be viewed as the learning problem; model parameters are optimized to find the best observation sequence. The hidden Markov model has been successfully applied in biosciences, climatology, econometrics, handwriting and text recognition, image processing and computer vision, signal processing and speech processing.

Chapter 4

Tabu Search Technique

4.1 Introduction

Many optimization problems in practice require large space and more computational time in nonlinear framework. Extensive effort has been directed towards the design of good heuristics, in other words algorithm efficient with respect to computing time and storage space. Tabu Search is a general heuristic search procedure devised for finding a global minimum of a function which may be linear or nonlinear in nature. The basic concept of Tabu Search as described by F.Glover [55] [56] is "*a meta-heuristic superimposed on another heuristic*". The overall approach is to avoid entrainment in cycles by forbidding or penalizing moves which take the solution, in the next iteration, to points in the solution space previously visited ("Tabu"). Glover attributes to the origin of Tabu Search in 1977. The method was partly motivated by the observation that human behaviour appears to operate with a random element that leads to inconsistent behaviour given similar circumstances. As Glover points out, the resulting tendency to deviate from a specific characteristics, might be regretted as a source of error but can also prove to be source of gain. The Tabu method operates in this way with the exception that new solutions are not chosen randomly. Instead The Tabu Search proceeds according to the supposition that there is no point in accepting a new (poor) solution unless it is to avoid a

path already investigated. This insures that new regions of solution space will be investigated with a goal of avoiding local minima and ultimately finding the desired solution.

The Tabu Search has traditionally been used on combinatorial optimization problems [57]. Many of the applications involve integer programming problem, scheduling, routing, traveling salesman and related problems like design of digital filter, cell image segmentation, speech recognition [62, 59, 61, 65]. Using Tabu Search has a greater probability of finding globally optimal parameters and achieves better performance than that of other globally convergent algorithms.

4.2 Notion of Tabu Search

Tabu Search explores the solution space by moving at each iteration from a solution s to the best solution in a subset of its neighbourhood $N(s)$. This procedure has a flexible memory to keep the information about the past steps of the search and uses it to create and exploit the new solutions in the search space. Contrary to the classical descent methods, the current solution may deteriorate from one iteration to the next. Thus, to avoid cycling, solutions possessing some attributes of recently explored solutions are temporarily declared Tabu or forbidden. The duration that an attribute remains Tabu is called its Tabu-tenure and it can vary over different intervals of time. The Tabu status can be overridden if certain conditions are met; this is called the "*aspiration criterion*". The Tabu Search begins by marching to a local minima. To avoid retracing the steps used, the method records recent moves in one or more Tabu lists. The original intent of the list was not to prevent a previous move from being repeated, but rather to insure it was not reversed. The Tabu lists are historical in nature and form the Tabu Search memory. The role of the memory is to restrict the choice to some subset of neighbourhood $N(s)$ by forbidding for

instance moves to some neighbour solutions. This systematic use of memory is an essential feature of Tabu Search. At initialization the goal is to make a coarse examination of the solution space, known as "*diversification*", but as candidate locations are identified the search is more focused to produce local optima solutions in a process of "*intensification*". In the search process it is sometimes fruitful to intensify the search in some region of S because it may contain some acceptable solutions. Such an intensification can be carried out by giving a high priority to the solutions which have common features with the current solutions. This can be done with the introduction of an additional term in the objective function which penalizes the solution far from the present one. Again diversification can be forced by introducing an additional term in the objective function which penalizes solutions close to the present one at some stage. In many cases the differences between the various implementations of the Tabu method have to do with size, variability, and adaptability of the Tabu memory to a particular problem domain.

4.3 Tabu Search Procedure

Initially the Tabu Search algorithm starts from a random point or move X_{ini} and the next point obtained from the set of the feasible solutions by applying simple modification to X_{ini}. This modification is called a 'move' and the next point X_1 is the 'new point'. In order to avoid the algorithm's move to a new point in the search space which has been visited earlier, a Tabu list is introduced. Every successful move is stored in the Tabu list. The new move obtained will now be compared with all the earlier moves stored in the Tabu list. If the new move matches with any move in the Tabu list, it is discarded. the next point is again introduced and if the new point does not matches, then it is considered as a new point in the solution space. The Tabu list is updated with the new set of solutions. The best valued solution is

selected as the next solution X_{next}. The moves stored in the Tabu list are the ones that were carried out most frequently and recently. Tabu Search procedure consists of the following steps.

Salient steps of Tabu Search

1. *Initialisation*

   Choose an initial schedule X_{ini} to be the current solution and compute the value of the objective function $F(X_{ini})$.

2. *Neighbour Generation*

   Select a neighbour X_{next} of the current solution and compute $F(X_{next})$.

3. *Acceptance Test*

   Test whether to accept the move from X_{ini} to X_{next}. If the move is accepted, then X_{next} replaces X_{ini} as the current solution; otherwise X_{ini} is retained as the current solution.

Its acceptance test is based on a Tabu list which is as follows.
Determine $\Delta = F(X_{next}) - F(X_{ini})$

1. If $\Delta < 0$ and X_{next} is non-Tabu, then a move to X_{next} is always accepted.

2. If $\Delta < 0$ and X_{next} is Tabu, then a move to X_{next} may be accepted for a promising schedule X_{next} (if $F(X_{ini})$ is less than the objective function value for any other solution obtained before).

3. If $\Delta >= 0$ and X_{next} is Tabu, then a move to X_{next} is always rejected.

4. If $\Delta >= 0$ and X_{next} is non-Tabu, then a wait and see approach is adopted: X_{next} remains as a candidate while the search continues for a neighbour which can be accepted immediately. If no such neighbour is found, a move to the best candidate X_{next} is made.

Chapter 5

Supervised Image Segmentation using HMRF model

5.1 Introduction

Segmentation is the process of splitting an observed image into its homogeneous or constituent regions. It is a basic early vision problem that has received attention of researchers for quite sometime. Often, model based approaches have been adhered to obtain proper segmentation. In this regard, the problem is cast as a pixel labeling problem and the segmentation problem reduces to estimation of the pixel labels. In model based framework, the segmentation problem can be viewed as supervised one when the model parameters are either assumed to be known or estimated *a priori*. These parameters are used to obtain the estimates of the image labels and hence segmentation. Different deterministic and stochastic models have been employed successfully for image segmentation. In the stochastic paradigm, Markov Random Field model and its variants have been extensively used for image segmentation. Often, Gauss Markov Random Field (GMRF) models have been used. In this chapter, Gauss Hidden Markov Random Field (GHMRF) model as proposed by Zhang *et al.* [95] has been employed while formulating the image segmentation problem. The image segmentation is formulated using MAP estimation criterion. It is a tedious task to obtain the MAP estimates and toward this end, a Hybrid Tabu Search (HTS)

algorithm is proposed. The algorithm is successfully tested with synthetic as well as brain MR images. The performance of the proposed algorithm is compared with Simulated Annealing (SA) and Iterated Conditional Mode (ICM) algorithm.

5.2 HMRF Image Model

Hidden Markov Models(HMM) are already been described in Chapter 3. Here, a special case of HMM is considered, where the underlying stochastic process is a MRF instead of a Markov chain and therefore, not restricted to one dimension. This special case is referred to as Hidden Markov Random Field (HMRF) model [95]. Let the images are assumed to be defined on a discrete rectangular lattice $S = (N \times N)$. Let $X = \{X_i, i \in S\}$ denote the random field associated with the noise free class labels of the original image, X_i is the random variable of i^{th} site and, $x = \{x_i, i \in S\}$ is the realization of X. The label process X is assumed to be MRF with respect to a neighborhood system η and is described by its local characteristics.

$$P(X_i = x_i \mid X_j = x_j,\ j \in S,\ j \neq i) = P(X_i = x_i \mid X_j = x_j,\ j \in \eta_i) \tag{5.1}$$

Since X is a MRF, or equivalently Gibbs distributed, the joint distribution can be expressed as

$$P(X = x \mid \phi) = \frac{1}{Z} e^{-U(x,\phi)}$$

where $Z = \sum_x e^{-U(x,\phi)}$ is the partition function, ϕ denotes the clique parameter vector, $U(x, \phi)$ is the energy function and is of the form $U(x, \phi) = \sum_{c_i \in C} V_c(x, \phi)$, and $V_c(x, \phi)$ is the clique potential. Let $Y = \{Y_i, i \in S\}$ denote the observed random field and y be the realization of it. Given $X_i = l$, Y_i follows a conditional probability distribution

$$P(y_i \mid l) = f(y_i;\ \theta_l) \qquad \forall \quad l \in L \tag{5.2}$$

where $L = \{1, 2, ...l\}$ denote the set of all labels and θ_l is the set of parameters. For all l, the family of functions $f(.; \theta_l)$ has the same known analytic form. It is also assumed that (X, Y) is pairwise independent,

$$P(y, x) = \prod_{i \in S} P(y_i, x_i) \tag{5.3}$$

Given any particular configuration $x \in X$, every Y_i follows a known conditional probability distribution $p(y_i \mid x_i)$ of the same functional form $f(y_i;\ \theta_{x_i})$ where θ_{x_i} are the involved parameters. For any potential realization x, the random variables Y_i are conditionally independent

$$P(y \mid x) = \prod_{i \in S} P(y_i \mid x_i) \tag{5.4}$$

The joint probability of (X, Y) can be expressed as

$$P(y, x) = P(y \mid x)P(x) = P(x) \prod_{i \in S} P(y_i \mid x_i)$$

According to the local characteristics of MRF, the joint probability distribution of pair (X_i, Y_i) given the neighborhood configuration of X_{η_i} is

$$P(y_i, x_i \mid x_{\eta_i}) = P(y_i \mid x_i)P(x_i \mid x_{\eta_i}) \tag{5.5}$$

Thus, the marginal probability distribution of Y_i dependent on θ and X_{η_i} is

$$P(y_i \mid x_{\eta_i}, \theta) = \sum_{l \in L} P(y_i, l \mid x_{\eta_i}, \theta) = \sum_{l \in L} P(y_i \mid l, \theta)P(l \mid x_{\eta_i}) \tag{5.6}$$

where $\theta = \{\theta_l, l \in L\}$, L denotes the number of labels. (5.6) is the Hidden Markov Random Field model [95]. With Gaussian distribution, (5.6) can be expressed as

$$p(y_i \mid x_{\eta_i}, \theta) = \sum_{l \in l} g(y_i, \theta_l)P(l \mid x_{\eta_i}) \tag{5.7}$$

(5.7) is refereed to as the Gaussian Hidden Markov Random Field (GHMRF) model, where $g(y_i;\ \theta_l)$ is the Gaussian probability density function.

5.3 Image Label Estimation

Since in supervised framework the model parameters are assumed to be known, it is required to estimate the pixel labels using the associated model parameters. Let X be the random field associated with the noise free class label and x be the realization of the same. X is modeled as a MRF. Let Y denote the observed image random field and y be the realization of it. Y is modeled as Gauss Hidden Markov Random Field (GHMRF). Let θ be the associated model parameters. In the pixel labeling problem, let x^* denote the true but unknown labeling configuration and $\hat{x}$ denote the estimate for x^*. x^* is the realization of random field X, which is modeled as MRF. The problem is to recover x^* from the observed image y. The following optimality criterion is adopted,

$$\hat{x} = arg \max_{x} P(x \mid y, \theta) \tag{5.8}$$

where the model parameters for each class $\theta_l = [\mu_l, \sigma_l]$ are selected on an ad hoc basis. Since X is unknown, the posteriori probability distribution $P(x \mid y, \theta)$ can not be evaluated. Hence, using Baye's rule, (5.8) can be expressed as

$$\hat{x} = arg \max_{x} \frac{P(y \mid x, \theta)P(x)}{P(y)} \tag{5.9}$$

Since Y is known, the denominator of (5.9) is a constant. Thus, (5.9) can be written as

$$\hat{x} = arg \max_{x} P(y \mid x, \theta)P(x) \tag{5.10}$$

Since,X is MRF, the prior probability distribution in (5.10) is given as $P(x) = \frac{1}{Z}e^{-U(x)}$. It is also assumed that the pixel intensity y_i follows a Gaussian distribution with parameters $\theta_l = \{\mu_l, \sigma_l\}$. Given the class label $x_i = l$,

$$P(y_i \mid x_i) = \frac{1}{\sqrt{2\pi\sigma_l^2}} exp\left(-\frac{(y_i - \mu_l)^2}{2\sigma_l^2}\right) \tag{5.11}$$

Using the assumption of conditional independence

$$\begin{aligned} P(y \mid x) &= \prod_{i \in S} P(y_i \mid x_i) \\ &= \prod_{i \in S} \left[\frac{1}{\sqrt{2\pi}} exp\left(-\frac{(y_i - \mu_{x_i})^2}{2\sigma_{x_i}^2} - log(\sigma_{x_i}) \right) \right] \end{aligned} \tag{5.12}$$

(5.12) can be expressed as

$$P(y \mid x) = \frac{1}{Z'} exp(-U(y \mid x))) \tag{5.13}$$

$$\begin{aligned} U(y \mid x) &= \sum_{i \in S} U(y_i \mid x_i) \\ &= \sum_{i \in S} \left[\frac{(y_i - \mu_{x_i})^2}{2\sigma_{x_i}^2} + log(\sigma_{x_i}) \right] \end{aligned}$$

and $Z' = (2\pi)^{N/2}$. Using the above, (5.10) can be expressed as

$$\hat{x} = arg \max_x \left[\frac{1}{Z} exp(-U(x)) \frac{1}{Z'} exp(-U(y \mid x)) \right] \tag{5.14}$$

(5.14) is equivalent to minimizing the following

$$\begin{aligned} \hat{x} &= arg \min_x [U(y \mid x) + U(x)] \\ &= arg \min_x \left[\sum_{i \in S} \{ \frac{(y_i - \mu_{x_i})^2}{2\sigma_{x_i}^2} + log(\sigma_{x_i}) + \sum_{c_i \in C} V_c(x, \phi) \} \right] \end{aligned} \tag{5.15}$$

The MAP estimate of $\hat{x}$ in (5.15) is obtained by employing the proposed Hybrid Tabu Search (HTS) algorithm.

5.4 Hybrid Tabu Search Procedure:

5.4.1 Implementation of Hybrid Tabu Search Algorithm

We have developed the hybrid algorithm exploring the notions of annealing and the finite memory concept of Tabu Search procedure. The notion of annealing is employed with a view to examine every point of the search space with finite probability and hence obtain global optimal solution. The next move of the Tabu Search

is achieved by using the notion of neighbourhood search. In our implementation strategy, we consider an image as a point in the multidimensional search space. The next move is another image in the neighbourhood that has energy less than all the Tabu moves. Hence, the revisiting of earlier points are avoided. The next image in the move is attained by perturbing the point in the neighbourhood structure and selecting another image which has less energy than all the earlier moves known as Tabu moves. Thus, an array of Tabu images are created. In order to overcome the local minima trapping, the aspiration condition is introduced. The aspiration condition here is to accept moves of high energy with a probability. This guides the algorithm to come out of local minima and to attain the optimal values. The cooling schedule is introduced to avoid the premature convergence of the algorithm.

5.4.2 Hybrid Tabu Search (HTS) Algorithm

1. Initialize the initial temperature T_{in}.

2. The Initial Image of the algorithm is the degraded image.

3. A Tabu list, i.e. Tabu image set is created to store the recent moves, i.e. the image estimates of the algorithm. The set is of fixed length.

4. From the current move of the image, the next Tabu image is generated.

   (i) Perturb $x_{ij}(t)$ with a zero mean Gaussian distribution with a suitable variance.

   (ii) Evaluate the energy $U_p(x_{ij}(t+1))$ and $U_p(x_{ij}(t))$. If $\Delta f = (U_p(x_{ij}(t+1)) - U_p(x_{ij}(t))) < 0$, assign the modified value as the new value. If $\Delta f > 0$, accept the $x_{ij}(t+1)$ with a probability (if $exp(-\Delta f/T(x)) > random(0,1)$).

   iii) Repeat step (ii) for all the pixels of the image.

5. Compute the energy of the updated image $x(t+1)$ as $P_{x(t+1)}$ and compare it

with the energy of the Tabu list named as Tabu energy, if $P_{x(t+1)} < P_{Tabu}$, accept $x(t+1)$ as Tabu image.

6. Aspiration condition: If $P_{x(t+1)} > P_{Tabu}$, accept $x(t+1)$ as Tabu image with a probability.

7. Update the Tabu list.

8. Decrease the Temperature according to the logarithmic cooling schedule.

9. Repeat step 4-8 till the stopping criterion is met. In our simulation the stopping criterion is: temperature decreases to a low value.

5.5 Iterated Conditional Mode (ICM) Algorithm

To obtain the optimal Bayesian estimate of the image, *a posteriori* probability given in (5.8) is to be maximized. Stochastic relaxation techniques yield an optimal solution at the cost of huge computational overhead [11]. Since it is difficult to maximize the joint probability of an MRF, the problem of segmenting an image using MRF model to obtain MAP estimates of the image is a horrendous task.

The Iterated Conditional Modes (ICM) algorithm of Besag [15] gave a simplification to this problem. ICM is a deterministic algorithm and, maximizes local conditional probabilities sequentially, which states that "*suppose $\hat{x}$ denotes a provisional estimate of the true scene x^* and that our aim is to update the current label $\hat{x}_i$ at pixel i given all available information. Then a plausible choice is the label which has maximum conditional probability, given records y and the current construction $\hat{x}_{S\setminus i}$ elsewhere*". Here $x_{S\setminus i}$ represents the label set for the whole image except the site i. This algorithm uses the "greedy" strategy in the iterative local maximization and is based upon two assumptions as follows.

- For a particular realization x, the random variables $Y_1, Y_2, ...Y_n$ are conditionally independent and each y_i has the same known conditional density function $p(y_i \mid x_i)$, dependent on x_i.

$$p(y \mid x) = \prod_{i=1}^{S} p(y_i \mid x_i) \tag{5.16}$$

  where S is the number of sites of an image.

- The true image is a realization of a locally dependent MRF with respect to $\{P(x)\}$ which is the Markovianity property of MRF.

One starts with an initial labeling, $\hat{x^0}$ and then iterates sequentially (or in parallel) through each pixel, replacing the current label at that pixel with the label that maximizes $P(x_i \mid y, x_{S\setminus i})$. This defines a single cycle of an iterative algorithm for estimation of x^*. The probability distribution of x for the given y can be expressed as

$$P(x \mid y) = P(x_i \mid y,\ x_{S\setminus i})P(x_{S\setminus i} \mid y). \tag{5.17}$$

Using the two assumptions and the Bayes theorem, it follows that

$$\begin{aligned} P(x_i \mid y,\ x_{S\setminus i}) &= P(x_i \mid y,\ x_{\eta_i}) \\ &= \frac{P(y,\ x_i \mid x_{\eta_i})}{P(y \mid x_{\eta_i})} \end{aligned} \tag{5.18}$$

Finally the expression in (5.18) reduces to

$$P(x_i \mid y,\ x_{S\setminus i}) = P(y \mid x_i,\ x_{\eta_i})P(x_i \mid x_{\eta_i}) \tag{5.19}$$

Thus,

$$P(x_i \mid y,\ x_{S\setminus i}) \ \ \alpha \ \ p(y_i \mid x_i)P(x_i \mid x_{\eta_i}) \tag{5.20}$$

$P(x_i \mid y,\ x_{S\setminus i})$ is much easier to maximize than $P(x \mid y)$, which is the notion of ICM. Maximizing (5.20) is equivalent to minimizing the corresponding posterior potential.

Hence MAP estimates of the image labels are obtained using ICM algorithm by maximizing (5.20) as follows.

$$\hat{x_i} = arg\max_{x_i} p(x_i \mid y_i,\ \hat{x}_{S\setminus i})$$

or equivalently $\hat{x_i} = arg\max_{x_i} p(x_i \mid y,\ \hat{x}_{\eta_i})$

or equivalently $\hat{x_i} = arg\min_{x_i} U(x_i \mid y_i,\ \hat{x}_{\eta_i})$

The posterior energy at each site can be expressed as

$$U(x_i \mid y_i,\ \hat{x}_{\eta_i}) = \sum_{j\in\eta_i} U(x_i \mid y_i,\ \hat{x}_j) + U(x_i \mid y_i) \tag{5.21}$$

This algorithm is applied for a fixed number of cycles until convergence for final estimate is obtained. Since all updates must inherently either increase or maintain the joint probability of current realisation, the algorithm must converge to a local optimum. However, there is no guarantee of convergence to the global mode. Its dependence only on the local characteristics of $p(x)$ is ensured by the rapid convergence.

Salient steps of ICM Algorithm

1. Initialize the labeling $\hat{x^0}$ of the given image.
2. From the current move of the image, the next image is generated.
   (a) Evaluate the energy at each site.
   (b) Perturb each site with a suitable Gaussian disturbance.
   (c) Evaluate the new energy at that site after the disturbance.
   (d) If the new energy is less than the previous one, then except the perturbed one as the new label, else the previous one remains.

3. Repeat steps of 2 for all sites of the image to obtain the new configuration.

4. Go to step 2 and repeat till convergence is achieved.

5.6 Simulated Annealing (SA) Algorithm

Simulated Annealing algorithm has been proposed by Kirkpatrick [31, 32]. Geman and Geman [11] introduced SA to a more sophisticated optimization problem of image segmentation. SA draws heavily upon ideas from statistical mechanics and is introduced into combinatorial optimization [31, 32]. It has been considered to be a methodology with the potential to overcome the local convergence problem. First a cooling schedule is designated for the Gibbs distribution temperature parameter. The temperature begins in a hot state, causing the energy surface to be relatively flat, since the system is relatively excited. The temperature is then steadily lowered, making the local and global minima further pronounced. As the temperature tends to zero, the surface moves towards a set of inverted peaks, the deepest at the global minimum. If T is decreased too fast, the system is locked into a local minimum energy state and the global minimum energy state is never reached. There are three ingredients which constitute SA.

1. There should be a suitable cost function to maximize or minimize.

2. The second ingredient is the updating mechanism which consists of a visitation scheme and the actual updating, which is done by Metropolis algorithm or Gibbs sampler.

3. Third component of SA is to have an appropriate annealing schedule. The rate at which temperature T can be decreased is called the "annealing schedule" or "cooling schedule". T at n^{th} iteration is taken as $T(n) = \frac{\Delta E}{\log(1+n)}$, where ΔE is the energy difference between the highest and the lowest energy potential.

SA distinguishes between different local optima. Starting from an initial point, the algorithm takes the steps and the objective function is evaluated. When minimizing a function, any downhill step is accepted and the process repeats from this new point. The uphill decision is made by the Metropolis criteria. Thus, it can escape from local minima. When the optimization process proceeds, the length of the steps decline and the algorithm closes in on the global optimum. Since the algorithm makes very few assumptions regarding the function to be optimized, it is quite robust.

Salient steps of SA algorithm

1. Initialize the temperature T_{in}.
2. Compute the energy E of the initial configuration.
3. Perturb the system slightly with suitable Gaussian disturbance.
4. Compute the new energy E' of the perturbed system and evaluate the change in energy $\Delta E = E' - E$.
5. If $(\Delta E < 0)$, accept the perturbed system as the new configuration.
6. If $(\Delta E > 0)$, accept the perturbed system as the new configuration with a probability $exp\frac{-\Delta E}{kT}$.
7. Decrease the Temperature according to the logarithmic cooling schedule.
8. Repeat step 3-7 till the temperature decreases to sufficiently low value.

Hence, final configuration with the minimum energy can be obtained.

5.7 Results and Discussions

In simulation, both synthetic as well as real images are considered to validate the proposed algorithm. GHMRF model based synthetic images consisting of 3,4, and

5 classes are generated using Gibb's sampler. Besides, four different brain MR images are considered. The degraded images are obtained by adding white Gaussian noise of varying strength to the original image. The following degradation model is considered in simulation. $Y = X + N$ where Y is the random field associated with observed degraded image, X is the random field associated with the label process and N is the zero mean white Gaussian noise. The observed degraded image is modeled as GHMRF model where as the class labels are modeled as MRF model. The clique potential function $V_c(x, \phi)$ of the MRF model corresponding to the a priori class is given by

$$\begin{aligned} V_c(x) &= -\delta \quad if \quad |x_i - x_j| = 0 \\ &= \delta \quad if \quad |x_i - x_j| \neq 0 \end{aligned} \tag{5.22}$$

where x_i and x_j are the i^{th} and j^{th} pixel values respectively. Here the GHMRF model parameters for μ and σ for each class and the *a priori* MRF model parameter δ are selected on an ad hoc basis. We define $SNR_{dB} = 10\log_{10}(\frac{1}{N^2}\sum_i \frac{x_i^2}{\sigma^2})$.

5.7.1 Synthetic Images:

Synthetic image of 3 class, generated by Gibb's sampler, is shown in Fig. 5.1(a). The corresponding noisy versions of SNRs 22, 20 and 18dB are shown in Figs. 5.1(b), (f) and (j) respectively. The noisy images are modeled as GHMRF model and associated model parameters μ and σ considered for three different classes are tabulated in Table 5.1. It is to be noted that these are selected on a trial and error basis. The a priori MRF model parameter δ is selected as unity. The segmented images obtained by our proposed hybrid Tabu Search (HTS) algorithm are shown in Figs. 5.1(c), (g) and (k). The parameters of the HTS algorithm used in our simulation are: initial temperature $T_{in} = 0.5$ and length of the Tabu array K=10. The cooling schedule is governed by logarithmic function. It is observed from Figs.

5.1(c) and (g) that the proper labeling of pixels could be obtained for noisy images of SNR 22 and 20dB. It is also observed from Fig. 5.1(k) that there are very few misclassified pixels in a given class. Fig. 5.1(k) correspond to a noisy image of SNR 18dB and thus, it is clear that the performance of the HTS algorithm wane with increase in noise strength. The performance of the proposed HTS algorithm is also compared with SA algorithm and ICM algorithm. The results obtained by SA algorithm are shown in Figs. 5.1(d), (h), (l) while Figs. 5.1(e), (i), (m) show the results obtained by ICM algorithm. It is observed from Figs. 5.1(d), (h) and (l) that the results obtained by SA are comparable to that of the HTS algorithm, but the HTS algorithm converges faster than that of SA algorithm. This phenomenon is clear from Fig. 5.4(a) which shows the convergence corresponding to the minimization of the posterior energy $U_p(x)$ given by equation (5.15). It is seen from Fig. 5.4(a) that the proposed algorithm converges at approximately around 15 iterations where as the SA algorithm converge approximately 30 iterations. This enhancement in the rate of convergence may be attributed to the notion of Tabu Search in our algorithm that avoids the revisiting of different moves in the search space. The results obtained by ICM are poor as compared to SA and HTS algorithm. Comparing Figs. 5.1(i), (h) and (g) it can be inferred that results obtained by SA and the HTS algorithm are better that of ICM. Similar observations are also made in case of high noise condition of SNR 18dB. This can be seen from Fig. 5.1(m). The phenomenon of degradation in performance with increase in noise strength is also observed in case of ICM and SA algorithm as well. Since ICM is a locally convergent algorithm, poor performance as compared to other one is expected.

The synthetic image consisting of four classes is shown in Fig. 5.2(a). Noisy images of SNR 22, 20 and 18dB are shown in Figs. 5.2(b), (f) and (j) respectively. Figs. 5.2(c), (g) and (k) show the segmented images obtained by the HTS algorithm. Since, this image consists of four classes, the GHMRF model parameters correspond-

ing to four classes are presented in Table 5.2. The a priori MRF model parameters δ selected for different noisy cases are also given in Table 5.2. The parameters of the Hybrid Tabu algorithm are same as that used for three class image. It is observed from Figs. 5.2(c), (g) and (k) that the algorithm yielded proper segmented images at low noise condition of 22dB. With increase in noise to 20dB the segmented image contains few misclassified pixels despite four prominent classes as shown in Fig. 5.2(g). Further increase in noise degrades the performance of the algorithm as seen from Fig. 5.2(k). The results shown in Fig. 5.2(k) has four distinct classes even under high noise condition of 18dB as shown in Fig. 5.2(g). The results obtained by SA algorithm are shown in Figs. 5.2(d), (h) and (l). These are comparable to that of the HTS algorithm but the proposed algorithm converges faster than that of SA algorithm. This effect is evident from Fig. 5.4(b) that shows the behaviour of the posterior energy with respect to each epoch of the algorithm. It is clearly observed from Fig. 5.4(b) that the HTS algorithm converges at around 7 iterations where as the SA algorithm converges after 15 iterations. The rate of convergence of the proposed algorithm is also faster than that of SA. This phenomenon is also clearly evident from Fig. 5.4(b). Out of the three results obtained by SA algorithm, it can be inferred that the performance of SA algorithm wane with the increase in noise strength. Figs. 5.2(e), (i) and (m) show the results obtained by ICM algorithm. It is seen from Fig. 5.2(i) that there are many misclassified pixels albeit four distinct visible classes. With increase in noise i.e. at 18dB SNR, there is further degradation in the performance of the algorithm as seen from Fig. 5.2(m). This poor performance of ICM as compared to SA and the proposed algorithm could be attributed to the local convergent property of the ICM algorithm.

Five class synthetic image considered in our simulation is shown in Fig. 5.3(a). The corresponding noisy versions are shown in Figs. 5.3(b), (f) and (j) and, Figs. 5.3(c), (g) and (k) show the results obtained by HTS algorithm and the model

parameters used for these five classes are tabulated in Table 5.3. The *a priori* model parameters δ for each of the noisy images are also given in Fig. 5.3. The performance of the HTS algorithm are same as that of case of 3 and 4 class images. It is observed that at low noise, the algorithm could segment properly where as the performance degraded gradually with the increase in noise strength i.e at 18dB. Similar phenomenon is also observed in case of SA algorithm. The results obtained using SA algorithm are shown in Figs. 5.3(d), (h) and (l). Fig. 5.3(l) show a result corresponding to SNR of 18dB and it is observed that few misclassified pixels are found in the segmented image. Even though the results obtained by SA are comparable with that of the proposed algorithm, the rate of convergence of the proposed algorithm is much faster than the SA algorithm as seen from Fig. 5.4(c). As seen from Fig. 5.4 (c), the proposed algorithm converges at around 10 iterations while SA algorithm converges after 100 iterations. The results obtained by ICM algorithm are shown in Figs. 5.3(e), (i) and (m). It is observed that even at low noise condition of 22dB SNR, there is quite a few misclassified pixels as seen from Figs. 5.3(e). The findings in this case is same as that of 3 and 4 class image case. This degradation in performance of ICM as compared to SA and the proposed one could be attributed to the local convergent property of the ICM algorithm.

5.7.2 Brain MR Images:

Four different brain MR images as shown in Figs. 5.5(a), 5.6(a), 5.7(a), 5.9(a) are considered to validate the algorithm. A brain MR image of size (189×205) is shown in the Fig. 5.5(a). The corresponding noisy images of SNR 25dB, 22dB, 20dB and 18dB are shown in the Figs. 5.5(b), (f), (j) and (n) respectively. Four *a priori* classes are assumed for this real image and the corresponding GHMRF model parameters for four different classes are tabulated in Table 5.4. The *a priori* MRF model parameters for all the noisy cases is 0.1. The parameters used in HTS algorithm are: T_{in}=0.1

and length of the Tabu array K=5. It is observed from from Figs. 5.5(c), (g), (k) and (o) that four distinct classes could be obtained up to SNR 20dB while at high noise condition of SNR 18dB there are visibly four classes with a few mislabeled pixels. Hence, the performance of the algorithm gradually deteriorates with increase in noise strength. Similar observations are also made in case of SA algorithm. The results obtained by SA algorithm are shown in Figs. 5.5(d), (h), (l) and (p). Although the results are visibly comparable to those obtained by the proposed algorithm, the proposed algorithm converges faster than that of SA algorithm. This is evident from Fig. 5.8(a) that HTS algorithm converges around 100 iterations while SA converges around 150 iterations. The rate of convergence of HTS is also found to be faster than that of SA. Results obtained by ICM algorithm deteriorates even at SNR 22dB as seen from Fig.5.5(i) and at SNR 18dB, there is severe degradation as seen from Fig. 5.5(q). This phenomenon can be attributed to the local convergent property of algorithm.

A second brain image of size (227×195), as shown in Fig. 5.6(a), is considered in our simulation. The corresponding noisy images of SNR 25dB, 22dB, 20dB and 18dB are shown in Figs. 5.6(b), (f), (j) and (n) respectively. Here four *a priori* classes are assumed and the associated GHMRF model parameters are given in Table 5.5. The *a priori* MRF model parameter for all the noisy cases is selected as 0.1. The results obtained by the proposed HTS algorithm are shown in Figs. 5.6(c), (g), (k) and (o). In all the noisy cases four distinct classes could be obtained but for a few mislabeling of pixels corresponding to SNR of 18dB. Thus the performance of the algorithm starts deteriorating from noisy case of SNR 20dB. Analogous observations are also made in case of the results obtained by SA algorithm as shown in Figs. 5.6(d), (h), (l) and (p). However, as seen from Fig. 5.8(b) the rate of convergence of HTS algorithm is a bit faster than that of SA algorithm. The results obtained by the proposed approach is quite comparable to that of SA algorithm. It is observed

from the results shown in Figs. 5.6(e), (i), (m) and (q) that even at low noise conditions there are visible mislabeling of pixels in case of ICM algorithm. This problem aggravated further with increase in noise strength as seen from Figs. 5.6(i), (m) and (q). This mislabeling is expected because ICM algorithm is sensitive to the choice of initial parameters.

The third brain MR image considered is shown in Fig. 5.7(a) and its noisy versions in Figs. 5.7(b), (f), (j) and (n). Figs. 5.7(c), (g), (k) and (o) show the results obtained by HTS algorithm and again four distinct classes could be obtained as assumed for the noise free image. The model parameters used are given in Table 5.6. The algorithm exhibited similar behaviour as in case of the previous two brain MR images. The parameters used in HTS are $T_{in} = 0.1$ and the length of the Tabu array K=5. The results obtained by SA algorithm are shown in Figs. 5.7(d), (h), (l) and (p) and once again the algorithms performance degrades with increase in noise strength. Even though the results obtained by HTS and SA algorithms are comparable, the rate of convergence of HTS is faster than that of SA as seen from Fig. 5.8(c). ICM algorithm as in the previous case exhibited poor performance as compared to HTS and SA algorithm. This effect is evident from Figs. 5.7(e), (i), (m) and (q).

The fourth brain MR image considered is shown in Fig. 5.9(a) and the corresponding noisy images are shown in Figs. 5.9(b) and (f) respectively. In this case also four classes are assumed and the corresponding model parameters are tabulated in Table 5.7. The performance of HTS and SA are same as the previous cases.The parameters used in HTS algorithm are $T_{in} = 0.5$ and Tabu length array K=10. The rate of convergence of HTS is faster than SA and hence HTS algorithm converged around 5 iterations while SA after 15 iterations. As expected, performance of ICM algorithm is poor as compared to SA algorithm. This effect is observed in Figs. 5.9(e) and (i).

5.8 Conclusions

This chapter addressed the segmentation problem in supervised framework. The GHMRF model parameters together with *a priori* class model parameter δ are selected on a trial and error. The proposed HTS algorithm yielded satisfactory results in case of synthetic as well as real images. The parameters of HTS algorithm are also selected on trial and error basis. The performance of the proposed algorithm is compared with that of SA algorithm. Even though the results obtained by HTS algorithm and SA algorithm are visibly comparable, the proposed algorithm converged faster than that of the SA algorithm in all the synthetic as well as brain MR image examples. This phenomenon could be attributed to the algorithm's feature to alleviate the problem of revisiting the candidate solutions in the search space. In order to show the superiority of the algorithm over the locally convergent algorithms, the results are compared with that of ICM algorithm of Besag [15]. As expected, it is observed that performance of the ICM algorithm is poor as compared to the HTS and SA algorithms.

class→		1	2	3
SNR=22dB	σ	0.104	0.103	0.98
$\delta = 1.0$	μ	0.027	0.991	1.995
SNR=20dB	σ	0.104	0.109	0.98
$\delta = 1.0$	μ	0.027	0.991	1.995
SNR=18dB	σ	0.102	0.109	0.98
$\delta = 1.0$	μ	0.034	0.992	1.996

Table 5.1: *Model parameters of* 3*-class synthetic image of size* (128×128) *with SNR* $22dB$*,* $20dB$ *and* $18dB$ *of HTS algorithm.*

class→		1	2	3	4
SNR=22dB	σ	0.141	0.219	0.197	0.196
$\delta = 1.0$	μ	0.226	0.988	2.0	2.987
SNR=20dB	σ	0.147	0.195	0.197	0.196
$\delta = 1.0$	μ	0.226	0.988	2.0	2.987
SNR=18dB	σ	0.173	0.285	0.284	0.284
$\delta = 0.75$	μ	0.028	0.98	2.0	2.98

Table 5.2: *Model parameters of* 4*-class synthetic image of size* (64×64) *with SNR* $22dB$*,* $20dB$ *and* $18dB$ *of HTS algorithm.*

class→		1	2	3	4	5
SNR=22dB	σ	0.207	0.247	0.255	0.246	0.248
$\delta = 1.0$	μ	0.043	0.99	1.99	2.992	3.998
SNR=20dB	σ	0.207	0.247	0.255	0.246	0.248
$\delta = 1.0$	μ	0.043	0.99	1.99	2.992	3.998
SNR=18dB	σ	0.306	0.307	0.312	0.302	0.304
$\delta = 0.8$	μ	0.031	0.983	1.989	2.991	3.985

Table 5.3: *Model parameters of* 5*-Class synthetic image of size* (128×128) *with SNR* $22dB$*,* $20dB$ *and* $18dB$ *of HTS algorithm.*

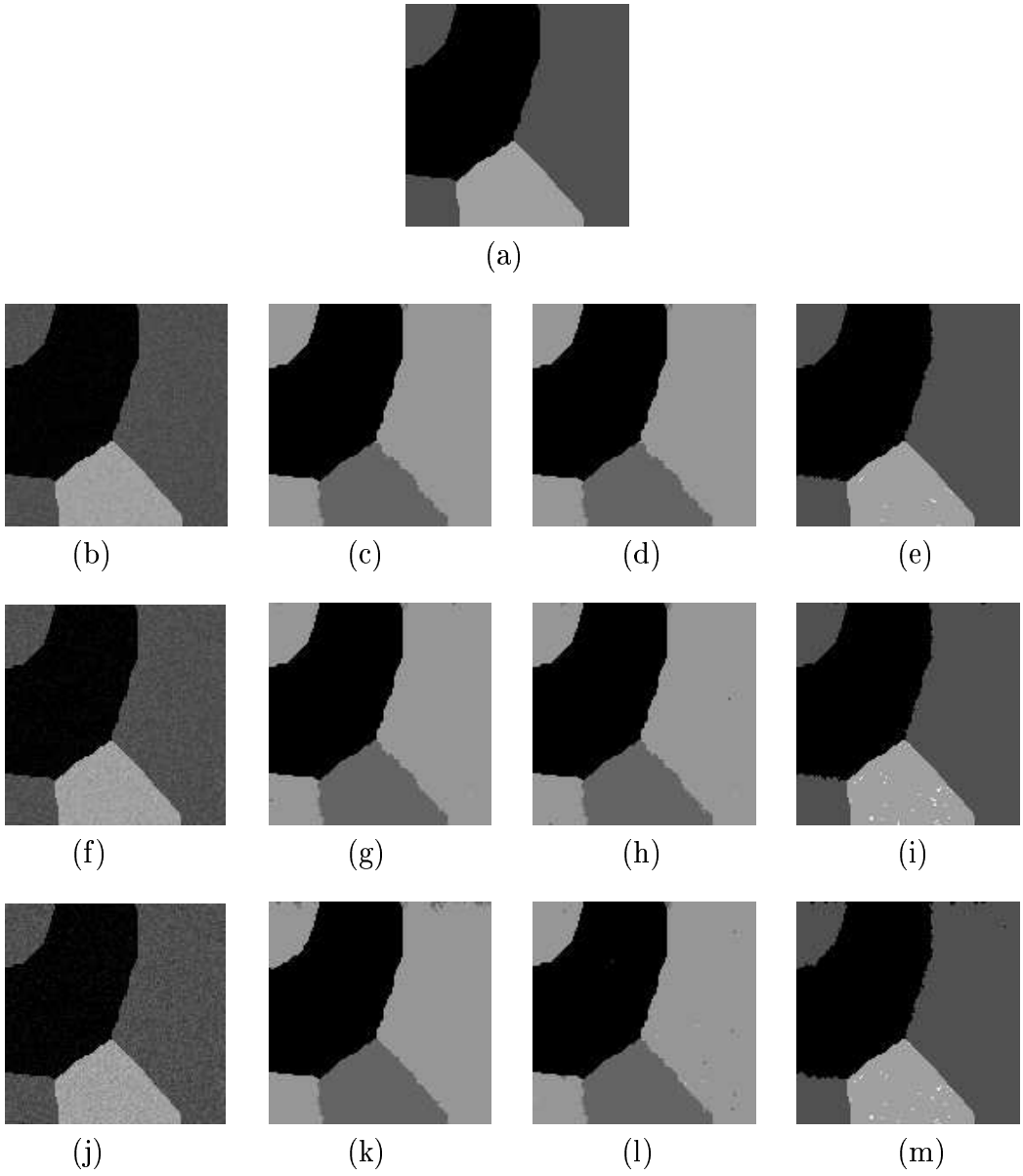

Figure 5.1: *Supervised segmentation of* 3*-class synthetic image of size* (128×128) *: (a) original image; (b),(f) and (j): noisy images with SNR* $22dB$*,* $20dB$ *and* $18dB$ *respectively; (c), (g) and (k): corresponding segmented images using HTS Algo. respectively; (d), (h) and (l): corresponding segmented images using SA Algo. respectively; (e), (i) and (m): corresponding segmented images using ICM Algo. respectively.*

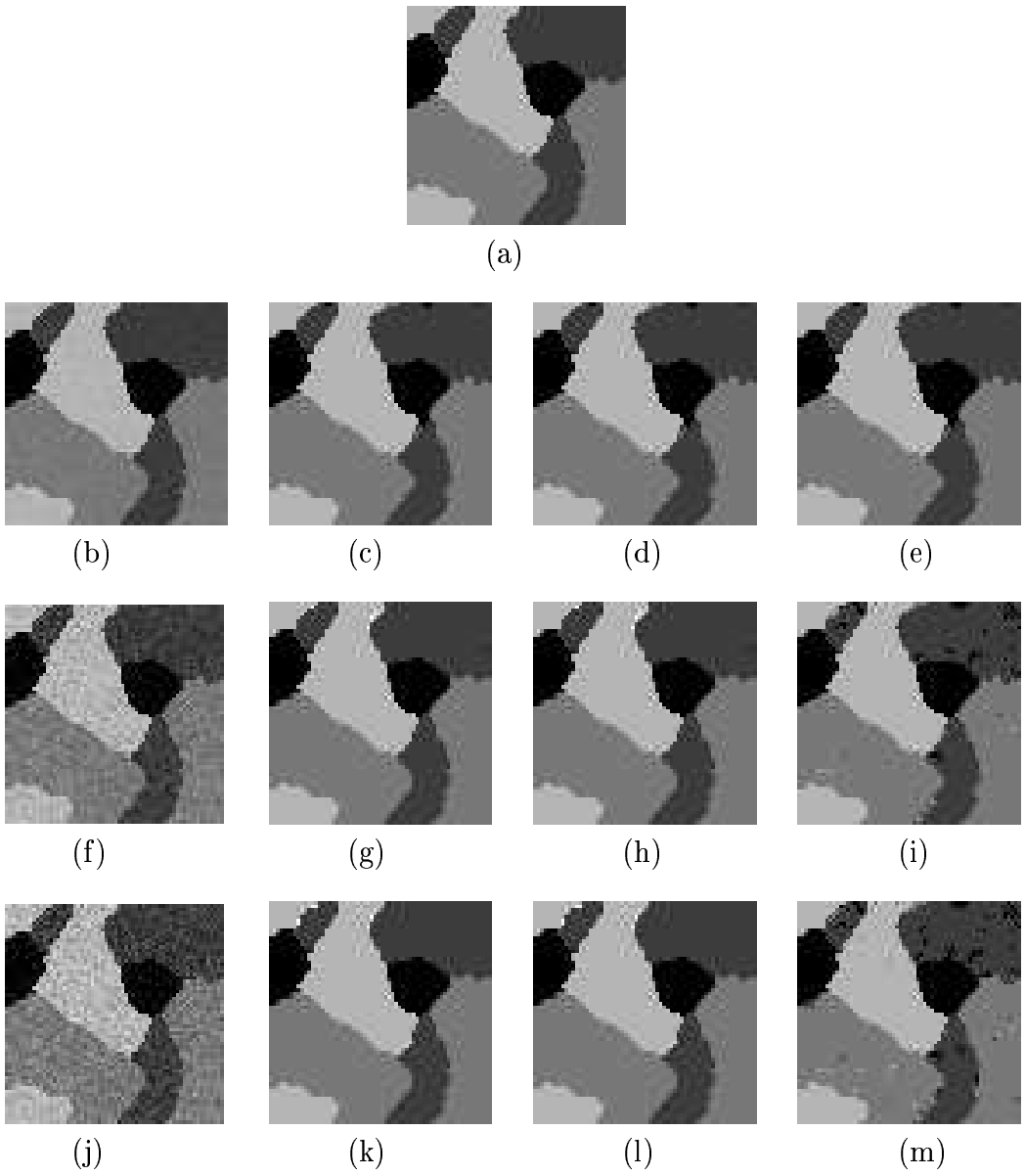

Figure 5.2: *Supervised segmentation of* 4*-class synthetic image of size* (64×64) *: (a) original image; (b), (f) and (j): noisy images with SNR* $22dB$*,* $20dB$ *and* $18dB$ *respectively; (c), (g) and (k): corresponding segmented images using HTS Algo. respectively; (d), (h) and (l): corresponding segmented images using SA Algo. respectively; (e), (i) and (m): corresponding segmented images using ICM Algo. respectively.*

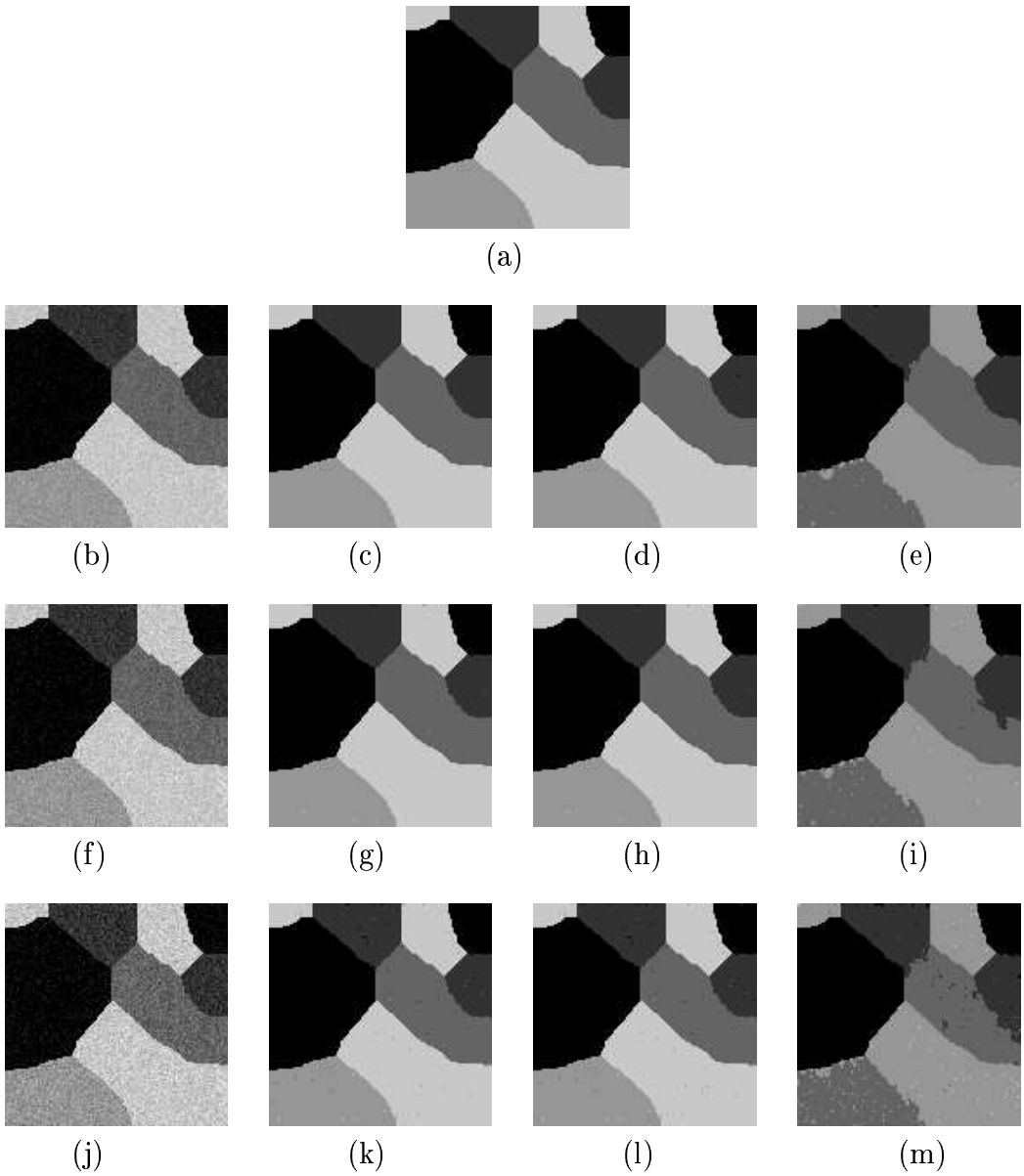

Figure 5.3: *Supervised segmentation of* 5*-class synthetic image of size* (128×128) *: (a)original image; (b), (f) and (j): noisy images with SNR* $22dB$*,* $20dB$ *and* $18dB$ *respectively; (c), (g) and (k): corresponding segmented images using HTS Algo. respectively; (d), (h) and (l): corresponding segmented images using SA Algo. respectively; (e), (i) and (m): corresponding segmented images using ICM Algo. respectively.*

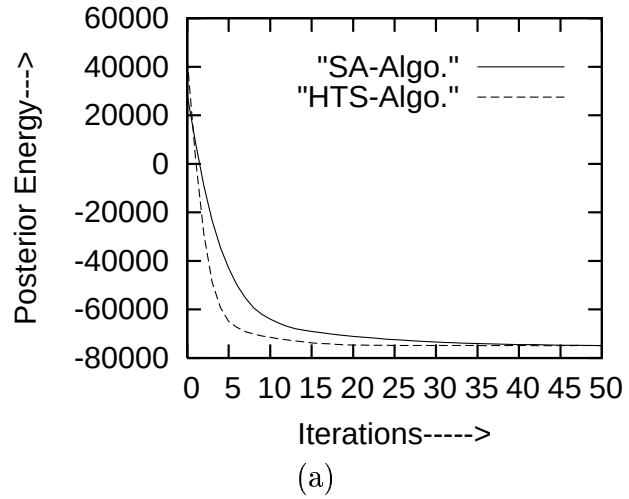

Figure 5.4: *Posterior Energy plots of synthetic Images for SNR 20dB using SA algorithm and HTS algorithm ; (a) 3-class, (b) 4-class, (c) 5-class.*

class→		1	2	3	4
SNR=25dB	σ	0.501	0.498	0.502	1.498
$\delta = 0.1$	μ	0.102	0.51	1.505	1.503
SNR=22dB	σ	0.501	0.512	0.508	1.502
$\delta = 0.1$	μ	0.105	0.507	1.504	1.511
SNR=20dB	σ	0.51	0.518	0.513	1.51
$\delta = 0.1$	μ	0.11	0.52	1.513	1.512
SNR=18dB	σ	0.515	0.519	0.517	1.515
$\delta = 0.1$	μ	0.12	0.521	1.52	1.523

Table 5.4: *Model parameters of brain MR image of size* (189×205) *with SNR* $25dB$, $22dB$, $20dB$ *and* $18dB$ *of HTS algorithm corresponding to Figure 5.5.*

class→		1	2	3	4
SNR=25dB	σ	0.41	0.57	0.55	0.6
$\delta = 0.1$	μ	0.1	0.96	2.13	2.8
SNR=22dB	σ	0.41	0.51	0.1	0.6
$\delta = 0.1$	μ	0.10	1.5	2.04	2.53
SNR=20dB	σ	0.415	0.512	0.15	0.61
$\delta = 0.1$	μ	0.11	1.51	2.06	2.55
SNR=18dB	σ	0.417	0.512	0.156	0.612
$\delta = 0.1$	μ	0.113	1.523	2.045	2.532

Table 5.5: *Model parameters of brain MR image of size* (227×195) *with SNR* $25dB$, $22dB$, $20dB$ *and* $18dB$ *of HTS algorithm corresponding to Figure 5.6.*

class→		1	2	3	4
SNR=25dB	σ	0.401	0.70	0.605	0.699
$\delta = 0.3$	μ	0.39	1.02	1.89	2.01
SNR=22dB	σ	0.401	0.75	0.6	0.71
$\delta = 0.3$	μ	0.41	1.03	1.91	2.11
SNR=20dB	σ	0.401	0.751	0.61	0.722
$\delta = 0.3$	μ	0.412	1.05	1.913	2.125
SNR=18dB	σ	0.402	0.752	0.617	0.725
$\delta = 0.3$	μ	0.415	1.07	1.92	2.132

Table 5.6: *Model parameters of brain MR image of size* (189×217) *with SNR* $25dB$, $22dB$, $20dB$ *and* $18dB$ *of HTS algorithm corresponding to Figure 5.7.*

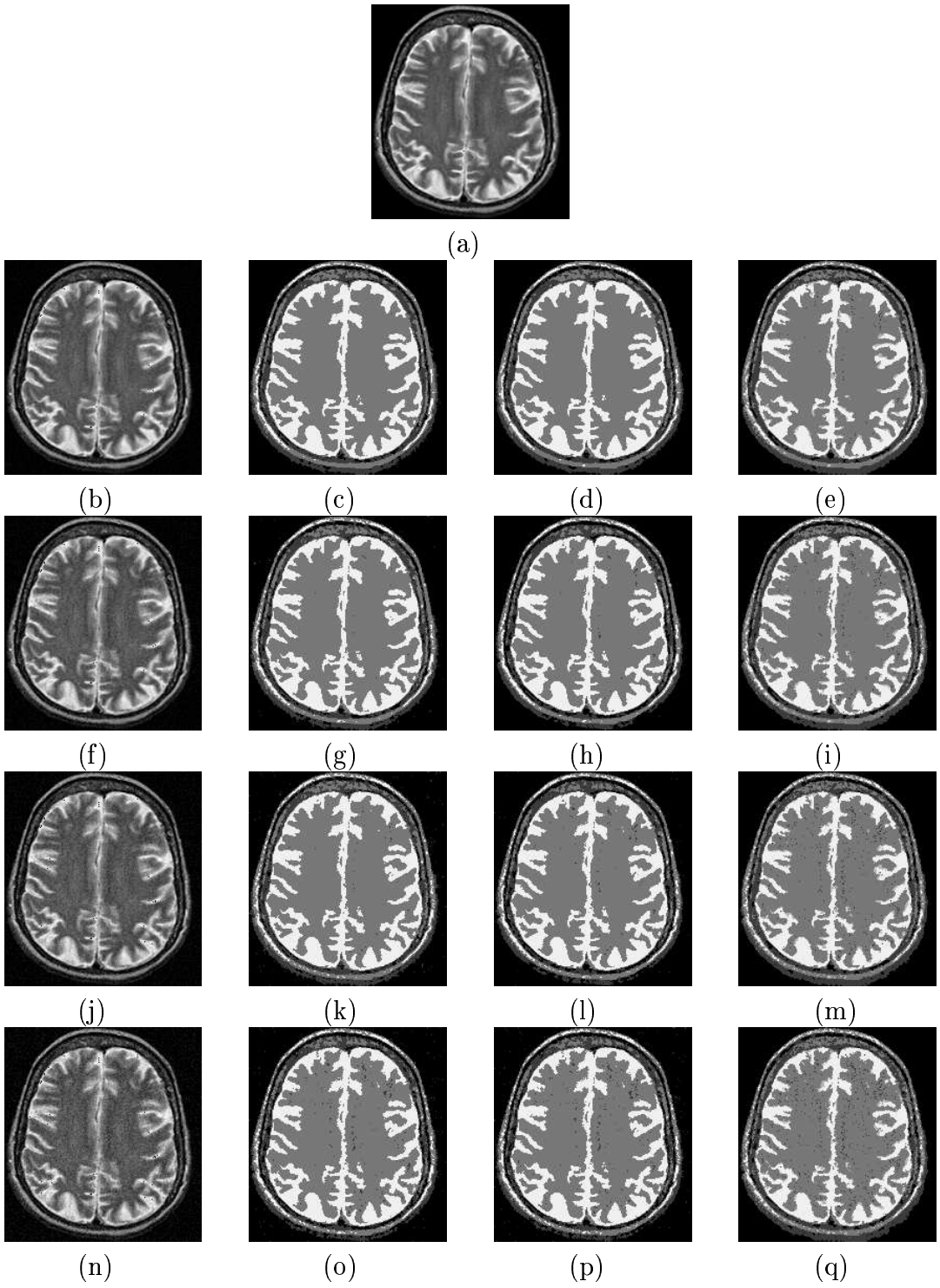

Figure 5.5: *Supervised image segmentation of brain MR image of size* (189×205)*: (a) original image; (b),(f),(j) and (n): noisy images with SNR* $25dB$*,* $22dB$*,* $20dB$ *and* $18dB$ *respectively; (c),(g),(k) and (o): corresponding segmented images using HTS Algo. respectively; (d),(h),(l) and (p): corresponding segmented images using SA Algo. respectively; (e),(i),(m) and (q): corresponding segmented images using ICM Algo. respectively*

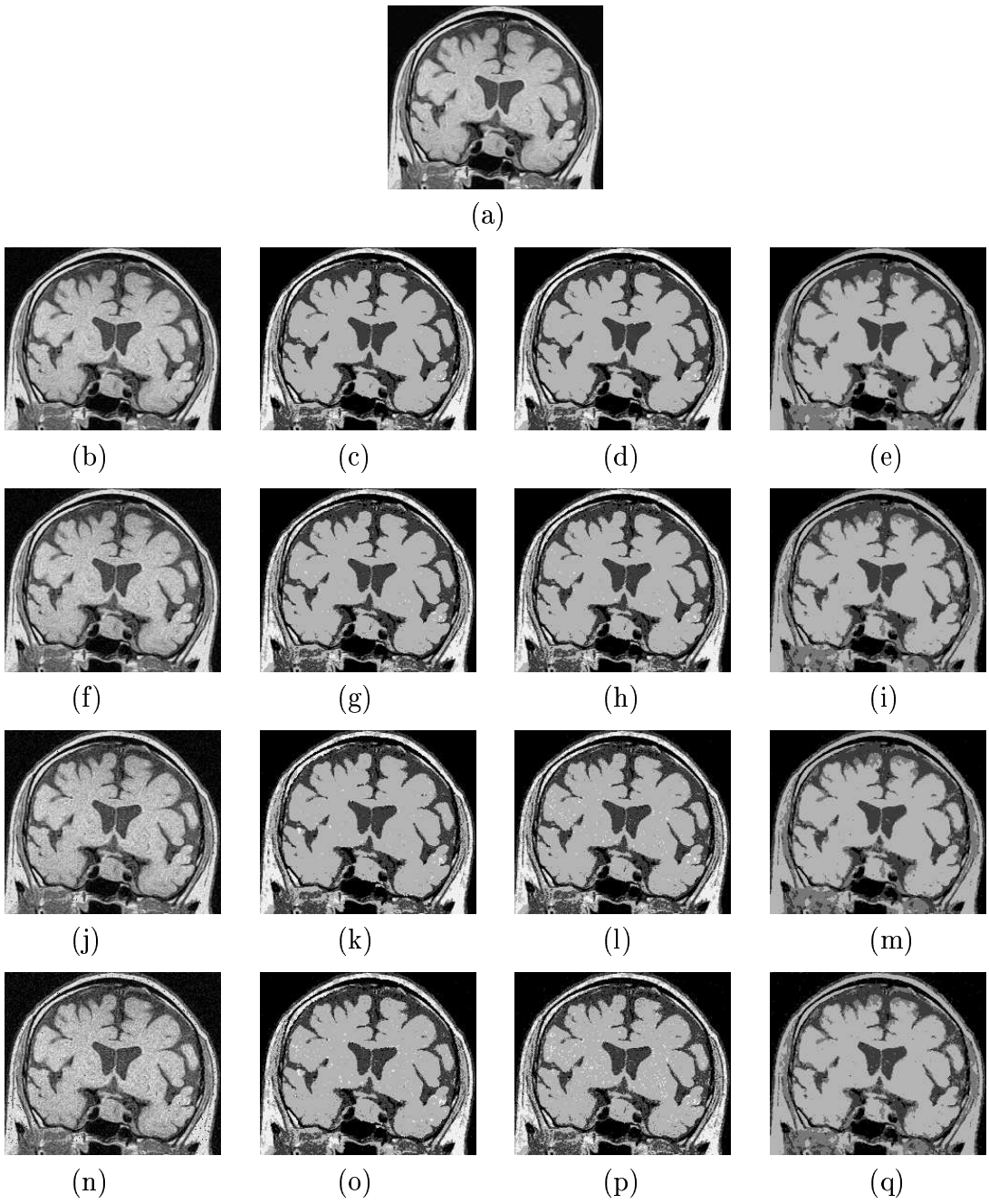

Figure 5.6: *Supervised image segmentation of brain MR image of size* (227×195) *: (a) original image; (b),(f),(j) and (n): noisy images with SNR* $25dB$*,* $22dB$*,* $20dB$ *and* $18dB$ *respectively; (c),(g),(k) and (o): corresponding segmented images using HTS Algo. respectively; (d),(h),(l) and (p): corresponding segmented images using SA Algo. respectively; (e),(i),(m) and (q): corresponding segmented images using ICM Algo. respectively*

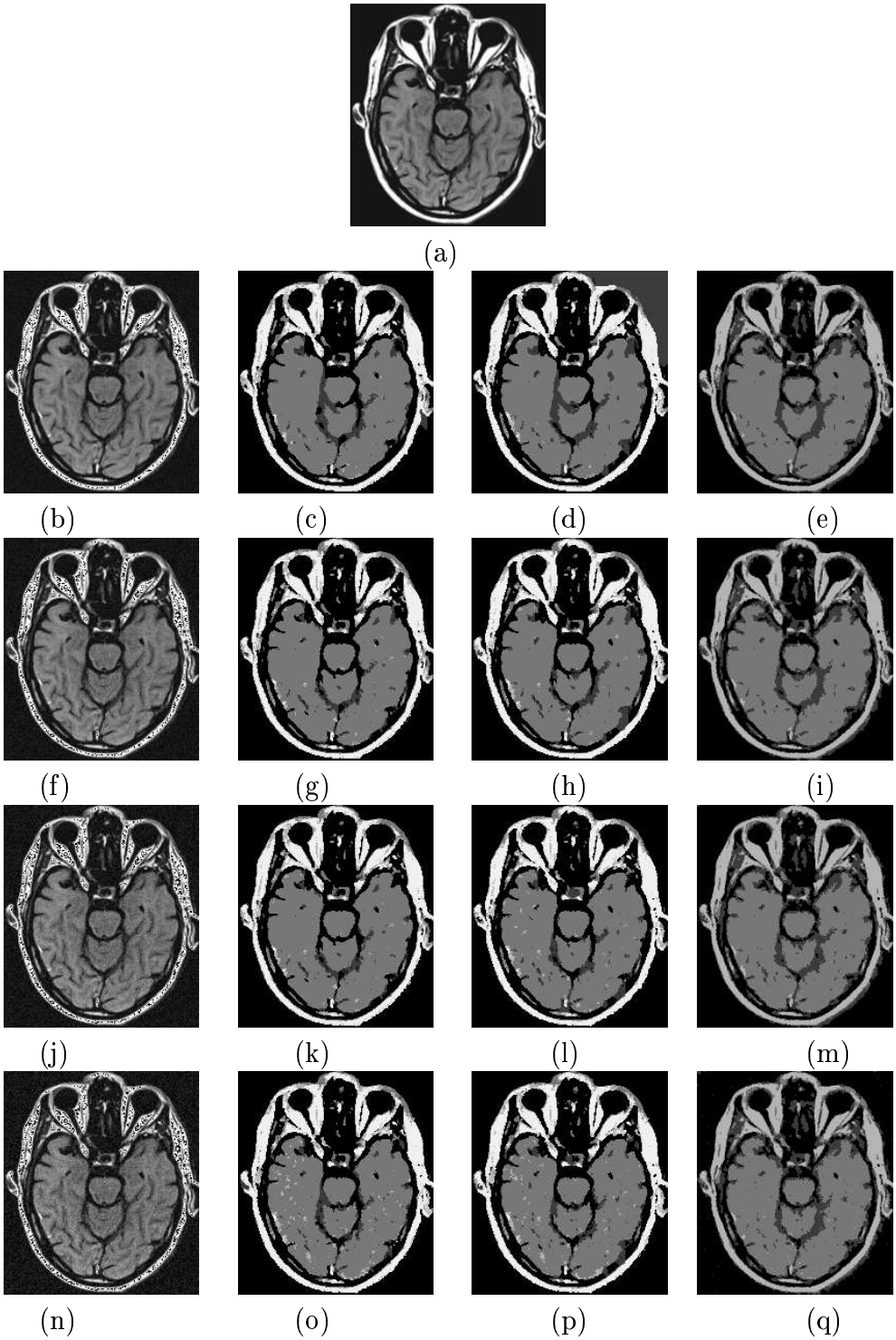

Figure 5.7: *Supervised image segmentation of brain MR Image of size* (189×217) *: (a) original image; (b),(f),(j) and (n): noisy images with SNR* $25dB$*,* $22dB$*,* $20dB$ *and* $18dB$ *respectively; (c),(g),(k) and (o): corresponding segmented images using HTS Algo. respectively; (d),(h),(l) and (p): corresponding segmented images using SA Algo. respectively; (e),(i),(m) and (q): corresponding segmented images using ICM Algo. respectively*

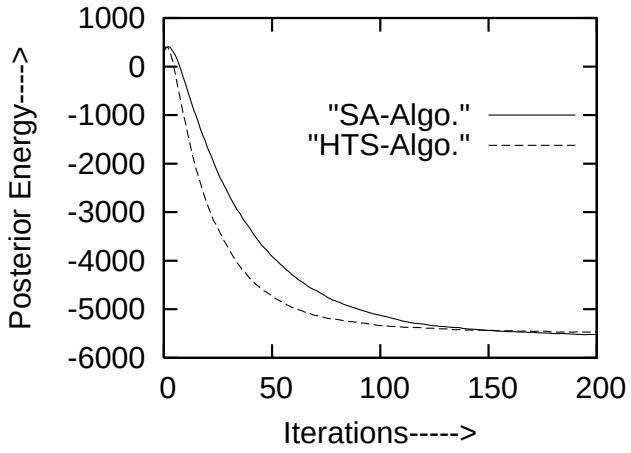

(a)

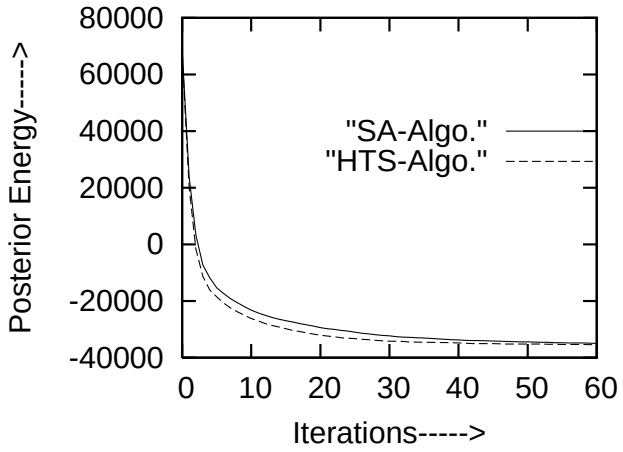

(b)

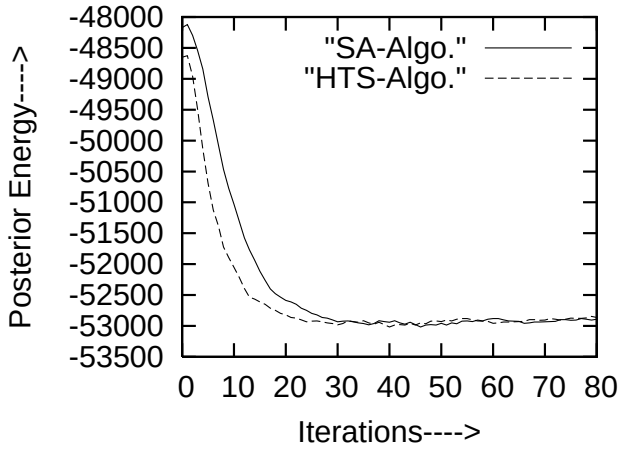

(c)

Figure 5.8: *Posterior Energy plots of brain MR Images for SNR 22dB using SA algorith and HTS algorithm; (a) of size (*189×205*), (b) of size (*227×195*), (c) of size (*189×217*).*

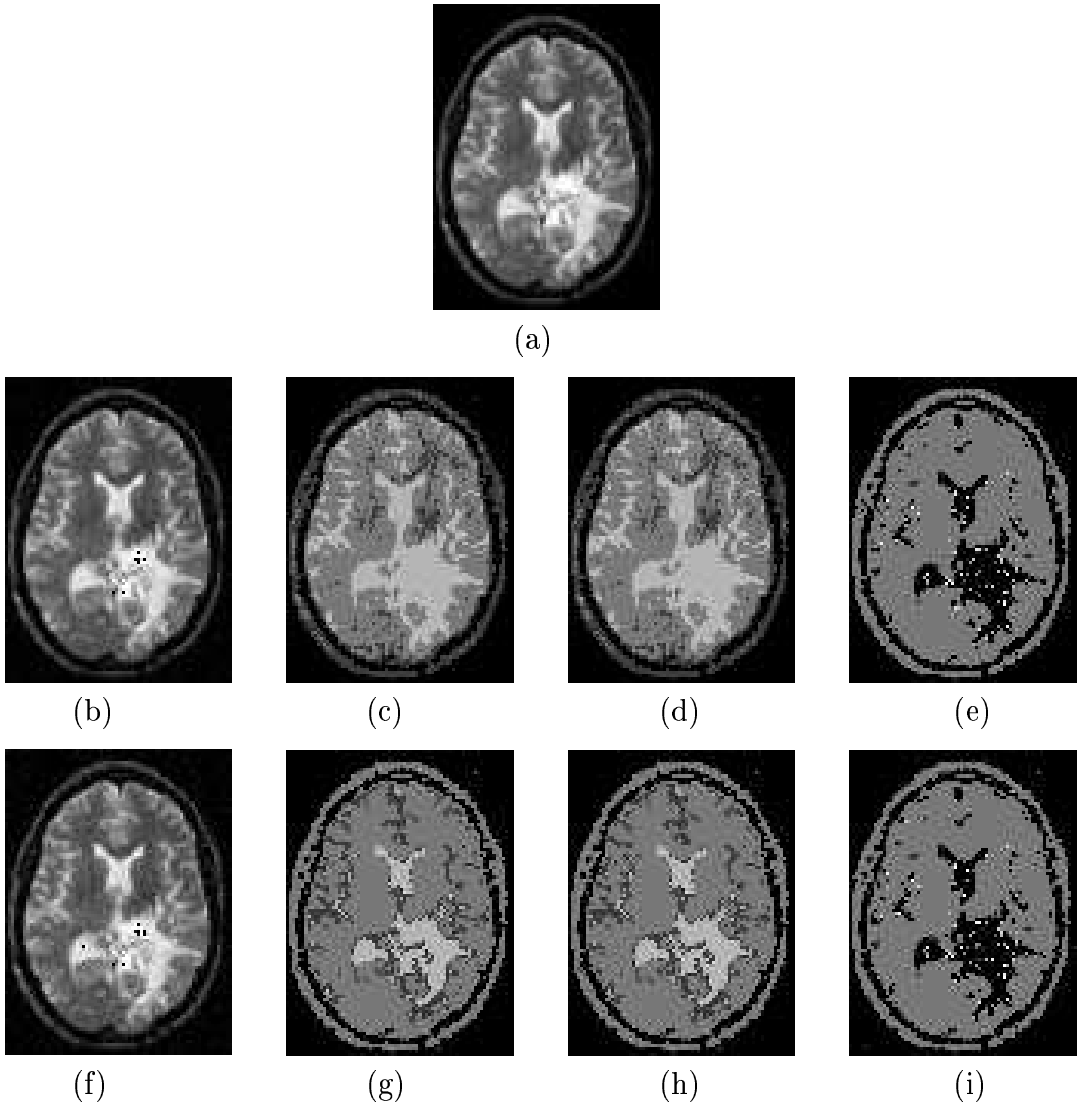

Figure 5.9: *Supervised image segmentation of brain MR image of size* (74×100) *: (a) original image; (b) and (f): noisy images with SNR* 25 *and* $22dB$ *respectively; (c) and (g): corresponding segmented images using HTS Algo. respectively; (d) and (h): corresponding segmented images using SA Algo. respectively; (e) and (i): corresponding segmented images using ICM Algo. respectively.*

class→		1	2	3	4
SNR=25dB	σ	0.079	4.86	0.562	0.408
$\delta = 0.28$	μ	0.052	2.62	1.597	3.265
SNR=22dB	σ	0.08	4.9	0.563	0.409
$\delta = 0.28$	μ	0.053	2.62	1.697	3.265

Table 5.7: *Model parameters of brain MR image of size* (74×100) *with SNR* $25dB$ *and* $22dB$ *of HTS algorithm corresponding to Figure 5.9.*

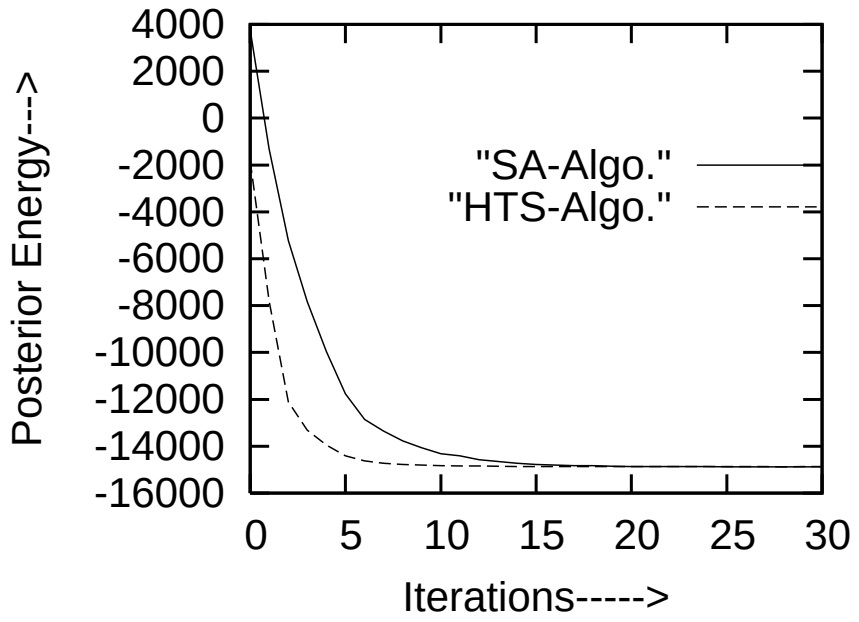

Figure 5.10: *Posterior energy plot of brain MR image of size*(74×100) *for SNR* $25dB$ *using SA algorithm and HTS algorithm.*

Chapter 6

Unsupervised Image Segmentation using HMRF model

6.1 Introduction

In model based image segmentation, often in practice the model parameters are unknown. Since the optimal image label estimates depend upon the optimal value of the model parameters, and vice versa, the problem becomes incomplete data problem. This necessitates to develop a strategy to jointly estimate the model parameters as well as image labels. On the top of this, the number of class labels are assumed to be unknown and hence the problem is viewed as a unsupervised one. Motivated by the work of Dempster *et al.* [36], the problem is formulated in EM framework. The use of Gauss Hidden Markov Random Field (GHMRF) model is motivated by the work of Zhang *et al.* [95]. Since EM algorithm is a recursive one, and the estimates of the model parameters greatly depends upon the estimates of the image labels and vice versa, use of a globally convergent algorithm is motivated to overcome the burden of selection of initial parameters. This globally convergent algorithm also helps in determining the optimal estimates of the model parameters and hence proper segmentation. Obtaining MAP estimates of the images is a horrendous task and hence a hybrid Tabu Search based algorithm is used in this step. The use of the algorithm eventually guides the proposed TEM algorithm to converge to the optimal set of model parameters and hence proper segmentation.

6.2 Problem Statement

In the unsupervised framework, we estimate the class labels and the model parameters alternately to obtain segmentation. The class labels are modeled as MRF model while the observed degraded image is modeled as GHMRF model. Since the estimate of the optimal class labels is dependent on the estimate of optimal set of parameters, this can be viewed as an incomplete data problem. Hence, the MRF model parameters $\theta = \{\theta_l; l \in L\}$ need to be estimated. Specifically, for Gauss Hidden MRF model for the observed image y, the mean and standard deviation of each Gaussian class parameters $\theta_l = (\mu_l, \sigma_l)$ need to be estimated. In EM algorithm, the missing part $\hat{x}$ is estimated with the current θ estimate and then $\hat{x}$ is used to form the complete data set $\{\hat{x}, y\}$. Thereafter, θ is estimated by maximizing the expectation of complete data log likelihood $E[log\ P(x, y \mid \theta)]$. In this case, in E step, the MAP estimates of the class labels are obtained to form the complete data set $(\hat{x}, y)$ using the current estimate of the parameters. In the M step, the ML estimate of the parameter is computed using the class labels computed in E step.

E-step

MAP estimate of X is obtained by using the following optimality criterion.

$$\hat{x}^{(t)} = arg\max_{x} P(X = x \mid Y = y, \theta^t)$$

and there after the expected value is computed as follows.

$$Q = E[log\ P(X = x, Y = y \mid \theta) \mid Y = y, \theta^t]$$

where the parameter θ is the new parameter that is optimized to increase Q and θ^t is the current parameter estimate that is used to evaluate the expectation. $P(X = x \mid Y = y,\ \theta^t)$ is the marginal distribution of the unknown data and is dependent on both the observed data Y and current parameter θ^t.

M-step

ML estimate of parameters is obtained

$$\hat{\theta}^{(t+1)} = arg\max_{\theta} E[log\ P(X = x, Y = y \mid \theta) \mid Y = y, \theta^t]$$

The "E" and "M" steps are repeated till the parameters converge to the optimal set and these optimal parameters set is used for segmentation. In the E step, using

the arbitrary set of parameters, the MAP estimate of the class labels $\hat{x}$ is obtained. These MAP estimates are obtained using HTS algorithm. Subsequently, the $Q = E[log\ P(X = x, Y = y \mid \theta) \mid Y = y, \theta^t]$ is computed which is maximized in the M-step to yield the parameter estimation. The Maximum Likelihood estimate of the GHMRF model parameters are obtained by maximizing the Expected value of the log likelihood function $E[\{log\ P(Y = y \mid \theta, X(t))\} \mid Y = y, \theta^t]$.

6.3 MAP Estimation of Image Labels

The image label estimation is formulated in Bayesian framework using *Maximum a Posteriori* criterion. Here the image model parameters θ and the noise model parameters are assumed to be known. In this EM framework, θ has been estimated in the previous step. Hence given the observed degraded image Y and the current estimate of the parameter $\hat{\theta}$, the estimate of the class labels are obtained by maximizing the posterior distribution. Thus the following optimality criterion is adopted. The following optimality criterion is adopted,

$$\hat{x} = arg \max_x P(X = x \mid Y = y, \theta) \tag{6.1}$$

As described in section 5.3, (6.1) can be expressed as

$$\hat{x} = arg \max_x \left[\frac{1}{Z} exp(-U(x)) \frac{1}{Z'} exp(-U(y \mid x)) \right] \tag{6.2}$$

(6.2) is equivalent to minimizing the following

$$\hat{x} = arg \min_x [U(y \mid x) + U(x)]$$

Substituting for the energy function, $\hat{x}$ can be expressed as

$$\hat{x} = arg \min_x \left[\sum_{i \in S} \{ \frac{(y_i - \mu_{x_i})^2}{2\sigma_{x_i}^2} + log(\sigma_{x_i}) + \sum_{c_i \in C} V_c(x, \phi) \} \right] \tag{6.3}$$

This minimization is achieved by the proposed Hybrid Tabu Search (HTS) Algorithm in the E-step of the TEM algorithm.

6.4 Parameter Estimation in EM framework

At the beginning, an arbitrary value of θ^0 is selected and using θ^0 the current image estimate of x^0 is obtained. Thus, at time "t" of EM algorithm, the image label estimates x^t are obtained using the previously estimated parameter θ^t. This image label estimates x^{t+1} are used to form the complete data set for estimating the model parameters θ^{t+1} for the next recursion. Thus, at time t, the label estimates are available to compute the Q function. Hence the Q function is given by

$$Q(\theta, \theta^t) = E\{\log P(X = x, Y = y \mid \ \theta) \ \mid Y = y, \ \theta^t\}$$

or equivalently

$$Q(\theta, \theta^t) = \sum_{x \in X} P(X = x \mid Y = y, \ \theta^t) \log P(X = x, Y = y \mid \ \theta)$$

For all possible class labels $l \in L$, Q function can be expressed as

$$Q(\theta, \theta^t) = \sum_{l \in L} \sum_{i \in S} P(x_i \mid y_i, \ \theta^t) \ \log P(x_i, y_i \mid \theta)$$

or equivalently

$$Q(\theta, \theta^t) = \sum_{i \in S} \sum_{l \in L} P^t(l \mid y_i) \ \log\{P(y_i \mid x_i) \ P(x_i \mid x_{\eta i}, \ \theta)\} \tag{6.4}$$

Since Y is modeled as GHMRF model and Y_i are conditionally independent (6.4) can be expressed as

$$Q(\theta, \theta^t) = \sum_{i \in S} \sum_{l \in L} P^t(l \mid y_i)\{\log(\frac{1}{\sqrt{2\pi\sigma_l^2}} exp(-\frac{(y_i - \mu_l)^2}{2\sigma_l^2})) + \log P(l \mid x_{\eta i}, \ \theta)\}$$

$$\begin{aligned} or \quad Q(\theta, \theta^t) \ &= \ \sum_{i \in S} \sum_{l \in L} P^t(l \mid y_i)\{-\frac{(y_i - \mu_l)^2}{2\sigma_l^2} - \log \sigma_l - 0.5 \log 2\pi\} \\ &\quad + \log P(l \mid x_{\eta i}, \ \theta) \end{aligned}$$

$$\begin{aligned} or \quad Q(\theta, \theta^t) \ &= \ \sum_{i \in S} \sum_{l \in L} P^t(l \mid y_i)\{-\frac{(y_i - \mu_l)^2}{2\sigma_l^2} - \log \sigma_l \\ &\quad + \log P(l \mid x_{\eta i}, \ \theta)\} \\ &\quad + P^t(l \mid y_i)(-0.5 \log 2\pi) \end{aligned} \tag{6.5}$$

Denoting $C = \{-\frac{(y_i-\mu_l)^2}{2\sigma_l^2} - \log\sigma_l + \log P(l \mid x_{\eta i},\ \theta)\}$ and $D = (-0.5\log 2\pi)$, (6.5) can be expressed as

$$Q(\theta,\theta^t)\sum_{i\in S}\sum_{l\in L} P^t(l \mid y_i)(C+D) \tag{6.6}$$

The current estimate of θ^{t+1} can be obtained by maximizing the following

$$\hat{\theta}^{t+1} = arg\max_{\theta} Q(\theta,\theta^t) \tag{6.7}$$

Substituting $Q(\theta,\theta^t)$ from (6.5), we obtain

$$\begin{aligned} \frac{\partial Q(\theta,\theta^t)}{\partial \mu_l} &= 0 \\ or \qquad \frac{\partial}{\partial \mu_l}\{P^t(l \mid y_i)(-\frac{(y_i-\mu_l)^2}{2\sigma_l^2})\} &= 0 \end{aligned} \tag{6.8}$$

Thus μ_l^{t+1} can be found as $\frac{\sum_{i\in S} P^t(l|y_i)\ y_i}{\sum_{i\in S} P^t(l|y_i)}$.
Similarly Maximizing with respect to σ_l^2, we obtain

$$\begin{aligned} \frac{\partial Q(\theta,\theta^t)}{\partial \sigma_l^2} &= 0 \\ or \qquad \frac{\partial}{\partial \sigma_l^2}\{P^t(l \mid y_i)(-\frac{(y_i-\mu_l)^2}{2\sigma_l^2}) - \log\sigma_l\} &= 0 \end{aligned} \tag{6.9}$$

Thus, the current estimate of the variance $\sigma_l^{2^{t+1}}$ is obtained as $\frac{\sum_{i\in S} P^t(l|y_i)(y_i-\mu_l)^2}{\sum_{i\in S} P^t(l|y_i)}$.
Hence, the parameters are updated as follows.

$$\mu_l^{(t+1)} = \frac{\sum_{i\in S} P^{(t)}(l \mid y_i) y_i}{\sum_{i\in S} P^{(t)}(l \mid y_i)} \tag{6.10}$$

$$\left(\sigma_l^{(t+1)}\right)^2 = \frac{\sum_{i\in S} P^{(t)}(l \mid y_i)(y_i-\mu_l)^2}{\sum_{i\in S} P^{(t)}(l \mid y_i)} \tag{6.11}$$

where $P(l \mid y_i)$ is the probability of $x_i = l$ given the realization y_i, and $\theta_l = (\mu_l, \sigma_l)$ is the parameter (mean and standard deviation) of each class with Gaussian distribution.

6.5 Joint Parameter Estimation and Image label Estimation in EM framework

In the EM framework, image labels as well as the model parameters are estimated recursively until the model parameters converge to the optimal ones. The initial model parameters are selected arbitrarily, and using these parameters θ^0 the image label estimates x^0 are obtained by computing the MAP estimate given in Section 6.3. The MAP estimate is obtained by the proposed HTS algorithm of Section 5.4. Using the label estimates x^0 and the degraded image Y, the model parameter θ^1 is estimated by maximizing the $Q(\theta, \theta^t)$. This recursive process is repeated till the parameters converge to optimal values. These optimal values of parameters are used to obtain the desired segmentation result. The salient steps of the algorithm are enumerated below.

6.6 Tabu-EM Algorithm

1. Initialize the class label to random values and select an arbitrary parameter set.

2. Compute the likelihood distribution $P^{(t)}(Y_i = y_i \mid X_i = x_i)$ and estimate the class labels by MAP estimation

$$\hat{x}^{(t)} = arg \max_x P(X = x \mid Y = y, \theta)$$

   or equivalently

$$\hat{x}^{(t)} = arg \min_x [U(y \mid x) + U(x)]$$

   This is obtained by the proposed hybrid Tabu algorithm using the arbitrary parameter set $\theta = \{\theta_l, l \in L\}$.

3. Compute the posterior distribution

$$P^{(t)}(X_i = l \mid Y_i = y_i) = \frac{g^{(t)}(y_i \mid \theta_l) P^{(t)}(l \mid x_{\eta_i})}{P(y_i)}$$

4. Update the parameters

$$\mu_l^{(t+1)} = \frac{\sum_{i \in S} P^{(t)}(l|y_i) y_i}{\sum_{i \in S} P^{(t)}(l|y_i)} \quad and \quad \left(\sigma_l^{(t+1)}\right)^2 = \frac{\sum_{i \in S} P^{(t)}(l|y_i)(y_i - \mu_l)^2}{\sum_{i \in S} P^{(t)}(l|y_i)}$$

5. Step 2-4 are repeated until a stopping criterion is met.The stopping criterion for our algorithm is: parameters do not change for three consecutive combined iterations.

6.7 Results and Discussions

In simulation, two synthetic images of three and four class and for brain MR images are considered for validating the proposed algorithm. The synthetic images are generated using Gibb's sampler and GHMRF model. The degraded images are obtained by adding additive white Gaussian noise. Thus, the image model can be expressed as follows $Y = X + N$. Where Y denotes the observed degraded image model as GHMRF model, X denotes the image label process modeled as MRF model and N denotes the white Gaussian noise process. The clique potential function $V_c(x, \phi)$ of the *a priori* MRF model considered in simulation is as follows.

$$\begin{aligned} V_c(x) &= -\delta \quad if \quad |x_i - x_j| = 0 \\ &= \delta \quad if \quad |x_i - x_j| \neq 0 \end{aligned} \tag{6.12}$$

where x_i and x_j are the i^{th} and j^{th} pixel values respectively. In this frame work the GHMRF model parameters are estimated together with the image labels. The *a priori* MRF model parameters δ is selected on a trial and error basis. Since the proposed algorithm does not require to have proper choice of initial parameters, the algorithm is tested for different initial conditions in case of synthetic as well as real images. The performance of the algorithm is compared with Zang's [95] approach where the initial parameters are selected using histogram based strategy.

6.7.1 Synthetic Images

The three class synthetic image generated by the Gibb's sampler shown in Fig. 6.1(a). The corresponding noisy image of SNR 20dB is shown in Fig. 6.1(b). The results obtained by the proposed TEM algorithm with three different initial conditions are shown in Figs. 6.1(e), (f), and (g) respectively. The parameters used in TEM algorithm are T_{in}=0.1 and the length of Tabu array K=5. Since the image has three labels, three sets of model parameters corresponding to three different initial

conditions are given in Table 6.1. The initial parameters for each class and the converged ones are tabulated in Table 6.1. The model parameters μ and σ estimated over different iterations of the algorithm are shown in Fig. 6.2. The six figures shown in Fig. 6.2 correspond to three classes and in each class, three different initial conditions. It is clear from these figures that even though the algorithm starts from three different initial conditions, the parameters converge to either a single value or values that are very close to each other. This is also corroborated by the initial and final values given in Table 6.1.

For example, the σ of the fourth class starts from three different values but converges to the same value of 0.046. Similar observations are also made for other parameters of other classes. This fact is reinforced from the results shown in Figs. 6.1(e), (f) and (g). Proper segmentation could be achieved even starting the algorithm from three different initial conditions. For the sake of comparison, Zhang's approach is also implemented and the result obtained by Zhang's approach is shown in Fig 6.1(c). In Zhang's approach, the initial parameters are determined using the histogram of the noisy image. As seen from Figs. 6.1(c), (e), (f) and (g) the results obtained by TEM algorithm is visibly comparable to that of Zhang's approach. The estimation of parameters over each epoch of Zhang's approach is shown in Fig. 6.3. Of Zhang's algorithm, that employ ICM algorithm, is run with one of the starting conditions of TEM, the parameters do not converge to the optimal ones and hence improper segmentation is obtained as shown in Fig. 6.1(d). The estimated parameters are shown in Fig. 6.2 together with the parameters of TEM also. The segmented result of Fig. 6.1(d) does not even possess three main classes rather two broad classes are obtained. This clearly indicates that the estimated model parameters and the image labels are converged to suboptimal values. This indicates that Zhang's approach is sensitive to initial model parameters. This could be attributed to use of locally convergent ICM algorithm. The word arbitrary in our algorithm does not imply a completely random set rather from a set of values. This is conceivable because the algorithm converges to optimal one starting from a bounded set. The TEM algorithm is also successfully tested with high noise conditions as shown in Fig. 6.4. The model parameters used for the three noisy conditions are

tabulated in Table 6.3. The converged values of the parameters are different because of different noise conditions. It is clear from the result of Fig. 6.4 that at a low SNR of 12dB, the number of misclassified pixels are more as compared to cases SNR 18 and 15 dB as seen from Figs. 6.4(d) and (e) respectively.

The unsupervised scheme with the proposed TEM algorithm is also validated for a four class synthetic image as shown in Fig. 6.5(a). The corresponding noisy image is shown in Fig. 6.5(b). The model parameters used by TEM algorithm for four different initial conditions and that used by Zhang's also are presented in Tables 6.4 and 6.5 respectively. The results obtained by TEM algorithm corresponding to four different initial conditions, are shown in Figs., 6.5(d), (e), (f) and (g) respectively. It is clear from these figures that four distinct different classes could be obtained and hence proper segmentation could be achieved. The parameters used in TEM algorithm are same as that of the 3 class synthetic image case. The result obtained by Zhang's algorithm is shown in Fig. 6.5(c). Although the result obtained by TEM are comparable to that of Zhang's algorithm, the proposed TEM algorithm yields proper segmented images even starting from four different initial conditions. Hence, the proposed algorithm does not require to have a proper choice of initial parameters. The convergence of the μ and σ for different classes with different initial conditions are shown in Fig. 6.6. It is observed from these figures that the different μ and σ values converged to single values even from four different initial conditions.

The TEM algorithm is also tested with two high noisy conditions as shown in Figs. 6.7(a) and (b). The model parameters used in these cases are tabulated in Table 6.6. The algorithm yielded satisfactory results for 18dB SNR. The performance degrade for noisy image of SNR 15dB. As found in supervised framework, the performance of the algorithm degrades with increase in noise strength.

6.7.2 Brain MR Images

One of the real images considered is shown in Fig. 6.8(a). The corresponding noisy image of SNR 25dB is shown in Fig. 6.8(b). TEM algorithm is employed with three different initial conditions. Four different classes are assumed and the initial and final model parameters are tabulated in Table 6.7. Figs. 6.7(d), (e) and (f) show the

results obtained by TEM algorithm. It is observed that four distinct classes could be obtained with three different initial conditions. Since exact number of classes are unknown, the algorithm is run from higher number of initial classes and eventually the algorithm converged to four classes. The result obtained by Zhang's approach is shown in Fig. 6.8(c). The initial model parameters determined from the respective histogram and the final model parameters are presented in Table 6.8. It is clear from Figs. 6.8(c), (d), (e) and (f) that the results obtained by the TEM algorithm are comparable with that of Zhang's approach. The model parameters used in TEM algorithm are T_{in}=0.2 and K=5. But, TEM algorithm does not require to determine proper initial parameters as opposed to Zhang's approach. The estimation of model parameters μ and σ for four classes and for three different initial conditions are shown in Fig. 6.9. It is seen from these figures that almost in all classes the parameters converged to a single value except in Fig. 6.9(d), where the σ converges to a different values. However, the converged values are close to each other. This is also observed from the tabulated values of Table 6.7. The estimation of model parameters using Zhang's approach is also shown in Fig. 6.10. The initial values in this figure are obtained by histogram method. This shows that the result obtained by Zhang's approach is dependent on initial value of the parameters. The algorithm is also tested with noisy images of SNR 22, 20 and 18dB as shown in Figs. 6.11(a), (b) and (c) respectively. The initial GHMRF model parameters and the converged ones for the three noisy cases are tabulated in Table 6.9. It is observed from Fig. 6.11(f) that at a high noise of 18dB, there is degradation in performance. At noisy cases of 22dB and 20dB, four distinct classes are obtained as seen from Figs. 6.11(d) and (e).

The second real brain MR image considered is of size (227x195) and is shown in Fig. 6.12(a). The noisy image of SNR 25dB is shown in Fig. 6.12(b). Figs. 6.12(d), (e) and (f) show results corresponding to three different initial conditions. Here also the algorithm starts from three different initial conditions and eventually converges to the parameters as given in Table 6.10. The parameters used in TEM algorithm are $T_{in} = 0.1$ and the length of the Tabu array $K = 5$. It is observed from the results obtained by TEM algorithm is that the four distinct classes could

be obtained even from different initial conditions. The estimation of parameters for four classes over the different epochs are shown in Fig. 6.13. Almost in all cases, the parameters converged to a single value. In some classes, the parameter converged values that are very close to each other. This can be observed from Figs. 6.13(g) and (h). Even with these parameters the proper labeling of the pixels could be obtained. This corroborates that the algorithm yields satisfactory results from arbitrary initial conditions. The results obtained by TEM algorithm are compared with the results obtained by Zhang's approach as shown in Fig. 6.12(c). The initial parameters are computed using the histogram of the noisy image. The initial parameters and the converged values of the parameters are tabulated in Table 6.11. The estimation of the model parameters starting with the precomputed initial conditions are shown in Fig. 6.14. From Fig. 6.12(e) it is clear that four broad classes could be obtained, but, because of noisy conditions some misclassification are observed at the top of this image. This may be attributed to the choice of the initial parameters and the local convergent property of the algorithm. Besides different initial conditions, TEM algorithm is also tested for high noisy conditions i.e. for SNRs 22dB, 20dB and 18dB respectively. The noisy images and the corresponding segmented results are shown in Fig. 6.15. It is observed that misclassified pixels are observed with increase in noise strength i.e. at SNR 18dB, the mislabeling of pixels are more than that of low noise conditions. The parameters used for these three noisy conditions are tabulated in Table 6.12.

The third brain MR image considered in simulation is shown in Fig. 6.16(a). The corresponding noisy image of SNR 25dB is shown in Fig. 6.16(b). The results obtained by TEM algorithm are shown in Figs. 6.16(d), (e) and (f) for different initial conditions. It is observed in these cases that four distinct classes could be obtained but the values of class labels were different for different initial conditions. But proper segmentation could be obtained. The parameters used for TEM algorithm are $T_{in} = 0.2$ and length of the Tabu array is $k = 5$. The convergence of different parameters corresponding to different classes are shown in Fig. 6.17. In this case also, similar observations are made as in the previous cases. The parameters converged to either a single value or to values that are close to each other.

These results are also compared with the results obtained by Zhang's approach as shown in Fig. 6.16(e). The initial and final model parameters are given in Table 6.14 and the convergence of the parameters of the different classes are shown in Fig. 6.18. Comparing the result of TEM and Zhang's algorithm, it is obtained that in TEM algorithm although four different classes could be obtained, the class label values are different from that of Zhang's approach. The TEM algorithm could also be successfully tested with high noise conditions as shown in Fig. 6.19. The parameters used in these classes are presented in Table 6.15. Similar observation of degradation in performance at high noise condition is observed in this case as seen from Fig. 6.19(a).

The last brain MR image considered is shown in Fig. 6.20(a) and the corresponding noisy image of SNR 25dB is shown in Fig. 6.20(b). The results of Figs. 6.20(d), (e), (f) and (g) correspond to four different initial conditions. The TEM algorithm parameters are $T_{in} = 0.5$ and Tabu length of K=10. The initial and the converged values of the model parameters are given in Table 6.16. The estimation of these parameters are shown in Fig. 6.21, where observations similar to the previous cases are also made. The misclassification could be attributed to the different converged values of the parameters corresponding to different initial conditions. The results obtained by Zhang's approach is shown in Fig. 6.20(c) and the corresponding initial and final parameters are given in Table 6.17. The estimation of parameters are shown in Fig. 6.22. The results obtained by TEM algorithm is comparable to Zhang's approach. The TEM algorithm also could be successfully tested for high noise conditions as shown in Fig. 6.23 where it is seen that the performance of the algorithm deteriorates with increase in noise strength. The model parameters are tabulated in Table 6.18.

6.8 Conclusions

In this chapter, the problem of unsupervised image segmentation of brain MR images is addressed. Here, the number of classes, the image model parameters and the image labels are assumed to be unknown. The proposed unsupervised algorithm assumes more number of initial classes and eventually converges to the required number of

classes. More number of initial classes imply more number of model parameters. Since each class is modeled as Gaussian distribution and is characterized by mean (μ) and variance (σ^2), the total number of parameters become twice the number of classes. It is observed that the model parameters greatly affect the image class or label estimation and thus segmentation. The parameters evolve from the selected initial set and converges to a new set of parameters that decide the number of labels. Hence, the estimation of model parameters is one of the crucial issue. The model parameters estimated by Zhang *et al.* [95] are found to be very much dependent on the choice of initial parameters. Therefore, they have suggested a histogram based approach for determination of the proper initial choice of model parameters. In their approach, the accuracy of segmentation depends upon the proper choice of initial parameters. This although appears not to be a serious bottleneck in the unsupervised framework, the problem becomes more compounded in case of high noise conditions.

In order to make the existing scheme an unsupervised one, attempts have been made to propose an algorithm that does not depend upon the proper choice of initial model parameters. Towards this end, TEM algorithm is proposed that is independent of proper choice of initial model parameters. It has also been demonstrated that the algorithm converges to same or almost same parameters despite starting from different initial model parameters. This issue of convergence of model parameters has been demonstrated for both synthetic as well as brain MR images. It has also been demonstrated that if the algorithm proposed by Zhang starts from the same initial condition as ours, it converges to model parameters that lead to incorrect segmentation. This phenomenon has been observed for synthetic images with different classes but a comparison is presented only for three class problem. Furthermore, in some cases, the results obtained by Zhang's approach are visually inferior as compared to the results obtained by the proposed algorithm. The proposed algorithm also yields satisfactory results for high noise conditions.

Similar observations, as regards the convergence of image model parameters, are also made for real images. For the brain MR image of Fig. 6.8, some of the classes are observed to be misclassified. This is also reflected in case of Zhang's

approach. This could be attributed to the inability of the model to capture the intrinsic characteristics of the given images. However for the rest three brain MR images, almost correct classification could be achieved as reflected in Fig. 6.12, Fig. 6.16 and Fig.6.20. In these cases, the parameters converged to almost same values from different initial conditions. The convergence of parameters are presented only for the final correct classes. The parameters for other initial classes are not presented. With high noise condition, Zhang's approach yielded some misclassification while the proposed one yielded satisfactory performance.

The proposed approach assumes to have the knowledge of the MRF model parameters δ. The same is also true for Zhang's approach. The results reported are the best results depending on the assumption δ on a trial and error basis. The results may be further improved by estimating δ together with the model parameters that will make the system completely unsupervised. Arbitrary initial model parameters in the proposed scheme implies that the parameters are from a set with a bound rather than from any unbounded set. Theoretical justification of these bounds is worth pursuing. Thus, an unsupervised scheme is proposed that worked satisfactorily for synthetic as well as brain MR images.

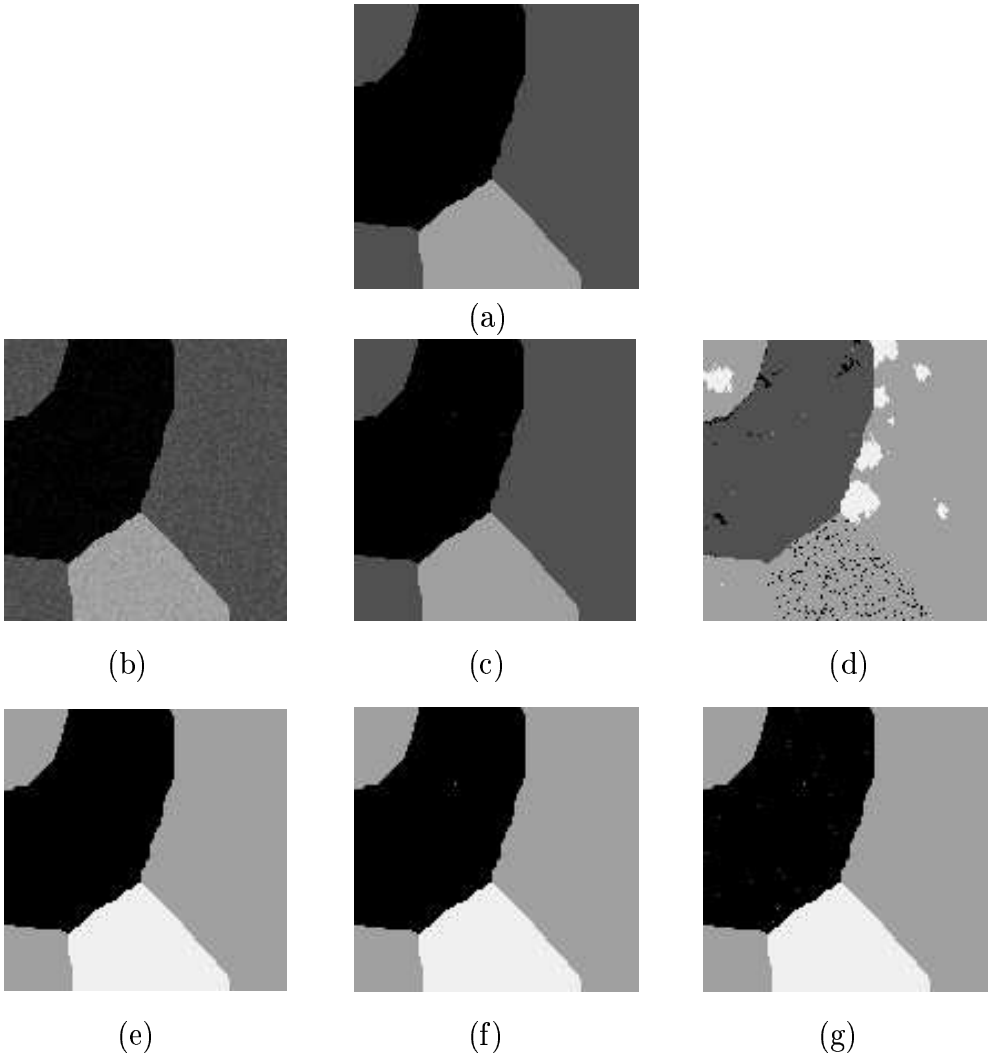

Figure 6.1: *Unsupervised segmentation of synthetic* 3*-class image of size* (128×128)*: (a) original image; (b) noisy image with SNR* $20dB$*; (c) segmented image using Zhang's approach; (d) segmented image using Zhang's approach with arbitrary initial parameters; (e),(f) and (g): segmented images using TEM Algo. corresponding to three different initial conditions.*

Class →		1	2	3
$\delta = 1.2$	μ_{i1}	0.3	0.2	0.8
	σ_{i1}	0.1	0.2	0.1
	μ_{f1}	0.0311	0.0022	0.9928
	σ_{f1}	0.0461	0.0052	0.104
$\delta = 1.2$	μ_{i1}	0.27	0.25	0.85
	σ_{i1}	0.12	0.18	0.12
	μ_{f1}	0.03	0.0001	0.9928
	σ_{f1}	0.046	0.0017	0.1044
$\delta = 1.2$	μ_{i1}	0.32	0.15	0.75
	σ_{i1}	0.14	0.22	0.14
	μ_{f1}	0.03	0.0018	0.9928
	σ_{f1}	0.046	0.0022	0.104

Table 6.1: *Image model parameters of synthetic* 3*-class image of size* (128×128) *with SNR=*$20dB$ *correspond to three different initial conditions of TEM algorithm.*

Class →		1	2	3
$SNR = 20dB$	μ_{i1}	0.875	1.85	2.00
$\delta = 1.0$	σ_{i1}	0.55	0.384	0.4
	μ_{f1}	0.99	1.997	2.006
	σ_{f1}	0.247	0.235	0.12

Table 6.2: *Parameters of synthetic* 3*-class image of size* (128×128) *with SNR=*$20dB$ *using Zhang's approach.*

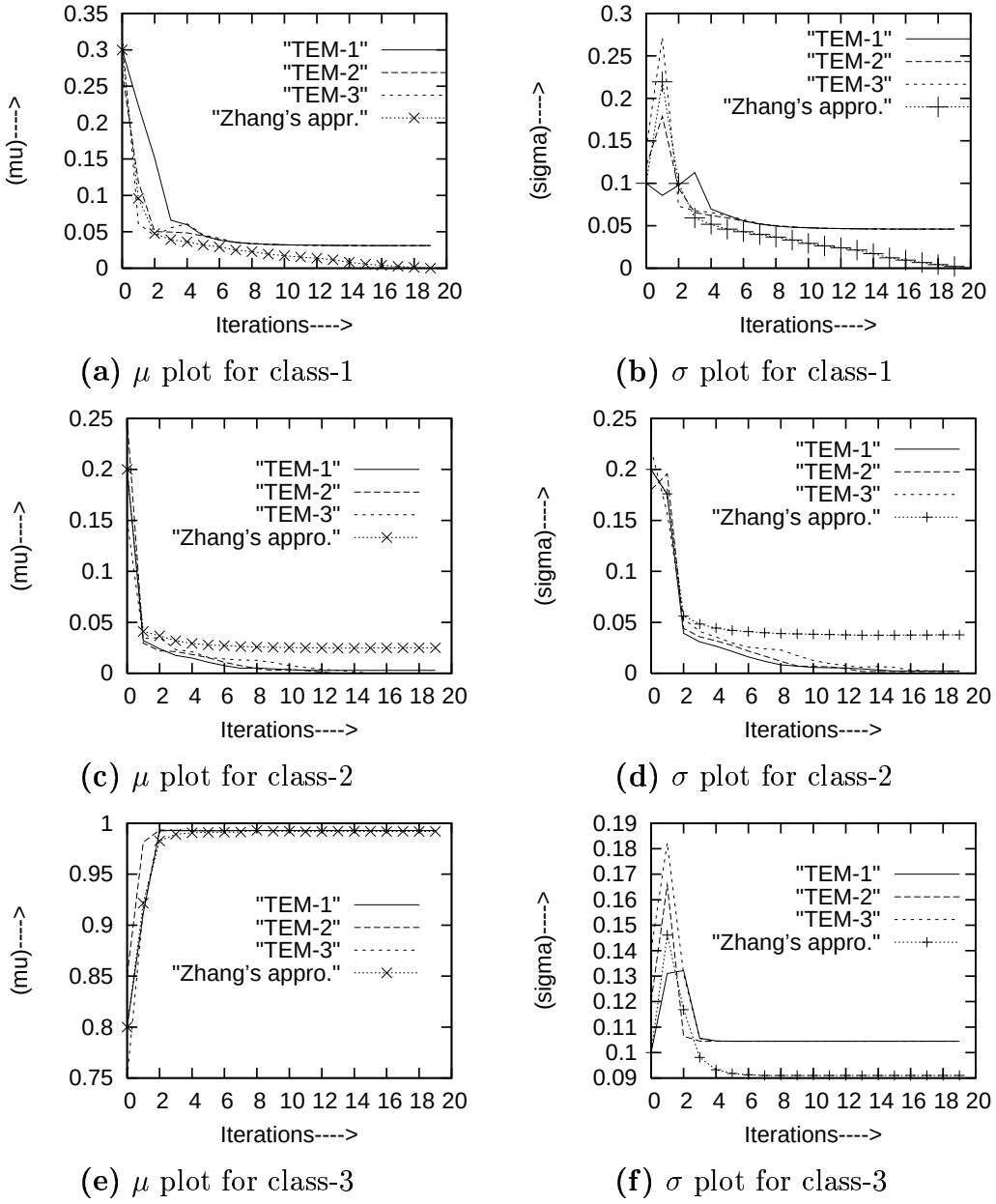

(a) μ plot for class-1

(b) σ plot for class-1

(c) μ plot for class-2

(d) σ plot for class-2

(e) μ plot for class-3

(f) σ plot for class-3

Figure 6.2: *Convergence of the image model parameters of synthetic 3-class image corresponding to 3 different initial conditions of TEM algorithm and the convergence of model parameters using Zhang's approach starting from one of the initial conditions of TEM algorithm.*

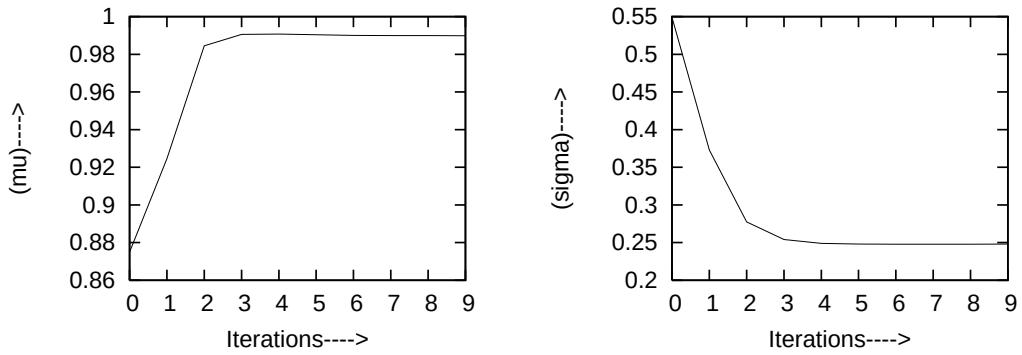

(a) μ plot for class-1

(b) σ plot for class-1

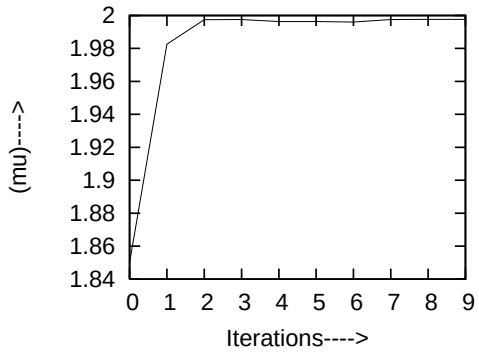

(c) μ plot for class-2

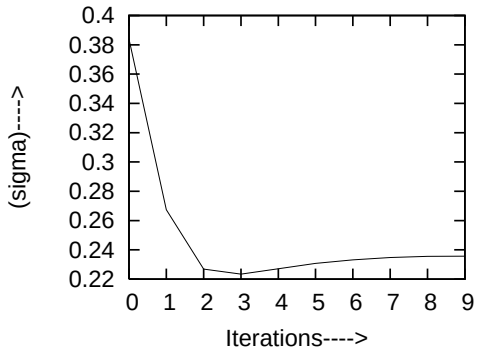

(d) σ plot for class-2

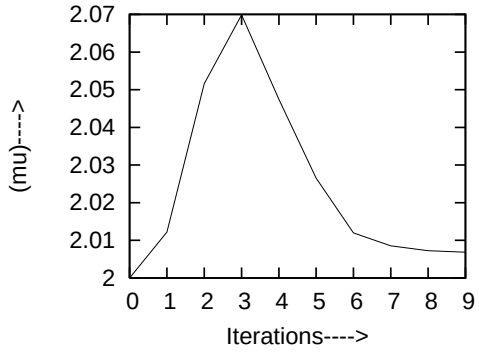

(e) μ plot for class-3

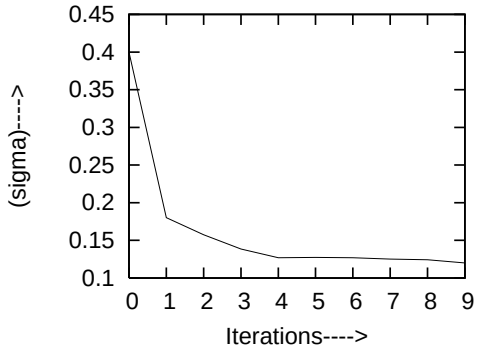

(f) σ plot for class-3

Figure 6.3: *Convergence of the image model parameters of synthetic* 3*-class image using Zhang's approach corresponding to Table 6.2.*

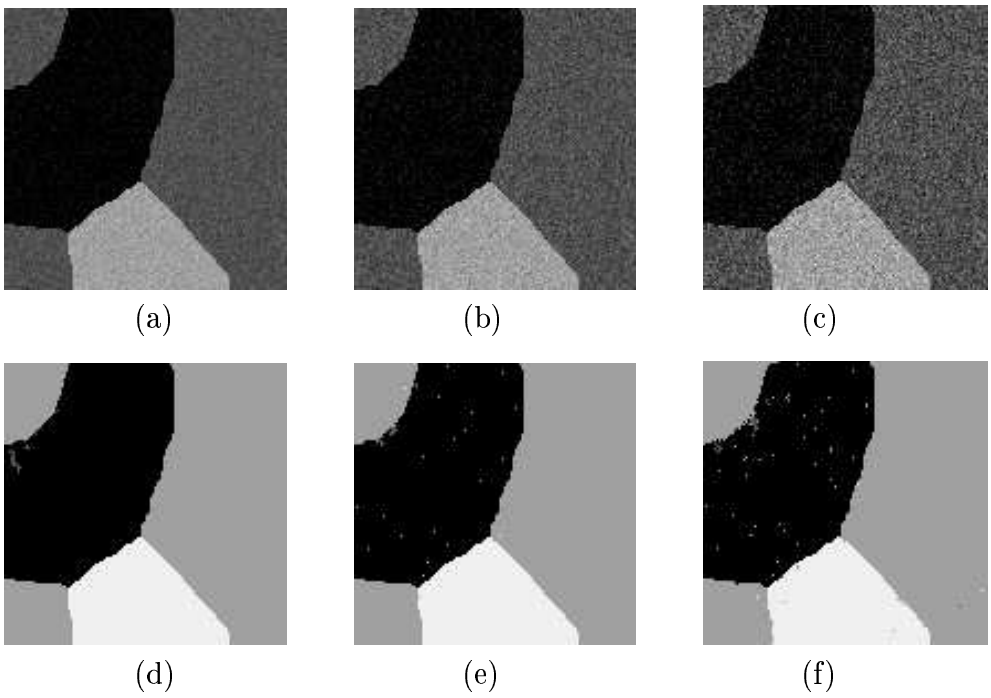

Figure 6.4: *Unsupervised segmentation of synthetic* 3*-class image of size* (128×128) *using TEM algorithm: (a),(b)and (c): noisy images with SNR* $18dB$*,* $15dB$*,* $12dB$ *respectively; (d),(e) and (f): corresponding segmented images respectively.*

Class		1	2	3
SNR	μ_i	0.3	0.2	0.8
18dB	σ_i	0.1	0.2	0.1
	μ_f	0.04	0.004	0.992
$\delta = 1.2$	σ_f	0.0592	0.013	0.1314
SNR	μ_i	0.3	0.15	0.8
15dB	σ_i	0.1	0.2	0.1
	μ_f	0.0581	0.0011	0.991
$\delta = 1.2$	σ_f	0.0848	0.0114	0.185
SNR	μ_i	0.3	0.15	0.8
12dB	σ_i	0.1	0.2	0.1
	μ_f	0.0843	0.0003	0.99
$\delta = 1.2$	σ_f	0.121	0.002	0.263

Table 6.3: *Image model parameters of TEM algorithm for synthetic* 3*-class image of size* (128×128) *with SNR of* $18dB$*,* $15dB$ *and* $12dB$ *respectively.*

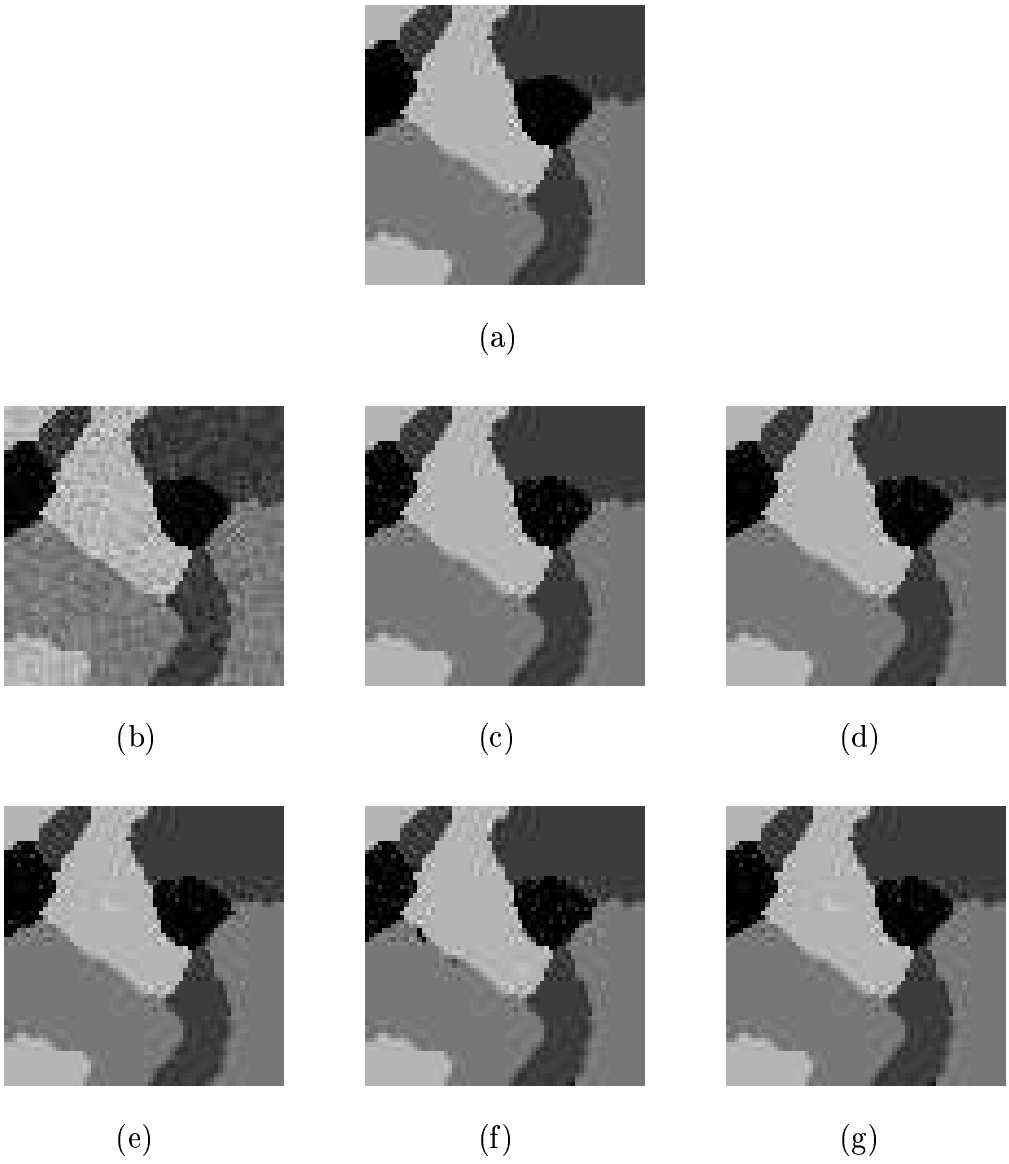

Figure 6.5: *Unsupervised segmentation of synthetic* 4*-class image of size* (64×64)*: (a) original image; (b) noisy image with SNR* $20dB$*; (c) segmented image using Zhang's approach; (d),(e),(f) and (g): segmented images using TEM algorithm corresponding to four different initial conditions.*

Class→		1	2	3	4
$\delta = 0.7$	μ_{i1}	0.04	1.1	1.5	2.9
	σ_{i1}	1.15	0.28	0.35	0.35
	μ_{f1}	0.037	0.998	2.00	2.989
	σ_{f1}	0.063	0.19	0.192	0.19
$\delta = 0.7$	μ_{i2}	0.06	1.15	1.55	2.92
	σ_{i2}	1.1	0.25	0.4	0.37
	μ_{f2}	0.037	0.988	2.00	2.98
	σ_{f2}	0.062	0.19	0.192	0.19
$\delta = 0.7$	μ_{i3}	0.03	1.05	1.58	2.8
	σ_{i3}	1.0	0.2	0.38	0.36
	μ_{f3}	0.027	.988	2.0	2.98
	σ_{f3}	0.048	0.19	0.192	0.19
$\delta = 0.7$	μ_{i4}	0.05	1.18	1.45	2.95
	σ_{i4}	1.0	0.2	0.42	0.34
	μ_{f4}	0.038	0.988	2.00	2.987
	σ_{f4}	0.048	0.19	0.192	0.19

Table 6.4: *Image model parameters of synthetic* 4*-class Image of size* (64×64) *with SNR=*$20dB$ *correspond to four different initial conditions of TEM algorithm.*

Class→		1	2	3	4
$SNR = 20dB$	μ_{i1}	0.11	1.0	1.95	2.8
$\delta = 0.8$	σ_{i1}	0.492	0.606	0.584	0.54
	μ_{f1}	0.007	0.97	2.009	2.98
	σ_{f1}	0.02	0.48	0.36	0.355

Table 6.5: *Parameters of synthetic 4-class image of size* 128×128 *with SNR=*$20dB$ *using Zhang's approach.*

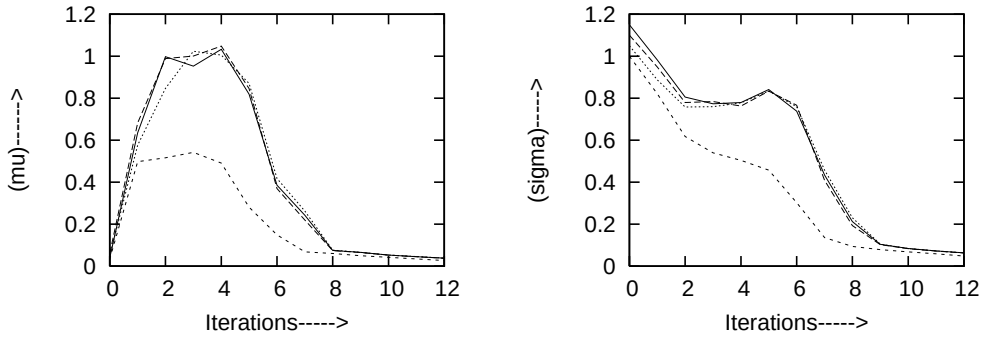

(a) μ plot for class-1 **(b)** σ plot for class-1

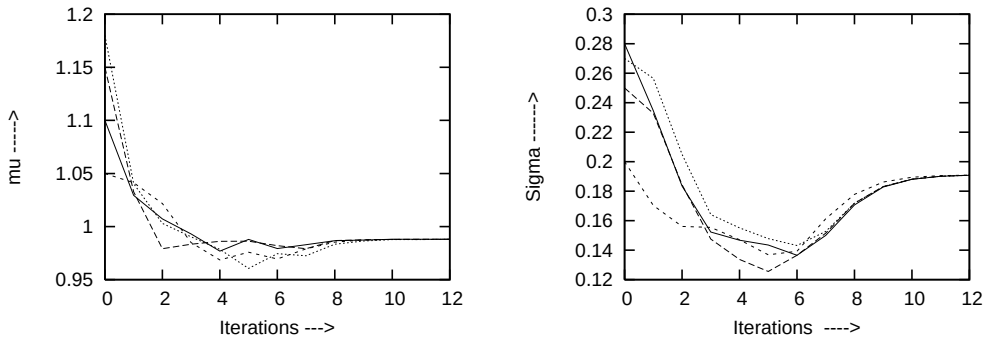

(c) μ plot for class-2 **(d)** σ plot for class-2

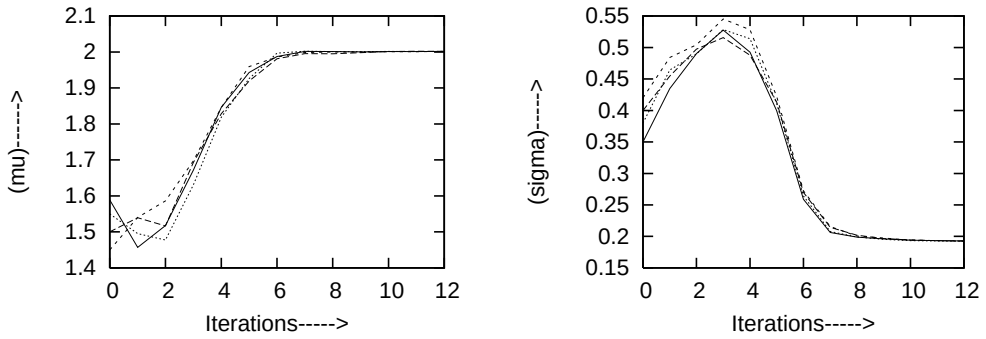

(e) μ plot for class-3 **(f)** σ plot for class-3

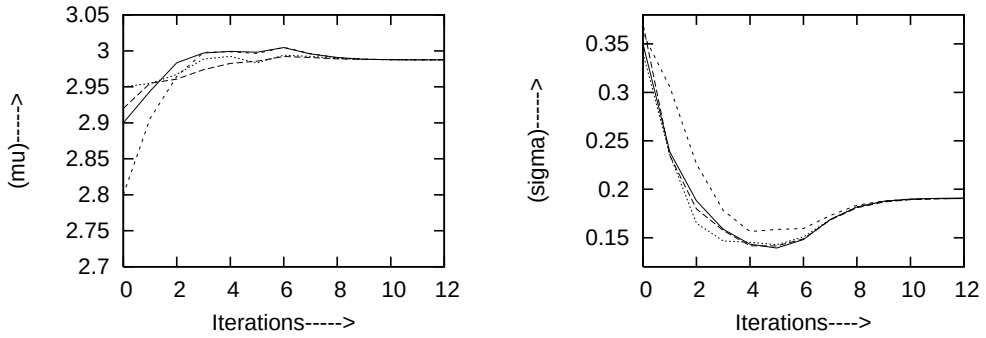

(g) μ plot for class-4 **(h)** σ plot for class-4

Figure 6.6: *Convergence of image model parameters of TEM algorithm of synthetic 4-class image corresponding to Table 6.4.*

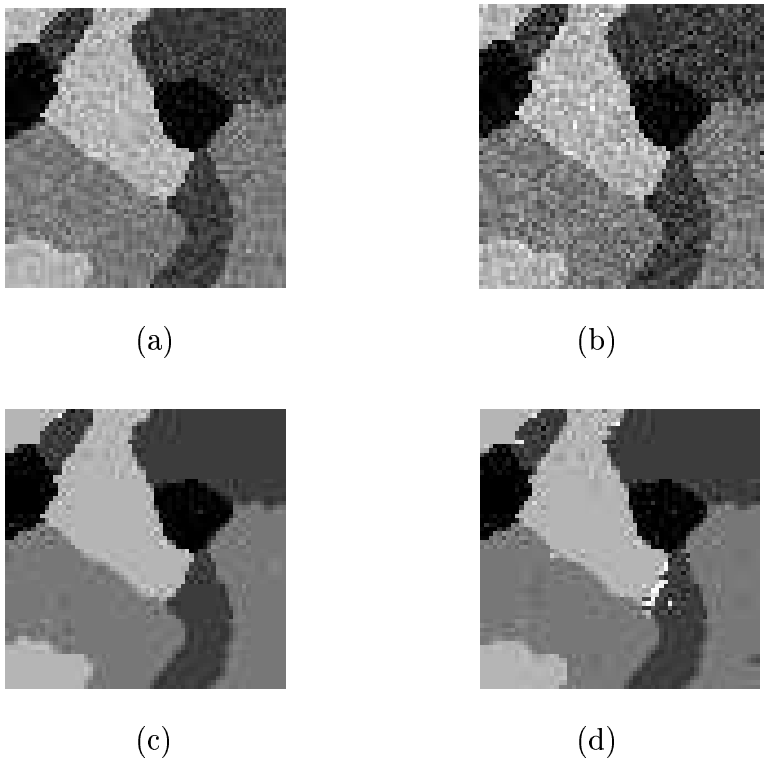

(a) (b)

(c) (d)

Figure 6.7: *Unsupervised segmentation of synthetic* 4*-class image of size* (64×64) *using TEM algorithm: (a) and (b): noisy images with SNR* $18dB$ *and* $15dB$ *respectively; (d) and (e): corresponding segmented images respectively.*

Class		1	2	3	4
SNR	μ_i	0.2	1.6	2.3	2.2
18dB	σ_i	0.5	0.9	0.3	0.5
	μ_f	0.051	0.991	2.0	2.989
$\delta = 0.7$	σ_f	0.080	0.2	0.199	0.201
SNR	μ_i	2.2	0.6	1.3	1.2
15dB	σ_i	1.5	0.2	0.8	1.5
	μ_f	0.005	0.994	2.0	2.997
$\delta = 0.7$	σ_f	0.088	0.253	0.252	0.25

Table 6.6: *Image model Parameters of TEM algorithm for synthetic* 4*-class image of size* (64×64) *with SNR of* $18dB$ *and* $15dB$ *respectively.*

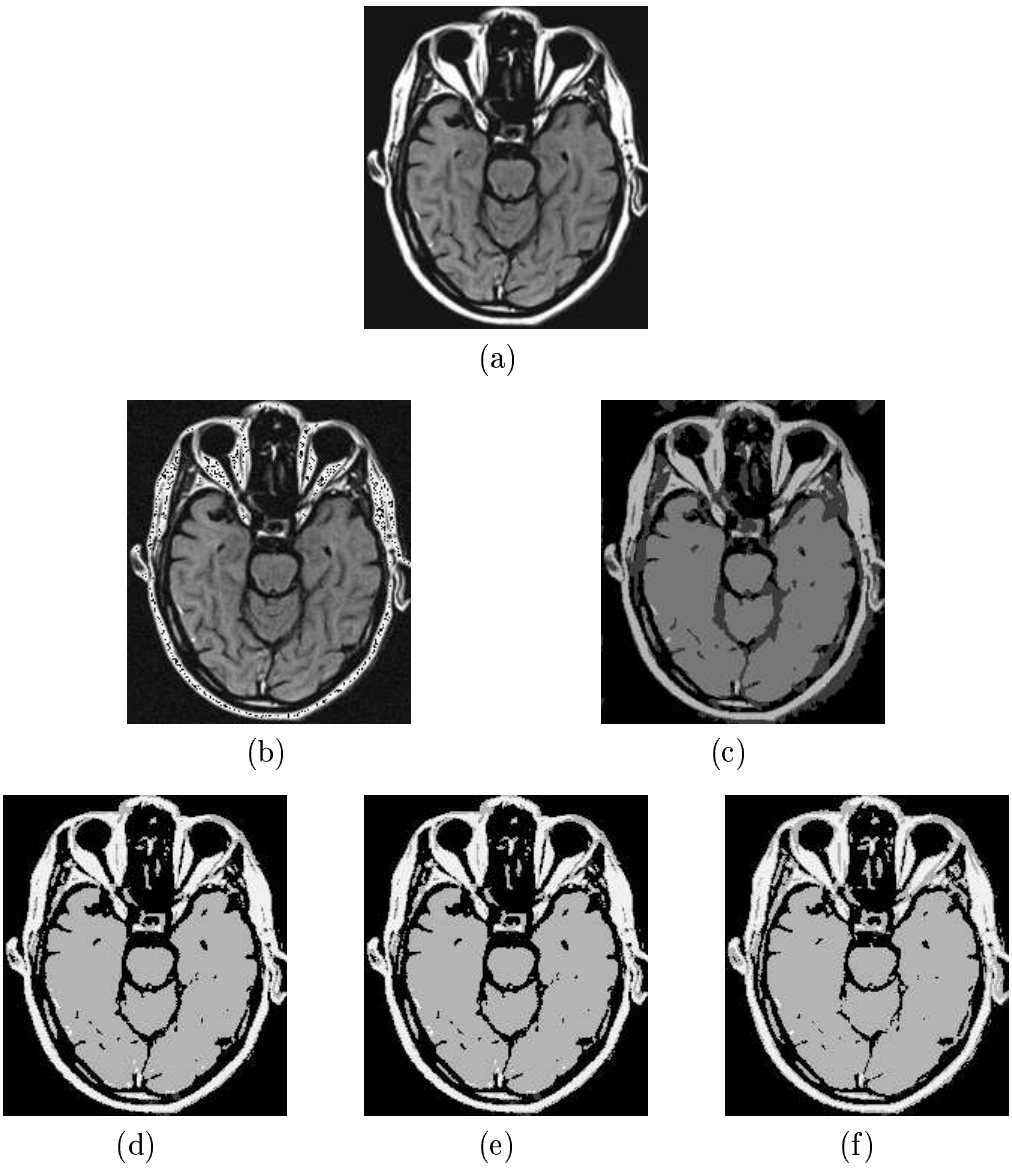

Figure 6.8: *Unsupervised segmentation of brain MR image of size* (189×217)*: (a) original image, (b) noisy image with SNR* $25\,dB$*, (c) segmented image using Zhang's approach, (d),(e) and (f): segmented images using TEM algorithm corresponding to three different initial conditions.*

Class→		1	2	3	4
$\delta = 0.4$	μ_{i1}	2.0	1.0	2.0	2.0
	σ_{i1}	0.6	0.3	0.5	1.0
	μ_{f1}	0.36	0.36	2.07	1.91
	σ_{f1}	0.08	0.031	0.042	0.21
$\delta = 0.4$	μ_{i2}	1.6	1.1	2.1	1.9
	σ_{i2}	0.62	0.34	0.55	1.2
	μ_{f2}	0.358	0.32	2.083	1.92
	σ_{f2}	0.074	0.03	0.03	0.22
$\delta = 0.4$	μ_{i3}	1.8	0.9	1.9	2.1
	σ_{i3}	0.65	0.26	0.53	1.1
	μ_{f3}	0.35	0.38	2.0803	1.91
	σ_{f3}	0.074	0.023	0.014	0.201

Table 6.7: *Image model parameters of TEM algorithm for brain MR image of size* (189×217) *with SNR* $25dB$ *correspond to three different initial conditions.*

Class →		1	2	3	4
$SNR = 25dB$	μ_{i1}	0.2	1.01	1.398	3.28
$\delta = 0.4$	σ_{i1}	0.34	0.607	0.625	0.65
	μ_{f1}	0.357	0.363	1.92	4.19
	σ_{f1}	0.066	0.083	0.197	0.063

Table 6.8: *Image model parameters for brain MR image of size* (189×217) *with SNR*=$25dB$ *using Zhang's approach.*

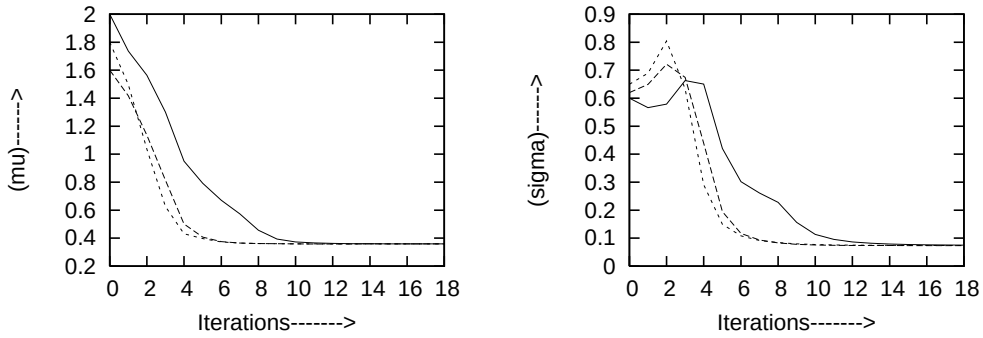

(a) μ plot for class-1 **(b)** σ plot for class-1

(c) μ plot for class-2 **(d)** σ plot for class-2

(e) μ plot for class-3 **(f)** σ plot for class-3

(g) μ plot for class-4 **(h)** σ plot for class-4

Figure 6.9: *Convergence of image model parameters of TEM algorithm corresponding to Table 6.7.*

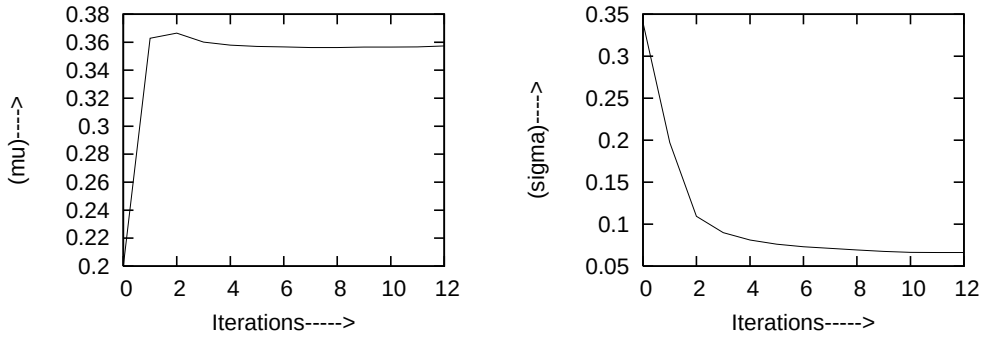

(a) μ plot for class-1

(b) σ plot for class-1

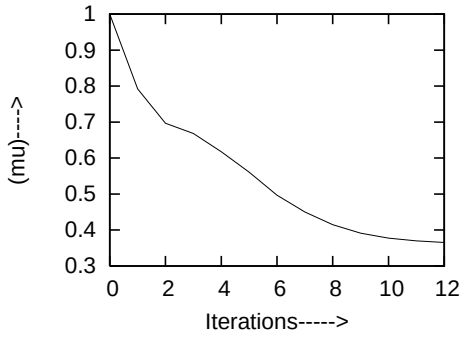

(c) μ plot for class-2

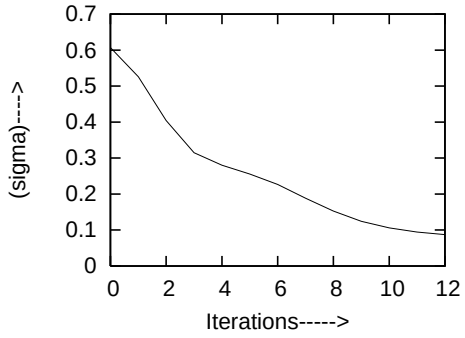

(d) σ plot for class-2

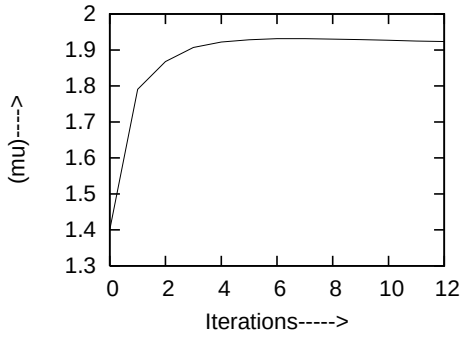

(e) μ plot for class-3

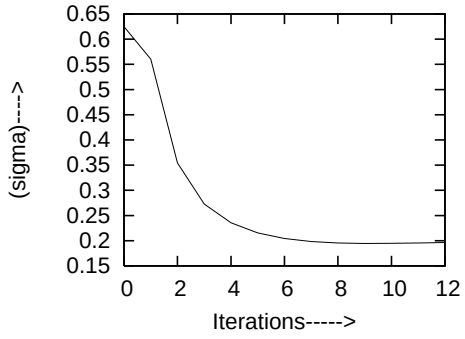

(f) σ plot for class-3

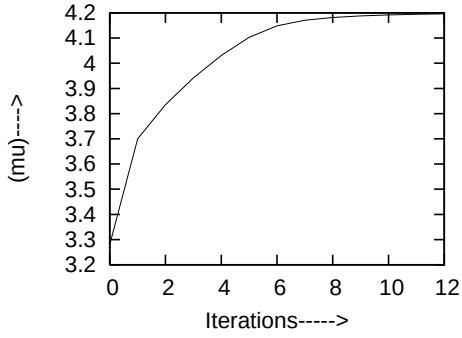

(g) μ plot for class-4

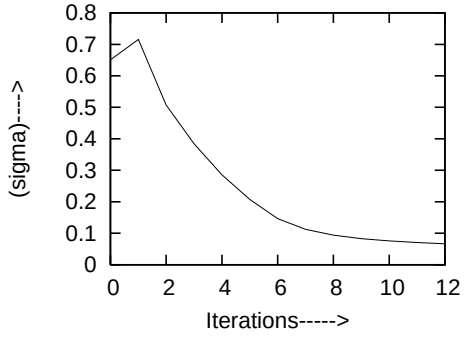

(h) σ plot for class-4

Figure 6.10: *Convergence of image model parameters of brain MR image using Zhang's approach corresponding to Table 6.8*

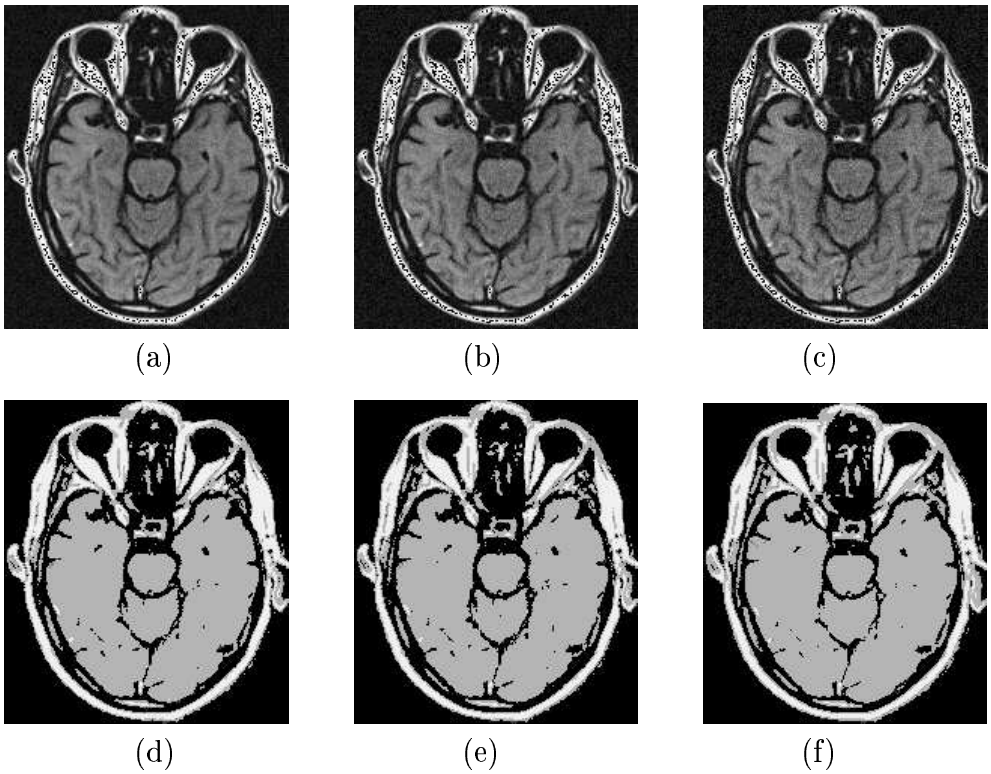

Figure 6.11: *Unsupervised segmentation of brain MR image of size* (189×217) *using TEM algorithm: (a),(b)and (c) : noisy images with SNR* $22dB$, $20dB$, $18dB$ *respectively; (d),(e) and (f): corresponding segmented images respectively.*

Class		1	2	3	4
SNR	μ_i	2.0	1.0	2.0	2.0
22dB	σ_i	0.6	0.3	0.5	1.0
	μ_f	0.363	0.396	2.034	1.90
$\delta = 0.4$	σ_f	0.105	0.005	0.005	0.217
SNR	μ_i	2.0	1.0	2.0	2.0
20dB	σ_i	0.6	0.3	0.5	1.0
	μ_f	0.367	0.42	2.04	1.911
$\delta = 0.4$	σ_f	0.133	0.007	0.008	0.232
SNR	μ_i	2.0	1.0	2.0	2.0
18dB	σ_i	0.6	0.3	0.5	1.0
	μ_f	0.373	0.343	1.958	1.911
$\delta = 0.4$	σ_f	0.173	0.17	0.008	0.25

Table 6.9: *Image model parameters of TEM algorithm for brain MR image of size* (189×217) *with SNR of* $22dB$, $20dB$ *and* $18dB$ *respectively.*

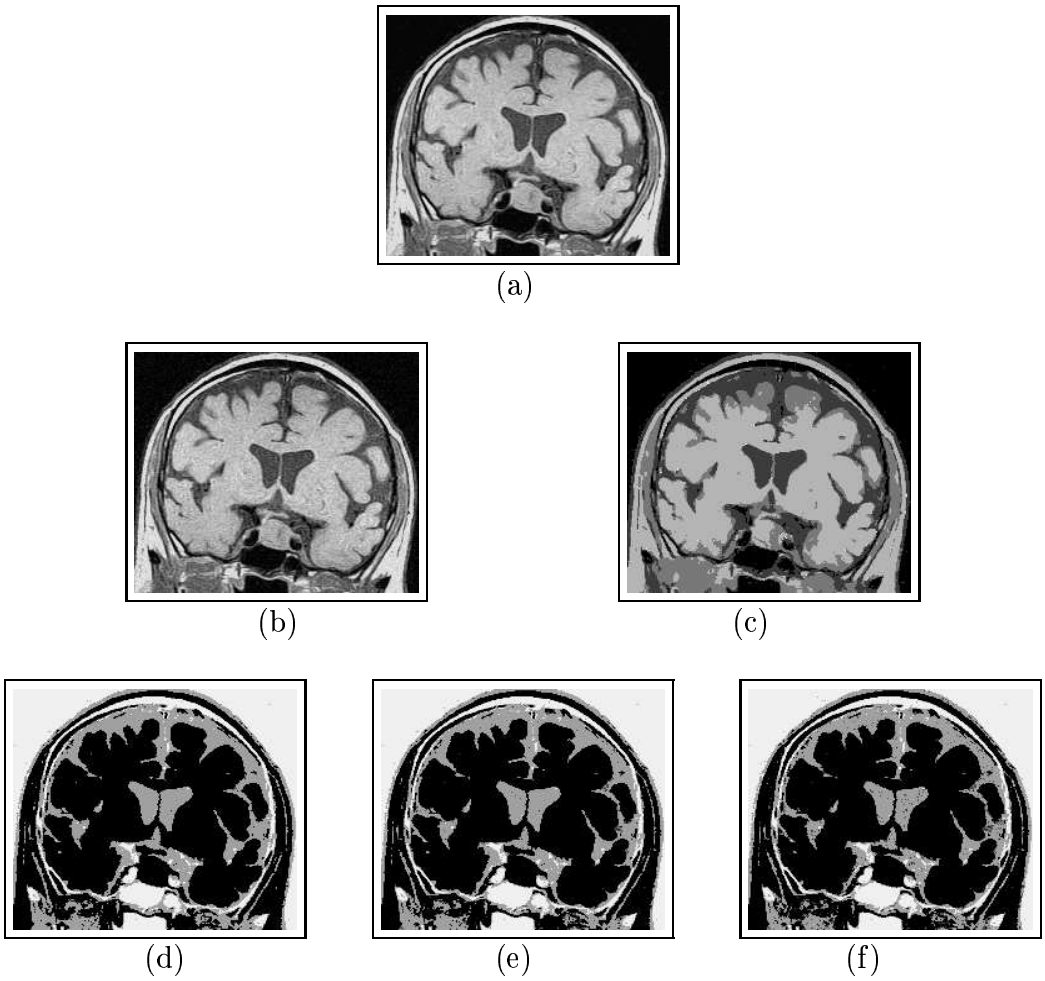

Figure 6.12: *Unsupervised segmentation of brain MR image of size* (227×195)*: (a) original image, (b) noisy image with SNR* $25\,dB$*, (c) segmented image using Zhang's approach; (d),(e) and (f): segmented images using TEM algorithm corresponding to three different initial conditions.*

Class→		1	2	3	4
$\delta = 0.5$	μ_{i1}	4.0	1.5	2	2.0
	σ_{i1}	0.6	0.1	1.0	1.0
	μ_{f1}	3.14	1.38	0.09	3.0
	σ_{f1}	0.08	0.028	0.08	0.34
$\delta = 0.5$	μ_{i2}	4.2	1.45	2.1	1.9
	σ_{i2}	0.65	0.14	1.1	1.2
	μ_{f2}	3.12	1.39	0.09	2.95
	σ_{f2}	0.09	0.027	0.08	0.34
$\delta = 0.5$	μ_{i3}	3.8	1.6	2.2	2.1
	σ_{i3}	0.55	0.12	1.3	1.1
	μ_{f3}	3.13	1.37	0.09	2.9
	σ_{f3}	0.09	0.028	0.08	0.34

Table 6.10: *Image model parameters of TEM algorithm for brain MR image of size* (227×195) *with SNR* $25dB$ *correspond to three different initial conditions.*

Class →		1	2	3	4
$SNR = 25dB$	μ_{i1}	0.96	2.13	2.8	0.1
$\delta = 0.2$	σ_{i1}	0.57	0.55	0.6	1.5
	μ_{f1}	1.2	2.067	3.077	3.65
	σ_{f1}	0.126	0.2	0.89	0.57

Table 6.11: *Parameters for brain MR image of size* (227×195) *with SNR* $25dB$ *using Zhang's approach.*

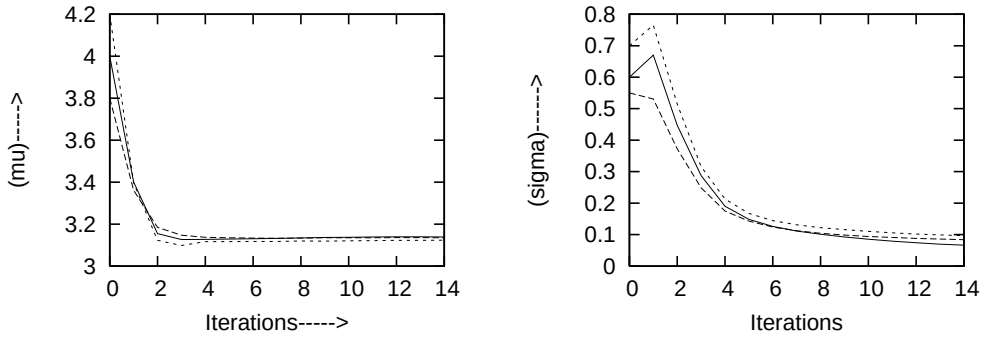

(a) μ plot for class-1 **(b)** σ plot for class-1

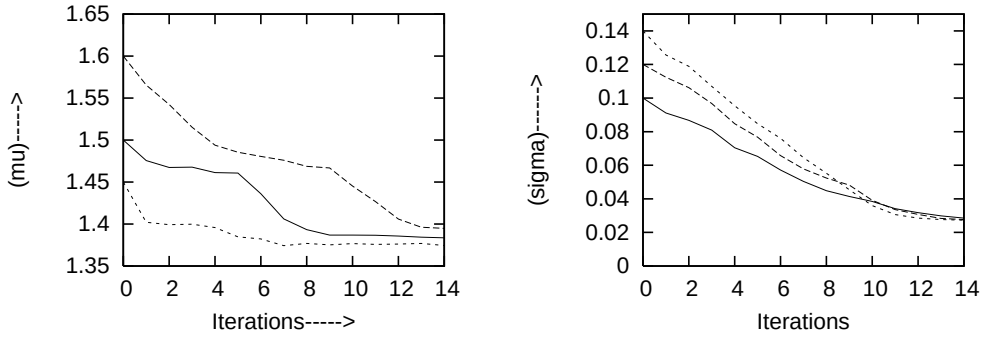

(c) μ plot for class-2 **(d)** σ plot for class-2

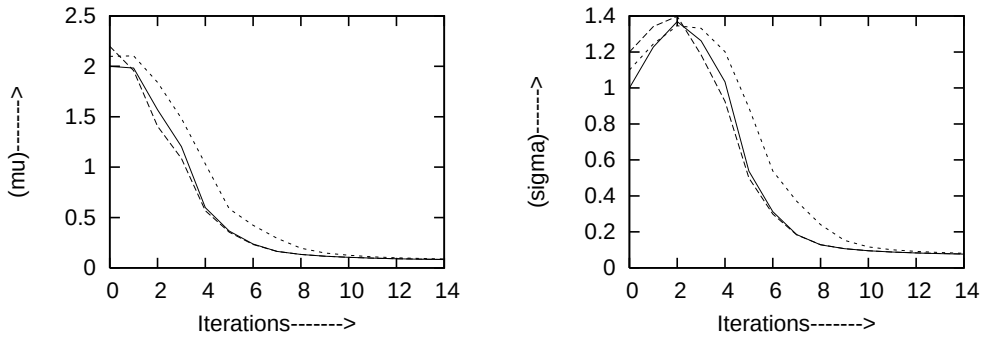

(e) μ plot for class-3 **(f)** σ plot for class-3

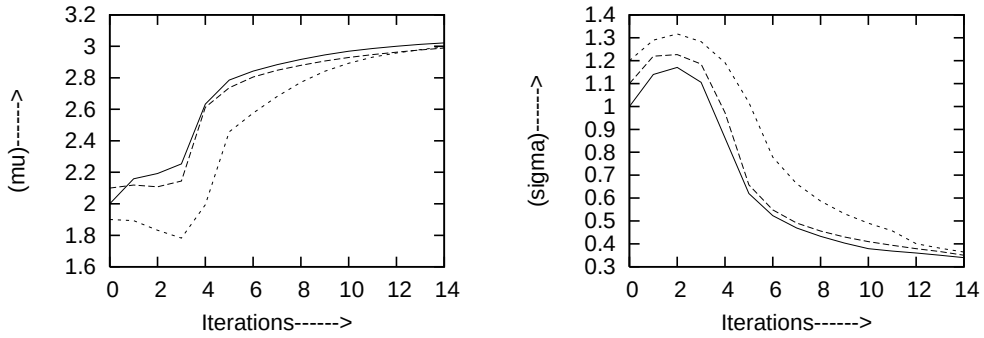

(g) μ plot for class-4 **(h)** σ plot for class-4

Figure 6.13: *Convergence of image model parameters of TEM algorithm corresponding to Table 6.10.*

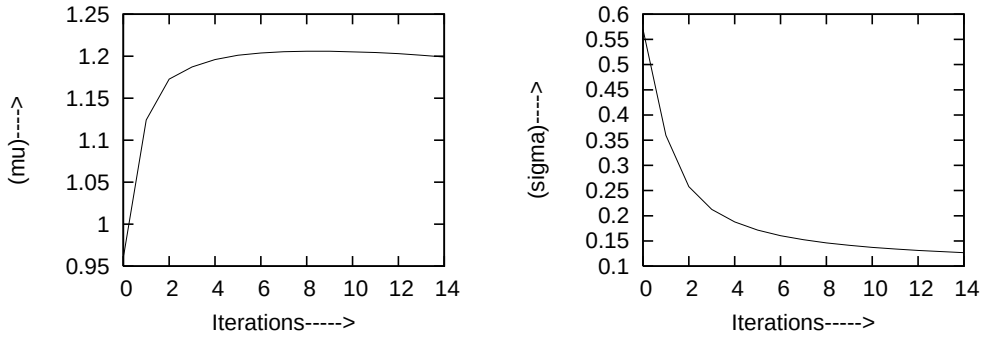
(mu)---->
Iterations----->
(sigma)---->
Iterations----->
(mu)---->
Iterations----->
(sigma)---->
Iterations----->
(mu)---->
Iterations----->
(sigma)---->
Iterations----->

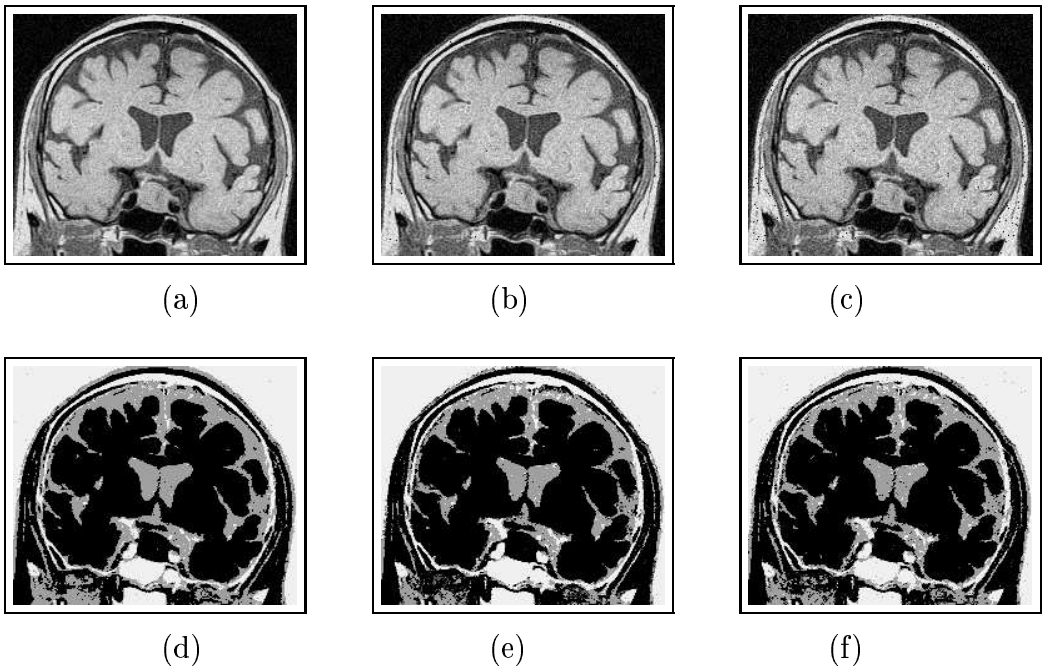

Figure 6.15: *Unsupervised segmentation of brain MR image of size* (227×195) *using TEM algorithm: (a),(b)and (c): noisy images with SNR* $22dB$, $20dB$, $18dB$ *respectively; (d),(e) and (f): corresponding segmented images respectively.*

Class		1	2	3	4
SNR	μ_i	4.0	1.5	2.0	2.0
22dB	σ_i	0.7	0.1	1.0	1.0
	μ_f	3.2	1.442	0.1	3.051
$\delta = 0.5$	σ_f	0.084	0.015	0.104	0.32
SNR	μ_i	4.0	1.5	2.0	2.0
20dB	σ_i	0.65	0.1	1.0	1.0
	μ_f	3.32	1.488	0.09	3.02
$\delta = 0.5$	σ_f	0.082	0.028	0.102	0.312
SNR	μ_i	4.0	1.5	2.0	2.0
18dB	σ_i	0.65	0.1	1.0	1.0
	μ_f	3.41	1.425	0.09	3.02
$\delta = 0.5$	σ_f	0.089	0.03	0.099	0.32

Table 6.12: *Image model parameters of TEM algorithm for brain MR image of size* (227×195) *with SNR of* $22dB$, $20dB$ *and* $18dB$ *respectively as shown in Figure 6.15*

Class→		1	2	3	4
$\delta = 0.5$	μ_{i1}	0.5	4.0	2.5	2.0
	σ_{i1}	0.5	0.5	0.5	2.0
	μ_{f1}	0.07	2.85	1.52	1.21
	σ_{f1}	0.034	0.535	0.4	0.19
$\delta = 0.5$	μ_{i2}	0.45	4.2	2.2	1.9
	σ_{i2}	0.45	0.45	0.45	1.7
	μ_{f2}	0.07	2.87	1.5	1.25
	σ_{f2}	0.04	0.53	0.22	0.21
$\delta = 0.5$	μ_{i3}	0.51	3.8	2.4	1.8
	σ_{i3}	0.52	0.4	0.47	2.2
	μ_{f3}	0.07	2.89	1.52	1.26
	σ_{f3}	0.038	0.52	0.22	0.22

Table 6.13: *Image model parameters of TEM algorithm for brain MR image of size* (189×205) *with SNR* $25dB$ *correspond to three different initial conditions.*

Class →		1	2	3	4
$SNR = 25dB$	μ_{i1}	0.013	1.433	2.883	2.00
$\delta = 0.2$	σ_{i1}	0.32	0.607	0.668	0.5
	μ_{f1}	0.0	1.422	3.115	2.475
	σ_{f1}	0.0001	0.12	0.198	0.054

Table 6.14: *Image model parameters for brain MR image of size* (189×205) *with SNR=*$25dB$ *using Zhang's approach.*

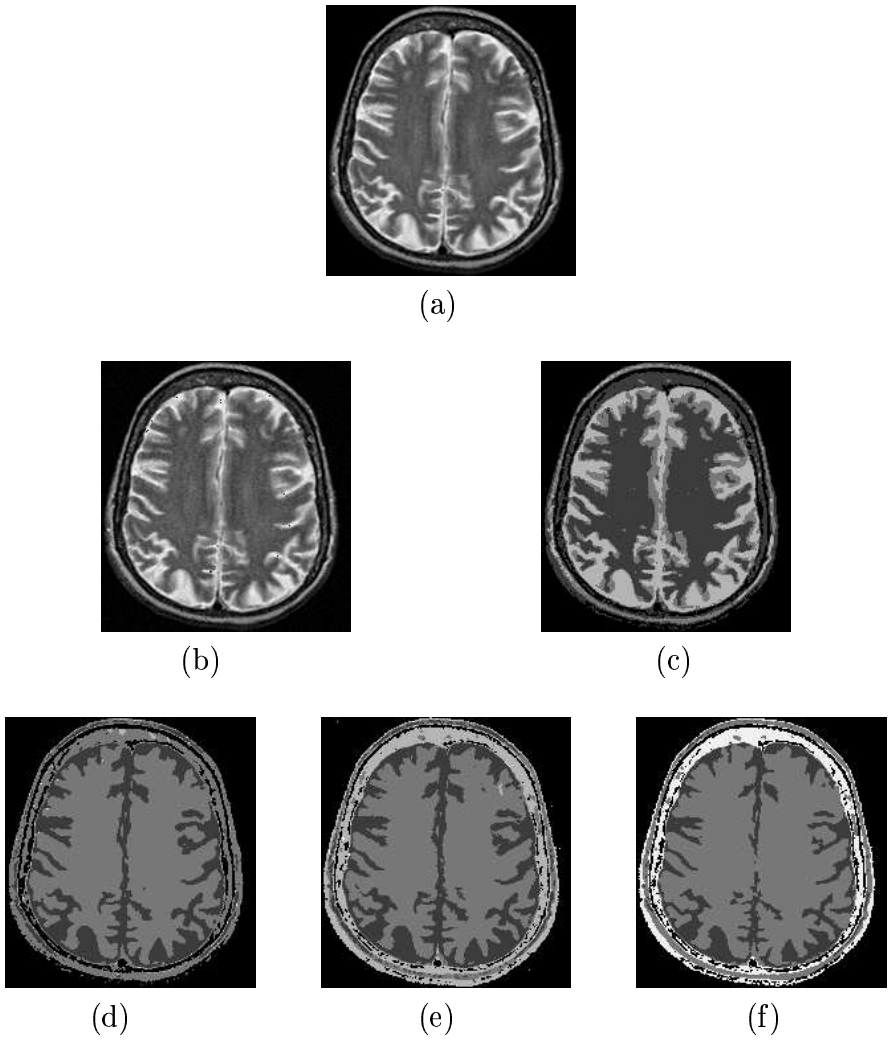

Figure 6.16: *Unsupervised segmentation of brain MR image of size* (189×205)*: (a) original image, (b) noisy image with SNR* $25\,dB$*, (c) segmented image using Zhang's approach; (d),(e) and (f) : segmented images using TEM algorithm corresponding to three different initial conditions.*

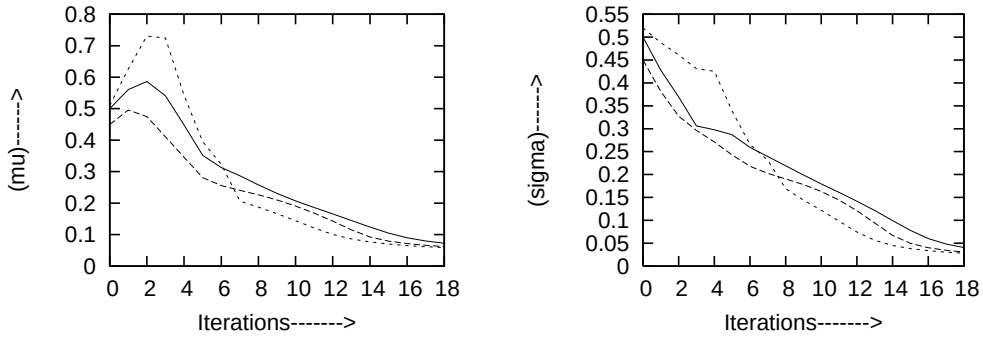

(a) μ plot for class-1

(b) σ plot for class-1

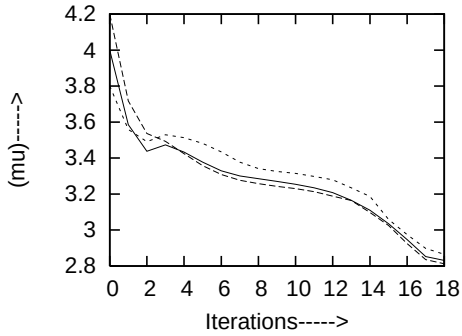

(c) μ plot for class-2

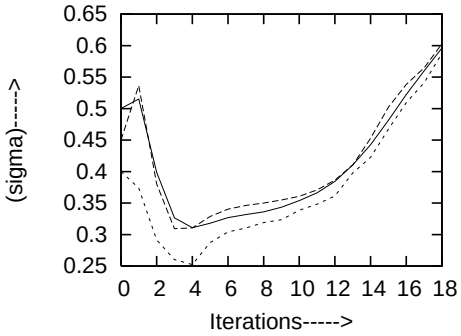

(d) σ plot for class-2

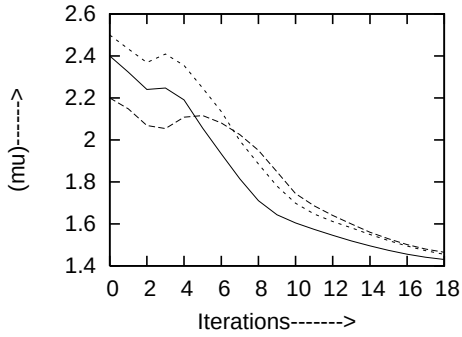

(e) μ plot for class-3

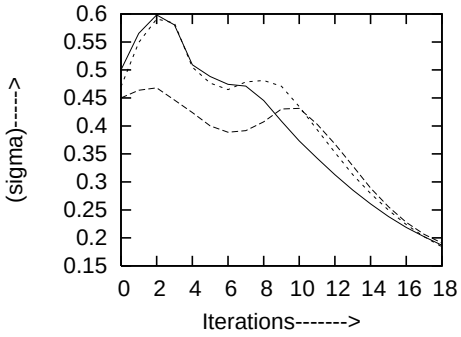

(f) σ plot for class-3

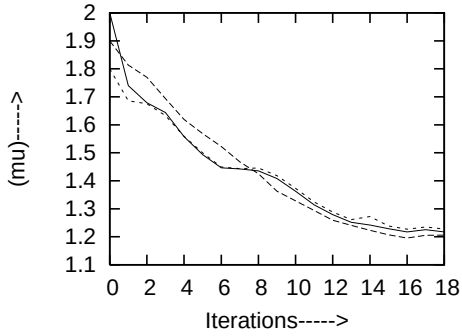

(g) μ plot for class-4

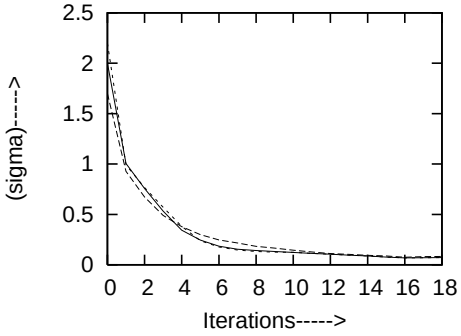

(h) σ plot for class-4

Figure 6.17: *Convergence of image model parameters of TEM algorithm corresponding to Table 6.13.*

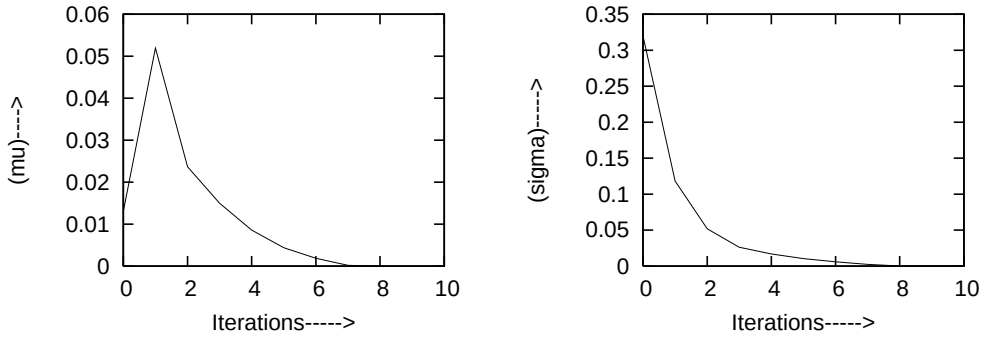

(a) μ plot for class-1

(b) σ plot for class-1

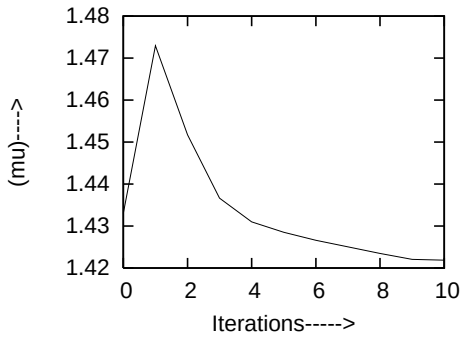

(c) μ plot for class-2

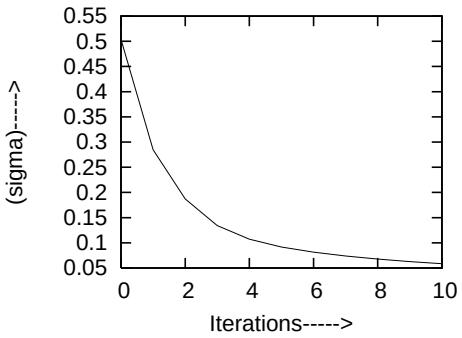

(d) σ plot for class-2

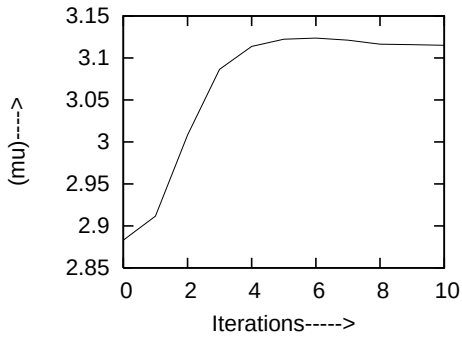

(e) μ plot for class-3

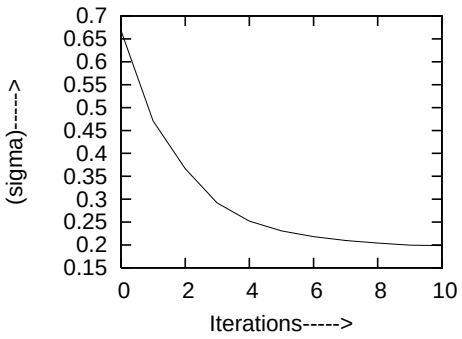

(f) σ plot for class-3

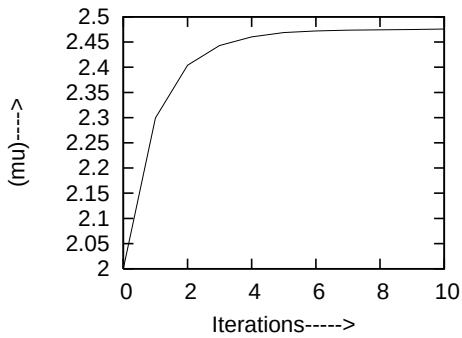

(g) μ plot for class-4

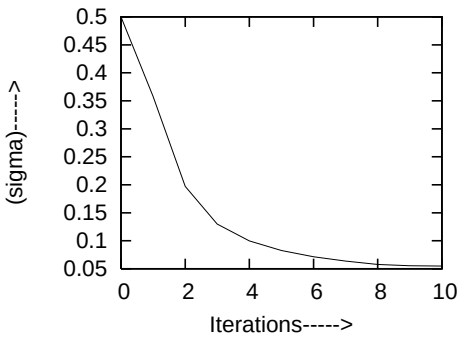

(h) σ plot for class-4

Figure 6.18: *Convergence of image model parameters of brain MR image of size* (189×205) *corresponding to Table 6.14.*

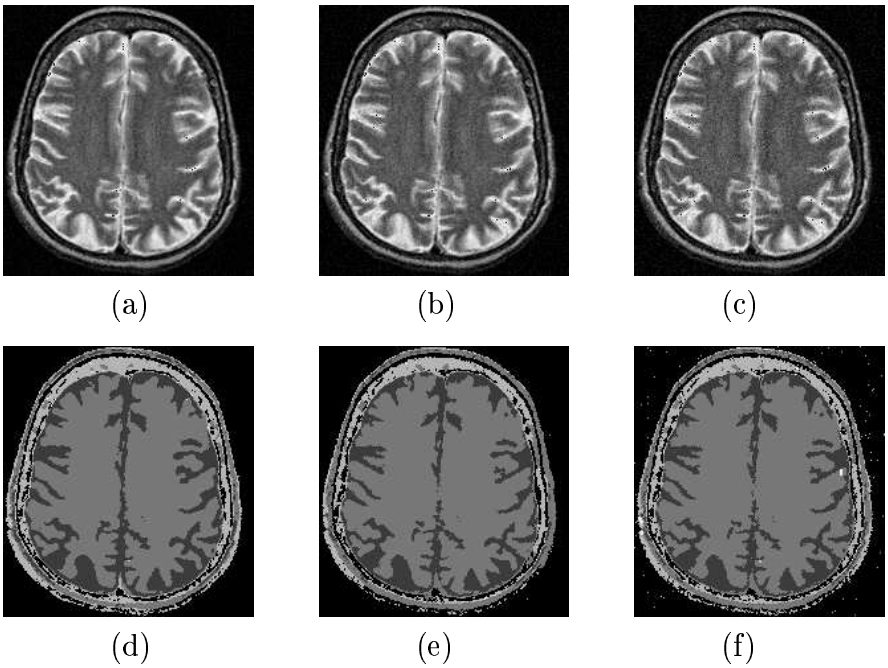

Figure 6.19: *Unsupervised segmentation of brain MR image of size* (189×205) *using TEM algorithm: (a),(b)and (c): noisy images with SNR* $22dB$, $20dB$, $18dB$ *respectively; (d),(e) and (f): corresponding segmented images respectively.*

Class		1	2	3	4
SNR	μ_i	0.5	4.0	2.4	2.0
22dB	σ_i	0.5	0.5	0.5	2.0
	μ_f	0.081	2.751	1.445	0.60
$\delta = 0.5$	σ_f	0.04	0.602	0.188	0.26
SNR	μ_i	0.5	4.0	2.4	2.0
20dB	σ_i	0.5	0.5	0.5	2.0
	μ_f	0.096	2.794	1.455	0.59
$\delta = 0.5$	σ_f	0.046	0.584	0.212	0.251
SNR	μ_i	0.5	4.0	2.4	2.0
18dB	σ_i	0.5	0.5	0.5	2.0
	μ_f	0.124	3.0	1.497	0.652
$\delta = 0.5$	σ_f	0.058	0.524	0.256	0.248

Table 6.15: *Image model parameters of TEM algorithm for brain MR Image of size* (189×205) *with SNR of* $22dB$, $20dB$ *and* $18dB$ *respectively.*

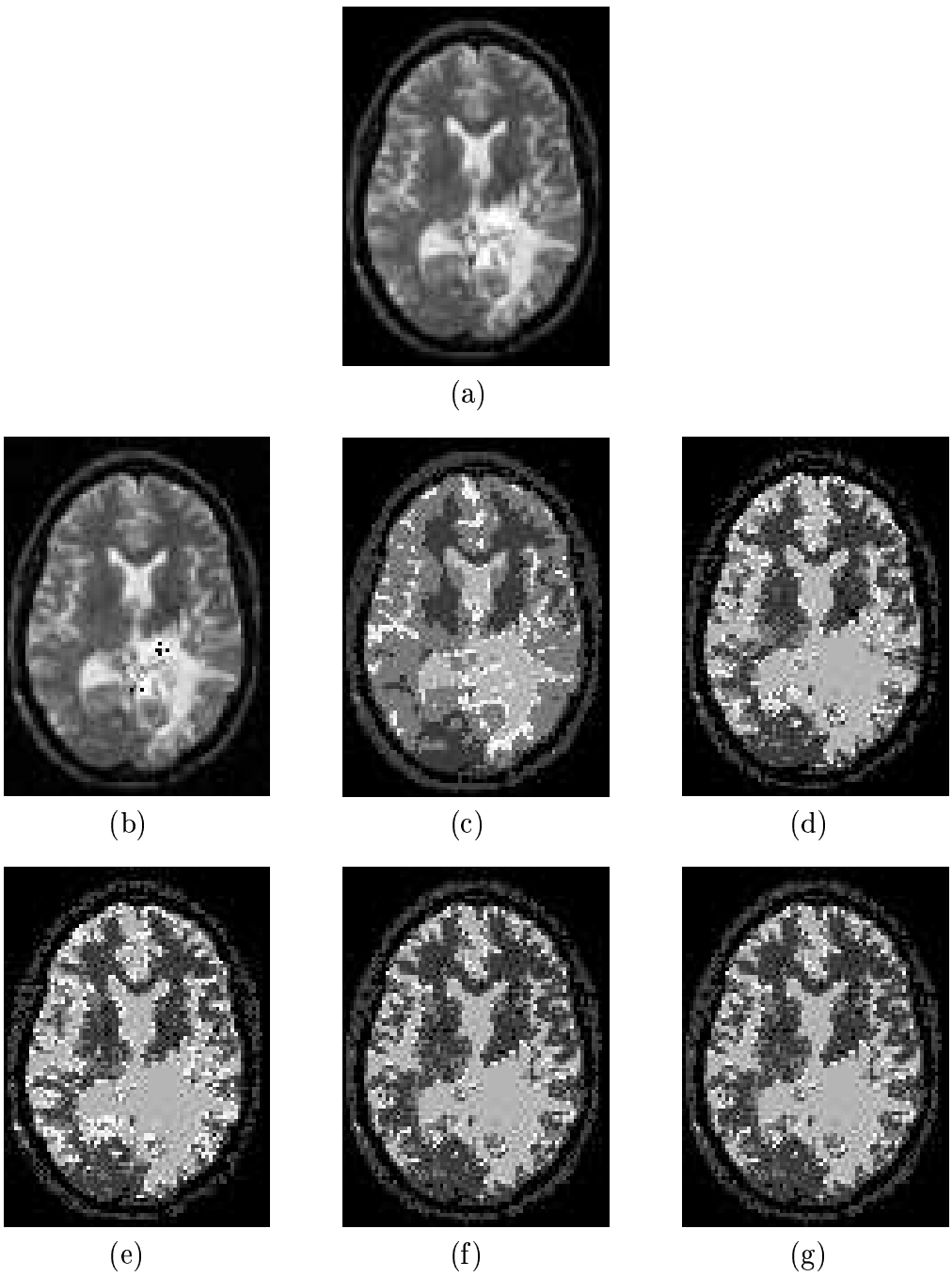

Figure 6.20: *Unsupervised segmentation of brain MR image of size* (74×100)*: (a) original image, (b) noisy image with SNR* $25\,dB$*, (c) segmented image using Zhang's approach, (d),(e),(f) and (g): segmented images using TEM algorithm corresponding to four different initial conditions.*

Class→		1	2	3	4
$\delta = 0.5$	μ_{i1}	0.5	1.1	1.8	2.5
	σ_{i1}	0.6	0.185	0.108	0.143
	μ_{f1}	0.025	1.389	1.721	2.481
	σ_{f1}	0.038	0.121	0.096	0.133
$\delta = 0.5$	μ_{i2}	.52	1.05	1.8	2.6
	σ_{i2}	0.5	0.18	0.115	0.128
	μ_{f2}	0.022	1.388	1.71	2.5
	σ_{f2}	0.034	0.120	0.09	0.118
$\delta = 0.5$	μ_{i3}	0.54	1.15	1.82	2.55
	σ_{i3}	0.61	0.19	0.114	0.16
	μ_{f3}	0.027	1.389	1.75	2.47
	σ_{f3}	0.04	0.121	0.0915	0.148
$\delta = 0.5$	μ_{i4}	0.46	1.17	1.78	2.65
	σ_{i4}	0.5	0.12	0.13	0.2
	μ_{f4}	0.026	1.39	1.685	2.48
	σ_{f4}	0.038	0.121	0.094	0.151

Table 6.16: *Image model parameters of TEM algorithm for brain MR image of size* (74×100) *with SNR=*$25dB$ *for four different initial conditions.*

Class→		1	2	3	4
$\delta = 0.5$	μ_{i1}	0.025	1.24	1.7	3.36
	σ_{i1}	0.046	0.21	0.215	0.308
	μ_{f1}	0.0	1.264	1.708	3.56
	σ_{f1}	0.0011	0.07	0.119	0.14

Table 6.17: *Image model parameters of brain MR image of size* (74×100) *with SNR=*$25dB$ *using Zhang's approach.*

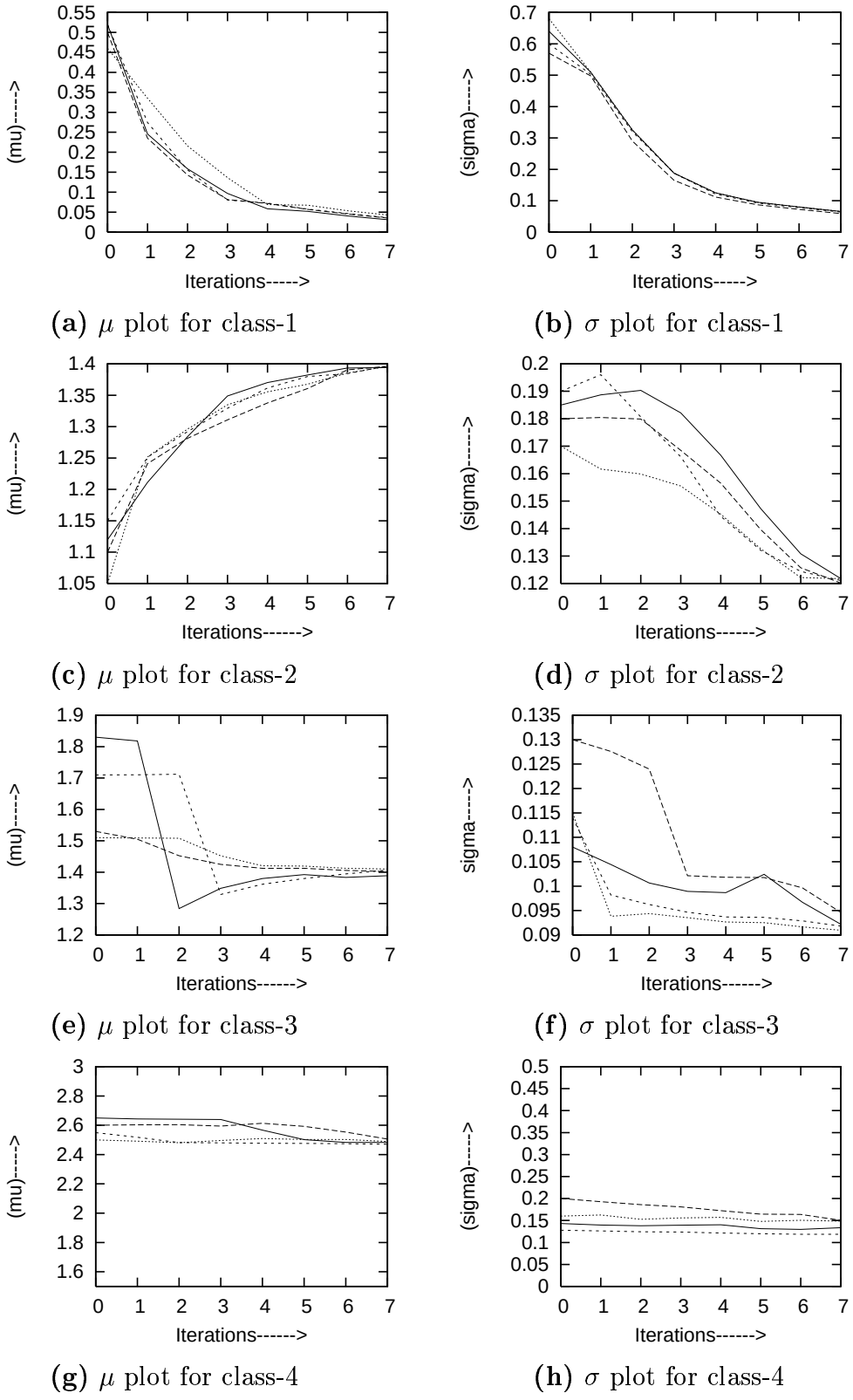

(a) μ plot for class-1 **(b)** σ plot for class-1

(c) μ plot for class-2 **(d)** σ plot for class-2

(e) μ plot for class-3 **(f)** σ plot for class-3

(g) μ plot for class-4 **(h)** σ plot for class-4

Figure 6.21: *Convergence of model parameters of TEM algorithm of brain MR image corresponding to Table 6.16.*

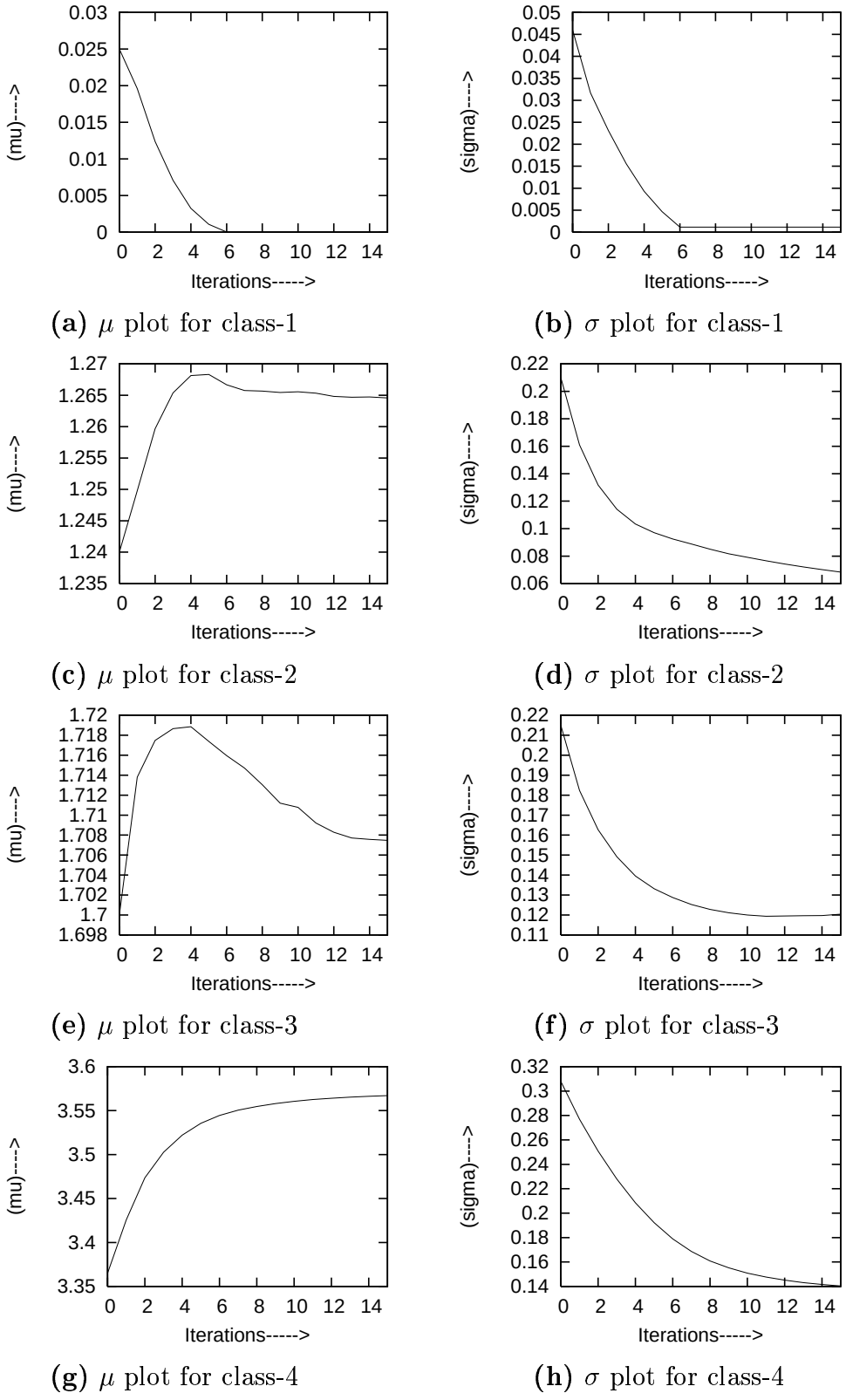

Figure 6.22: *Convergence of image model parameters of brain MR image using Zhang's approach corresponding to Table 6.17*

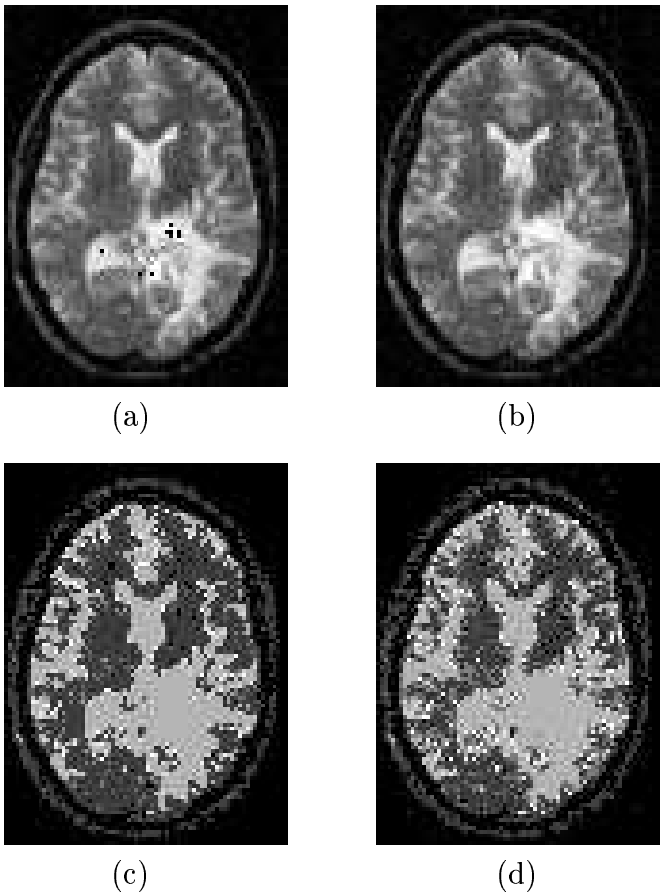

Figure 6.23: *Unsupervised segmentation of brain MR image of size* (74×100) *using TEM algorithm: (a) and (b): noisy images with SNR* $22dB$, $20dB$ *respectively; (c) and (d): corresponding segmented images respectively.*

Class		1	2	3	4
SNR	μ_i	0.5	1.3	1.63	2.54
22dB	σ_i	0.55	0.16	0.03	0.13
	μ_f	0.032	1.368	1.593	2.43
$\delta = 0.5$	σ_f	0.049	0.128	0.012	0.1155
SNR	μ_i	0.5	1.2	1.93	2.53
20dB	σ_i	0.6	0.16	0.01	0.113
	μ_f	0.031	1.33	1.754	2.455
$\delta = 0.5$	σ_f	0.05	0.134	0.077	0.092

Table 6.18: *Image model parameters of TEM algorithm for brain MR image of size* (74×100) *having SNR of* $22dB$, $20dB$ *respectively.*

Chapter 7

Supervised Image Segmentation using MRF model and Homotopy Continuation method

7.1 Introduction

In this chapter, a new concept of image segmentation using MRF model learning feature is introduced. It is assumed that the observed image is derived from a set, known as *class of images*. Out of this given image class, one image is selected and used as the training data for the MRF model learning. The MRF model learns this preselected image. The learning is viewed as estimation of MRF model parameters as it is assumed to have the knowledge of the structure of the model. The problem is formulated using Conditional Pseudo Likelihood(CPL) approach and the parameters are estimated using homotopy continuation method [120, 121]. Once the model learns one image, the same model is used as the image model for all the images of a class from which the training image is derived. This model is used to obtain the MAP estimate of the class labels using proposed hybrid Tabu and parallel hybrid Tabu algorithms. The performance of these algorithms are compared with that of the Simulated Annealing algorithm. This learning feature avoids the parameter estimation of each and every individual image of a class of images.

7.2 Image Model

Let X denotes the label process associated with the true but unknown labels and x be a realization of the same. The label process is modeled as MRF. Y denotes the observed random field corresponding to observed degraded image. We consider the

following degradation model

$$Y_{i,j} = X_{i,j} + W_{i,j}, \quad \forall\,(i,j) \in (N \times N) \tag{7.1}$$

which with a lexicographical ordering will be $Y = X + W$. In the above model X is assumed to be a Markov random field with respect to a neighborhood system $\eta = \{\eta_{i,j}; (i,j) \in L\}$ and is described in terms of its local characteristics

$$\begin{aligned} P[X_{i,j} = x_{i,j} \mid X_{k,l} = x_{k,l}, (k,l) \in L, (k,l) \neq (i,j)] \\ = P[X_{i,j} = x_{i,j} \mid X_{k,l} = x_{k,l}, (k,l) \in \eta_{i,j}] \end{aligned}$$

Since X is assumed to be MRF, the equivalent joint distribution is the Gibbs distribution which can be expressed as

$$P(X = x) = \frac{1}{Z} e^{-U(x)} \tag{7.2}$$

The model in (7.2) is the a priori distribution of the random field X. Z is the partition function as defined in Chapter 3. The exponent term $U(x)$ is called the energy function and is of the form $U(x) = \sum_{c \in C} V_c(x)$ with $V_c(x)$ denoting the clique potential associated with clique c. We make the following assumptions for the above model given by (7.1).

1. $W_{i,j}$ is a white Gaussian sequence with zero mean and variance σ^2 (σ unknown).

2. $W_{i,j}$ is statistically independent of $X_{k,l}$, for all (i,j) and (k,l) belonging to (L).

3. $x_{i,j}$ takes any gray level value from the set $G = (1, \ldots, G_m)$, typically $G_m = 2$ for binary and 256 for gray scaled images.

The parameter vector set for the *a posteriori* model is $\theta = [\alpha, \beta, \sigma^2]^T$.

7.3 Problem statement

Here we assume to have *a priori* knowledge of the number of classes. We also assume to have *a priori* knowledge of noise variance of the noisy image. The goal is to obtain the optimal estimate of the class label x^* based on the noisy random field realization y and hence achieve proper segmentation. This label estimation is formulated using MAP criterion. The following optimality criterion is adopted.

$$\hat{x} = arg \max_{x} P(X = x \mid Y = y, \hat{\theta}) \tag{7.3}$$

where $\hat{\theta}$ denotes the estimates of the parameter vector. The problem of determining $\hat{\theta}$, is referred to as the learning of the model for a class to which the given realization x belongs. Estimates of the model parameters are obtained using the notion of Maximum Conditional Pseudo Likelihood(MCPL) principle and homotopy continuation algorithm. In the learning phase we attempt to estimate the noise model parameter σ together with the image model parameters. Hence, we consider a zero mean white Gaussian noise process to generate a noisy image of prespecified SNR. The noisy image and the original image are used to estimate the image model and noise model parameters. Correct estimate of the noise model parameters corroborates the estimates of the model parameters. But, in the model validation phase we only use the image model parameters to model each and every image of the image class from which the training image is derived. We consider the following optimality criterion.

$$\hat{\theta} = arg \max_{\theta} P(X = x \mid Y = y, \theta) \tag{7.4}$$

Having determined $\hat{\theta}$, we use it in the MAP estimation problem of (7.3) for estimating the image labels and thus segment the image.

7.4 Homotopy concept and the approach

We begin by defining homotopy.

Definition: *Let X, Y be two topological spaces and I be the unit interval $\{\lambda \mid 0 \leq \lambda \leq 1\}$. The two maps $f, g : X \rightarrow Y$ are called homotopic if there exists a continuous map $h : X \times I \rightarrow Y$ such that $h(x,1) = f(x)$ and $h(x,0) = g(x)$ for each $x \in X$.*

In the above definition h represents a continuous deformation of the map g to f as the parameter λ is varied from 0 to 1. In this thesis, we use $f : \Re^n \longrightarrow \Re^n$, $g : \Re^n \longrightarrow \Re^n$ and $x \in \Re^n$. Therefore, from the definition of homotopy it is clear that $h : \Re^{n+1} \longrightarrow \Re^n$. Furthermore, $f(.) = [f_1(.), f_2(.), \cdots, f_n(.)]^T$, $h(.,.) = [h_1(.,.), h_2(.,.), \cdots, h_n(.,.)]^T$ and $x = [x_1, x_2, \cdots, x_n]^T$, where, n depends upon the number of unknowns.

Application of the concept of homotopy continuation for determining the fixed points or zeros of a function is well addressed in literature [91]. In a wide variety of engineering problems where the conventional procedures like Newton algorithms are inadequate, while continuation methods yield accurate solutions. Suppose, it is required to find a zero of the function $f(x)$, where, $f : \Re^n \longrightarrow \Re^n$. In homotopy continuation approach, the procedure for determining zero of $f(x)$ is to start from the zero of a trivial function, for example, $x - q$, where, q is known. It is easy

to see from the definition of homotopy that $(x-q)$ is homotopic to $f(x)$ (choose $h(x,\lambda) = \lambda f(x) + (1-\lambda)(x-q)$). Therefore, $(x-q)$ can be deformed continuously by a homotopy function h till the desired function $f(x)$ is reached at $\lambda = 1$. The idea is to solve a series of problems as λ is slowly varied using a locally convergent iterative technique. Essentially the problem boils down to tracing the zero curve of the homotopy function h, when the homotopy parameter λ is varied from 0 to 1. This approach is briefly outlined as follows.

1. Start with a trivial system $g(x)$ that is specially chosen to have an obvious solution, for example, $g(x) = (x-q)$, where, q is known.

2. Set up a system of equations $h(x,\lambda) = 0$ with an additional variable λ that yields $g(x)$ at $\lambda = 0$ and $f(x)$ at $\lambda = 1$. For example, take $h(x,\lambda) = \lambda f(x) + (1-\lambda)(x-q)$.

3. Follow the zero path of $h(x,\lambda)$ from $\lambda = 0$ to $\lambda = 1$.

Since Jacobian of the homotopy function will be used frequently, we state them before using it in various places. For a homotopy function $h(x,\lambda) : \Re^{n+1} \longrightarrow \Re^n$, its Jacobian $Jh(x,\lambda)$ is an $n \times (n+1)$ matrix which can be expressed as

$$Jh(x,\lambda) = \begin{bmatrix} \frac{\partial h_1}{\partial x_1} & \cdots & \frac{\partial h_1}{\partial x_n} & \frac{\partial h_1}{\partial \lambda} \\ \vdots & \cdots & \vdots & \vdots \\ \frac{\partial h_n}{\partial x_1} & \cdots & \frac{\partial h_n}{\partial x_n} & \frac{\partial h_1}{\partial \lambda} \end{bmatrix}$$

Let $Jh_x(x,\lambda)$ be the $n \times n$ matrix consisting of the first n columns of $Jh(x,\lambda)$. So $Jh_x(x,\lambda)$ can be written as

$$Jh_x(x,\lambda) = \begin{bmatrix} \frac{\partial h_1}{\partial x_1} & \cdots & \frac{\partial h_1}{\partial x_{n-1}} & \frac{\partial h_1}{\partial x_n} \\ \vdots & \cdots & \vdots & \vdots \\ \frac{\partial h_n}{\partial x_1} & \cdots & \frac{\partial h_n}{\partial x_{n-1}} & \frac{\partial h_1}{\partial x_n} \end{bmatrix}$$

For any homotopy function $h(q,x,\lambda)$, with $q \in \Re^n$, $x \in \Re^n$, $\lambda \in [0,1]$, the following conditions are to be satisfied for successful tracking of the path to the desired solution [91]. Further, $h(q,x,\lambda)$ should be smooth (twice continuously differentiable).

1. $h(q,x,1) = 0$ is the system we want to solve for x with given q.

2. $h(q,x,0) = 0$ is easy to solve for x (given q).

3. The matrix $Jh_q(q,x,\lambda)$ has rank n, where $Jh_q(q,x,\lambda)$ denotes the Jacobian of $h(q,x,\lambda)$ with respect to x and λ.

4. One of the following condition holds.
   (a) The continuation curves are increasing in λ.
   (b) $h(q, x, 1) = 0$ has a unique solution x for each q.
5. The zero paths of $h(q, x, \lambda)$ are bounded. This should hold good between $\lambda \in [0, 1]$.

7.4.1 Homotopy functions

There is no unique homotopy map that will continuously deform from a trivial map to any map. Depending upon the problem at hand the path has to be accurately tracked and hence, a suitable homotopy function has to be chosen for the existence of a path leading to the solution. The commonly used maps are as follows.

Linear homotopy

This homotopy function is a linear combination of the two function f and g.

$$h(x, \lambda) = \lambda f(x) + (1 - \lambda)g(x) \tag{7.5}$$

This is quite useful when one could find a function g of the same degree as f with known solutions. Nevertheless, often it is cumbersome to select such a function.

Newton homotopy

This is defined as follows:

$$h(x, \lambda) = f(x) - (1 - \lambda)f(x^0) \tag{7.6}$$

where x^0 denotes an arbitrary point. Having selected x^0 one could compute $f(x^0)$ and then at $\lambda = 0$ the trivial function $g(x) = f(x) - f(x^0)$. Here, the function $g(x)$, by construction, has the solution x^0. Therefore, Newton homotopy offers the advantage of an arbitrary starting point.

Fixed point homotopy

The fixed point homotopy map also allows to choose the initial solution arbitrarily. This is given as,

$$h(x, \lambda) = \lambda f(x) + (1 - \lambda)(x - x^0). \tag{7.7}$$

Here again, the trivial map $g(x) = x - x^0$ and the trivial solution is x^0 thus permitting to choose the initial solution at random.

7.5 Model Learning

The objective here is to learn the image model. We choose initial image model parameters arbitrarily. Then MAP estimate criterion is used to estimate X from Y. Using the estimated image X and the degraded image Y we estimate the image model parameters. This process is repeated until some stopping criterion is met. This scheme can be viewed as unsupervised model learning scheme. In the following, we develop a parameter estimation technique which is used at each step of the above mentioned learning scheme. Moreover, we assume that the structure of the probability distributions of image model is known. But the parameters are assumed to be unknown. Thus, the problem is to estimate the model parameter vector θ using the estimated image X and the observed image Y. Towards this end, we try to maximize the posterior probability distribution $P(X = x \mid Y = y, \theta)$ with respect to θ to find the optimal estimate of θ. In other words, we consider the following optimality criterion.

$$\theta^* = arg \max_{\theta} P(X = x \mid Y = y, \theta) \tag{7.8}$$

Using Bayes rule the conditional probability can be written as

$$P(X = x \mid Y = y, \theta) = \frac{P(Y = y \mid X = x, \theta)P(X = x \mid \theta)}{P(Y = y \mid \theta)} \tag{7.9}$$

Making use of the assumptions described in Section (7.3), the term $P(Y = y \mid X = x, \theta)$ in (7.9) can be written as

$$\begin{aligned} P(Y = y \mid X = x, \theta) &= P(X + W = y \mid X = x, \theta) \\ &= P(W = y - x \mid X = x, \theta) \end{aligned} \tag{7.10}$$

Since, W is assumed to be white Gaussian, (7.10) can be written as

$$P(Y = y \mid \theta, X = x) = \frac{1}{(2\pi\sigma^2)^{N^2/2}} exp\left\{\frac{-\|y - x\|^2}{2\sigma^2}\right\} \tag{7.11}$$

Now, $P(Y = y \mid \theta)$ in (7.9) is not a constant. By definition, the marginal conditional probability is given by,

$$\begin{aligned} P(Y = y \mid \theta) &= \sum_{\xi} P(X = \xi, Y = y \mid \theta) \\ &= \sum_{\xi} P(Y = y \mid X = \xi, \theta)P(X = \xi \mid \theta). \end{aligned} \tag{7.12}$$

Where, ξ ranges over all realizations of X. Substituting (7.11) in the above expression and using the fact that X is a MRF, (7.12) can be expressed as,

$$P(Y = y \mid \theta) = \sum_{\xi} \frac{1}{(2\pi\sigma^2)^{N^2/2}} e^{\frac{-\|y-\xi\|^2}{2\sigma^2}} \frac{1}{Z} e^{-U(\xi,\phi)}. \tag{7.13}$$

which implies,

$$P(X = x \mid Y = y, \theta) = \frac{e^{\frac{-\|y-x\|^2}{2\sigma^2}} e^{-U(x,\phi)}}{\sum_{\xi} e^{\frac{-\|y-\xi\|^2}{2\sigma^2}} e^{-U(\xi,\phi)}}. \tag{7.14}$$

In (7.14) the summation is over all possible realizations of X; for example $(256)^{(256)^2}$ realizations for a (256×256) image with each pixel having 256 gray levels. Thus, from a computational standpoint, handling (7.14) would be practically impossible. One can view (7.14) as a conditional likelihood (CL) function to be maximized for estimating θ. To overcome the computational problem, we approximate (7.14) using the conditional pseudo likelihood (CPL) function.

$$\begin{aligned} P(X = x \mid Y = y, \theta) \;&\approx\; \prod_{i,j} P(X_{i,j} = x_{i,j} \mid X_{m,n} = x_{m,n},\ \ (m,n) \in \eta, Y = y, \theta) \\ &\triangleq \hat{P}(X = x \mid Y = y, \theta) \end{aligned} \tag{7.15}$$

This is the conditional pseudo likelihood function, where we are approximating the posterior probability distribution instead of the *a priori* probability distribution. We maximize (7.15) to obtain the maximum conditional pseudo likelihood (MCPL) estimate of the parameter vector θ.

$$\hat{P}(X = x \mid Y = y, \theta) = \prod_{(i,j)\in L} \left[\frac{exp(\frac{-(y_{i,j}-x_{i,j})^2}{2\sigma^2}) exp(-\sum_{c\in C} V_c(x,\phi))}{\sum_{x_{i,j}\in G} \left\{ exp(\frac{-(y_{i,j}-x_{i,j})^2}{2\sigma^2}) exp(-\sum_{c\in C} V_c(x,\phi)) \right\}} \right] \tag{7.16}$$

In (7.16) the summation is only over the all possible G gray levels of the pixel $x_{i,j}$. This would involve 256 terms in the summation for a 256 gray level image. A significant reduction as compared to (7.14) ; thus making (7.16) a computationally feasible expression. Now the parameter estimation problem is recast as

$$\theta^* = arg \quad \max_{\theta} \hat{P}(X = x \mid Y = y, \theta) \tag{7.17}$$

7.5.1 Parameter Estimation Using Homotopy Continuation Method

It is clear from previous section that the parameter estimation problem has been reduced to maximization of (7.16) with respect to θ. Towards this end let

$$f(\theta) = \frac{\partial}{\partial \theta} \left\{ \log \left[\hat{P}(X = x^{k+1} \mid Y = y, \theta) \right] \right\} \tag{7.18}$$

Now the homotopy method is employed to solve $f(\theta) = 0$, where θ is the unknown parameter vector to be determined. The following weak membrane is used as *a priori* energy function.

$$\begin{aligned} U(x, \phi) = \sum_{i,j} \alpha \Big\{ (x_{i,j} - x_{i,j-1})^2 + (x_{i,j} - x_{i,j+1})^2 + (x_{i,j} - x_{i-1,j})^2 \\ + ((x_{i,j} - x_{i+1,j})^2 \Big\} + \beta \left\{ h_{i,j} + v_{i,j} \right\} \end{aligned} \tag{7.19}$$

and the corresponding *a posteriori* energy function is expressed as

$$\begin{aligned} U_p(x) \;=\; & \sum_{ij} \frac{(y_{ij} - x_{ij})^2}{2\sigma^2} \\ & + \alpha \left\{ (x_{ij} - x_{i-1,j})^2 + (x_{ij} - x_{i,j-1})^2 + (x_{ij} - x_{i+1,j})^2 + (x_{ij} - x_{i,j+1})^2 \right\} \\ & + \beta \left(h_{ij} + v_{ij} \right) \end{aligned} \tag{7.20}$$

Using the above energy functions and carrying out the maximization process, we land up in the following three nonlinear equations that need to be solved.

$$f_1(\theta) = \sum_{i,j} \{ (x_{i,j} - x_{i,j-1})^2 (1 - h_{i,j}) + (x_{i,j} - x_{i-1,j})^2 (1 - v_{i,j}) \} -$$

$$\frac{\sum_{x_{i,j} \in G} \{ (x_{i,j} - x_{i,j-1})^2 (1 - h_{i,j}) + (x_{i,j} - x_{i-1,j})^2 (1 - v_{i,j}) \} exp(-U_p(x, \phi, h, v))}{\sum_{x_{i,j} \in G} exp(-U_p(x, \phi, h, v))} = 0$$

$$f_2(\theta) = \sum_{i,j} \left[(h_{i,j} + v_{i,j}) - \frac{\sum_{x_{i,j} \in G} (h_{i,j} + v_{i,j}) exp(-U_p(x, \phi, h, v))}{\sum_{x_{i,j} \in G} exp(-U_p(x, \phi, h, v))} \right] = 0$$

$$f_3(\theta) = \sum_{i,j} \left[(y_{i,j} - x_{i,j})^2 - \frac{\sum_{x_{i,j} \in G} (y_{i,j} - x_{i,j})^2 exp(-U_p(x, \phi, h, v))}{\sum_{x_{i,j} \in G} exp(-U_p(x, \phi, h, v))} \right] = 0$$

Since the equations are highly nonlinear and there is no *a priori* knowledge of the solutions are known, the notion of homotopy continuation method is used to obtain the solution. In the continuation method we need to trace the homotopy path from a solution of a known system to that of the desired solution. In this regard, we

have considered the fixed point homotopy map [92] which offers the advantage of arbitrary starting point for the path. This fixed point map is given by

$$h(\theta, \lambda, q) = \lambda f(\theta) + (1 - \lambda)(\theta - q) \tag{7.21}$$

where $0 \leq \lambda \leq 1$ and q is an arbitrary starting point. Here the predictor-corrector method is employed to track the path defined by the homotopy in (7.21). The procedure can be briefly outlined as follows: Let $(\theta^k, \lambda^k, \theta^{k-1})$ be a point that satisfies (7.21). Therefore, the point considered is on the path. Tracking the path involves computing the adjacent point on the path. This is determined in the following way. Increment λ^k by some small value $\triangle\lambda$ thus giving the next point $\lambda^{k+1} = \lambda^k + \triangle\lambda$ and evaluate equation (7.21) at $(\theta^k, \lambda^{k+1}, \theta^{k-1})$. If the value of the map $h(\theta^k, \lambda^{k+1}, \theta^{k-1})$ is not equal to zero, then the point $(\theta^k, \lambda^{k+1}, \theta^{k-1})$ is not on the path. Since $h(\theta^k, \lambda^{k+1}, \theta^{k-1}) \neq 0$, we try to obtain an estimate of θ^k, say $\hat{\theta^k}$ corresponding to λ^{k+1} such that $h(\theta^k, \lambda^{k+1}, \theta^{k-1}) \approx 0$. To achieve this one could use Newton's algorithm, namely,

$$\hat{\theta}^k_{i+1} = \hat{\theta}^k_i - J^{-1}_{\hat{\theta}}[h(\hat{\theta}^k_i, \lambda^{k+1}, \theta^{k-1})] \\ h(\hat{\theta}^k_i, \lambda^{k+1}, \theta^{k-1}) \tag{7.22}$$

Where the superscript i denotes the ith Newton iteration and J^{-1}_θ is the inverse of the Jacobian of h with respect to the coefficient of the parameter vector θ. But if $\hat{\theta^k_0}$ is too far from the value $\hat{\theta^k}$ which makes $h(\hat{\theta^k}, \lambda^{k+1}, \theta^{k-1}) \approx 0$, then (7.22) may not converge. To improve the convergence of (7.22) , we select the initial point as $\hat{\theta^k_0} = \theta^k$. A further improvement in the convergence is obtained by considering

$$\hat{\theta}^k_0 = \theta^k - \triangle\lambda J^{-1}_\theta[h(\theta^k, \lambda^{k+1}, \theta^{k-1})] \\ \frac{\partial h}{\partial \lambda}[h(\theta^k, \lambda^{k+1}, \theta^{k-1})] \tag{7.23}$$

The derivation of (7.23) is analogous to the derivation of Stonick and Alexander [93] for our homotopy map (7.21). Equation (7.23) corresponds to the prediction of the next point by taking a step in the direction of the path's slope. For the fixed point homotopy map considered, (7.23) becomes

$$\begin{aligned} \hat{\theta}^k_0 \;=\; & \theta^k - \triangle\lambda \left\{ \frac{I}{1 - (\lambda^k + \triangle\lambda)} - \right. \\ & \frac{I}{(1 - (\lambda^k + \triangle\lambda))^2} \left[\frac{F^{-1}_\theta(\theta^k)}{(\lambda^k + \triangle\lambda)} + \right. \\ & \left. \left. \frac{I}{1 - (\lambda^k + \triangle\lambda)} \right]^{-1} \right\} \\ & \left\{ f(\theta^k) - (\theta^k - \theta^{k-1}) \right\} \end{aligned} \tag{7.24}$$

where I is the identity matrix. The intermediate steps for arriving at (7.24) is given in [42]. If $\hat{\theta}_0^k$ estimated by (7.23) is not on the path then it is taken as the initial point in the correction step (7.22). Otherwise $\hat{\theta}_0^k$ is considered as the next point on the path. Suppose $|\hat{\theta}_{M+1}^k - \hat{\theta}_M^k| \leq \gamma$ then we set $\hat{\theta}_M^k = \hat{\theta}^k = \theta^{k+1}$.

Homotopy Continuation algorithm

Initialize: ($\theta = \theta^0$ and $\lambda = 0$)

do {

Increment $\lambda^{k+1} = \lambda^k + \Delta\lambda$

Update θ^k to $\hat{\theta}_0^k$

if ($h(\theta_0^k, \lambda^{k+1}) <$ threshold)

$\theta^{k+1} = \theta_0^k$

else

take θ_0^k the initial point

for Newton Algorithm

Update: $\hat{\theta}_i^k$ to $\hat{\theta}_{i+1}^k$

if ($|\theta_{i+1}^k - \theta_i^k| \leq$ threshold)

$\theta^{k+1} = \theta_{i+1}^k$

else go to update:

} (Until $\lambda = 1$).

7.6 Segmentation using Bayesian framework

The problem is formulated as a pixel labeling problem. Let x^* denote the true but unknown labeling configuration and $\hat{x}$ denote the estimate for x^*. x^* is the realization of random field X, which is modeled as MRF. The following optimality criterion is considered,

$$\hat{x} = arg\max_x P(X = x \mid Y = y, \hat{\theta}). \tag{7.25}$$

Equation (7.25) can be solved as a posterior MAP estimation problem using Bayesian approach. It can be shown that,

$$P(X = x, \mid Y = y, \hat{\theta}) = \frac{P(Y = y \mid X = x, \hat{\theta})P(X = x \mid \hat{\theta})}{P(Y = y \mid \hat{\theta})}. \tag{7.26}$$

Since y is known the denominator is a constant. Moreover, the white Gaussian noise is independent of X. Therefore, the $P(Y = y \mid X = x, \hat{\theta})$ of the above equation can

be expressed as$\frac{1}{(2\pi\sigma^2)^{\frac{N^2}{2}}}e^{-\frac{||y-x||^2}{2\sigma^2}}$. Given the parameter vector θ the problem reduces to

$$\begin{aligned}\hat{x} &= arg\max_x \left[e^{\frac{-\|y-x\|^2}{2\sigma^2}}e^{-U(x,\phi)}\right] \\ &= arg\min_x \left[\frac{-\|y-x\|^2}{2\sigma^2} + -U(x,\phi)\right] \end{aligned} \tag{7.27}$$

where, $U(x,\phi)$ denotes the *a priori* energy function. We solve (7.27) using proposed hybrid Tabu algorithm and parallel hybrid Tabu algorithm and the performance is compared with that of Simulated Annealing(SA) algorithm.

7.7 Parallel Tabu Search

In the proposed Hybrid Tabu Search (HTS) algorithm of section 5.4, the next move is decided based on the energy of all possible Tabu moves. This incurs a substantial amount of computational burden. The computational burden is reduced by parallelizing the HTS algorithm. This can be described as follows. The image is partitioned into a set of sub-images, of size (16×16) and (32×32). The energy can be computed over each sub-image simultaneously. The energy for the whole image is the sum of the energies of individual sub-images. The computation of energy of each sub-image can be achieved by submitting each job to individual processor. The total energy can be computed in parallel machine. Thus, all possible Tabu moves are determined. If the energy of the next image, i.e. the next move is lower than that of all the moves of the Tabu array, then the next image is accepted as the next move. If the energy of the next image, i.e. the next move is higher than that of all the moves of the Tabu array, then the next image is accepted with probability. This is the Tabu aspiration condition which helps the algorithm to overcome the problem of local minima trapping.

7.7.1 Parallel Hybrid Tabu Search (PHTS) Algorithm

1. Initialize the initial temperature T_{in}.
2. The Initial Image of the algorithm is the degraded image.
3. A Tabu list, i.e. Tabu image set is created to store the recent moves, i.e. the image estimates of the algorithm. The set is of fixed length.
4. The image is partitioned into sub images of suitable sizes.

5. For each sub image :
   (i) Perturb $x_{ij}(t)$ with a zero mean Gaussian distribution with a suitable variance.
   (ii) Evaluate the energy $U_p(x_{ij}(t+1))$ and $U_p(x_{ij}(t))$. If $\Delta f = (U_p(x_{ij}(t+1)) - U_p(x_{ij}(t))) < 0$, assign the modified value as the new value. If $\Delta f > 0$, accept the $x_{ij}(t+1)$ with a probability (if $exp(-\Delta f/T(x)) > random(0,1)$).
   iii) Repeat step (ii) for all the pixels of the sub image.

6. Repeat step 5 for all the sub images.

7. Compute the total energy of the image by adding the energies of the sub images.

8. Compute energy of the updated image $x(t+1)$ as $P_{x(t+1)}$ and compare it with the energy of the Tabu list named as Tabu energy, if $P_{x(t+1)} < P_{Tabu}$, accept $x(t+1)$ as Tabu image.

9. Aspiration condition: If $P_{x(t+1)} > P_{Tabu}$, accept $x(t+1)$ as Tabu image with a probability.

10. Update the Tabu list.

11. Decrease the Temperature according to the logarithmic cooling schedule.

12. Repeat step 4-8 till the stopping criterion is met. In our simulation the stopping criterion is: temperature decreases to a low value.

7.8 Results and Discussions

In simulation, the model learning is carried out for a class of images. We have considered three classes namely, the indoor images, outdoor images, and brain MR images. The learning is carried out with a training image derived from a given class and having learnt, the learning attribute is validated with the test images. These test images together with the training image from a class of images. Although we have shown results for a few test images, it is believed that images possessing a similar intrinsic characteristics could belong to the same class which encompass the training and test images. We have made this observation for MRF model with isotropic and first order neighborhood structure. However, this learning attribute will be valid for isotropic case with higher order neighborhood structure. The first

order clique potential function $V_c(x)$ of MRF model considered in our simulation is given by

$$U(x,\phi) = \sum_{i,j} \alpha \Big\{ (x_{i,j} - x_{i,j-1})^2 + (x_{i,j} - x_{i,j+1})^2 + (x_{i,j} - x_{i-1,j})^2 + ((x_{i,j} - x_{i+1,j})^2 \Big\} + \beta \{h_{i,j} + v_{i,j}\} \quad (7.28)$$

where α, β are the external field and internal field model parameters respectively, $h_{i,j}$ and $v_{i,j}$ are horizontal and vertical line fields respectively.

The problem of model learning is considered in supervised framework. The model parameters once estimated for a training image is used to model the rest of the images from the same class. While training, not only the image parameters such as α and β are estimated, the noise model parameters such as mean and variances are also estimated. We have assumed to have a Gaussian noise model with zero mean and, hence noise variance is the only noise model parameter to be estimated. The posterior energy function corresponding to the above mentioned *a priori* energy function can be expressed as

$$\begin{aligned} U_p(x) &= \sum_{ij} \frac{(y_{ij} - x_{ij})^2}{2\sigma^2} \\ &\quad + \alpha \Big\{ (x_{ij} - x_{i-1,j})^2 + (x_{ij} - x_{i,j-1})^2 + (x_{ij} - x_{i+1,j})^2 + (x_{ij} - x_{i,j+1})^2 \Big\} \\ &\quad + \beta (h_{ij} + v_{ij}) \end{aligned} \quad (7.29)$$

The noisy image of required SNR is generated by adding Gaussian noise of respective variance. The estimated noise variance can be compared with the known variance that serves as an indicator of model learning.

7.8.1 Real Images

The first training image considered is an indoor image as shown in Fig. 7.1(a), captured in Image Processing and Computer Vision Lab. of our department. The corresponding image of SNR 20dB is shown in Fig. 7.1(b). Both the images are considered while learning the models using homotopy continuation method. The model learning algorithm starts from an arbitrary set of parameter vector $\theta = [\alpha,\ \beta,\ \sigma]^T$ and eventually converge to a value of $\alpha = 0.0096$, $\beta = 2.517$ and $\sigma = 21.037$. The arbitrary values correspond to solution of known system and the intermediate values correspond to the zero curves of the homotopy map, and the end value correspond to the solution of the homotopy map at $\lambda = 1$, in other words the solution of the unknown system. The convergence of α, β and σ over the iterations are shown in

Figs. 7.1(c), 7.1(d) and 7.1(e) respectively. The estimates of α, β and σ combinedly represent the solutions of the homotopy map.

Since Gaussian noise of a known variance σ^2 is added, the estimated σ serves as an indicator of the estimate of model parameters as well. It is observed that the estimated σ value of 21.037 is close to the actual σ value of 20.358. Thus, the image model is known. This image model together with the known noise variance σ^2 are now used to obtain the segmented image from a noisy image of SNR 20dB as shown in Fig 7.1(b). The segmented images obtained by SA algorithm, proposed HTS, and parallel hybrid Tabu Search (PHTS), are shown in Figs. 7.2(a), (b) and (c) respectively.

It is observed from Figs. 7.2(a), (b) and (c) that segmentation of the objects could be obtained and also the edges could be preserved in all the cases. This is because of the edge preserving capability of the line fields of the *a priori* clique potential function. As seen from these figures, the edges of the circular object could be obtained because of the edge preserving attribute. The HTS and PHTS algorithms converge faster than of SA albeit visually similar segmented images. The convergence is shown in Fig. 7.5(a), where it is observed that the HTS and PHTS algorithms converge at around 20 iterations where as SA algorithm converges after 40 iterations. The performance is also tested with high noise condition of SNR 15dB and the results obtained by these three algorithms are presented in Figs. 7.2(e), (f) and (g) respectively. It may be seen that Fig. 7.2(g) that even though a few black spots, in other words the misclassified pixels, are present in case of PHTS algorithm, sharp edges could be retained in this case as opposed to SA and HTS algorithms.

The model thus trained is validated with other indoor images as shown in Fig. 7.3(a). The two noisy images of SNR 25 dB and 20 dB are shown in Figs. 7.3(b) and (c) respectively. Segmented images obtained for 25dB case are shown in Figs. 7.3(d), (e) and (f). Although the performance appears visually same, the convergence of HTS and PHTS algorithm are faster than that of SA as shown in Fig. 7.3(b). HTS and PHTS algorithms converge at around 50 iterations where as SA algorithm converges at around 150 iterations. Furthermore, the edges could be preserved in case HTS and PHTS algorithm while in case of SA algorithm the edges are distorted as seen from Fig. 7.3(d). Of course under high noise condition, the edge preserving attribute is not prominent even in case of HTS and PHTS algorithm. This phenomenon is evident from Figs. 7.3 (g), (h) and (i) respectively. Since satisfactory segmentation could be obtained, it can be perceived that same model is valid for other image. The trained model is also tested with another indoor image as shown in Fig. 7.4(a). This image is part of an object. The corresponding

noisy images of SNRs 20 and 15dB are shown in Figs. 7.4 (b) and (c) respectively. Figs. 7.4 (d), (e) and (f) show the segmented results obtained by SA, HTS and PHTS algorithms respectively. Observations, analogous to the previous test image case, are also made here. With increase in noise, this edge preserving attribute yields results less satisfactory than that of low noise case. This may be seen from Figs. 7.4 (g), (h) and (i) respectively. The convergence of the two proposed algorithms are better than that of SA algorithm as shown in Fig. 7.5 (c). As seen from Fig. 7.5 (c) the proposed algorithm converge at around 20 iterations where as SA converges around 40 iterations.

The above results imply that the model trained for one indoor image is valid for other indoor test images. This in turn implies that the two test indoor images belong to the same class from which the training image is derived. Hence, this avoids the estimation of parameters for all the images of the class from which the training image is derived.

The above findings are corroborated with another outdoor scene as shown in Fig. 7.6 (a). The corresponding noisy scene is shown in Fig. 7.6 (b). As in the previous case, these two images are used for learning of image and noise models. The learning of the models is carried out using the homotopy continuation algorithm. The behavior of the model parameters during learning are shown in Figs. 7.6 (c), (d) and (e) respectively. The converged values are $\alpha = 0.031$, $\beta = 4.568$, and $\sigma = 16.399$. The additive white Gaussian noise of $\sigma = 17.106$ has been added and hence serves as an pointer to the learning accuracy. The same model when applied to the noisy image of SNR 20dB, yields results shown in Figs. 7.7 (a), (b) and (c) respectively. The results obtained are satisfactory, but the rate of convergence of HTS and PHTS are found to be faster than that of SA algorithm. This phenomenon may be observed from Fig. 7.9 (a), where the proposed algorithm converge around 15 iterations as opposed to SA algorithm converging after 30 iterations. With decrease in noise i.e. for noisy image of SNR 25dB, appreciable results are obtained as shown in Figs. 7.7 (e), (f) and (g) respectively. Having learnt the training image, the model is now validated for another outdoor image as shown in Fig. 7.8 (a). The corresponding noisy images of SNR 20dB and 15dB are also shown in Figs. 7.8 (b) and (c) respectively. The segmented images obtained for SNR 20dB by SA, HTS and PHTS algorithm are shown in Figs. 7.8 (d), (e) and (f) respectively. It may be observed that the edges could be well preserved in case of PHTS as opposed to HTS and SA algorithm. The results are satisfactory, but the rate of convergence of HTS and PHTS are faster than that of SA algorithm as shown in Fig. 7.9 (b). HTS and PHTS algorithms converge at around 40 while SA converges after 100 iterations.

The performance of the algorithm deteriorates with increase in noise strength. This phenomenon is evident from Figs. 7.8 (g), (h) and (i). The trained model is valid for this image and thus implies that the test image belongs to a class from which the training image is derived.

7.8.2 Brain MR Images

The notion of model learning is also validated brain MR images. The training image considered in our simulation is shown in Fig. 7.10 (a) and the corresponding noisy image of SNR 20dB is shown in Fig. 7.10 (b). These two images are used for model learning. The behavior of the model parameters during learning are shown in Figs. 7.10 (c), (d) and (e). The learning is carried out using homotopy continuation algorithm and the converged values are $\alpha = 0.009$, $\beta = 2.28$, and $\sigma = 10.547$. The estimated value of σ is close to the actual value of 10.364. This indicates the models have been learnt properly. The model, having learnt, is employed for segmentation for the training as well as test images. The segmented results for training image is shown in Figs. 7.11 (a), (b), and (c) and four distinct classes could be obtained in each case. But, as observed in the previous cases, the proposed algorithm converges faster than that of SA algorithm as shown in Fig. 7.14 (a). This fast convergence could be attributed to the incorporation of the notion of Tabu in our algorithm. The learnt model also yielded satisfactory results in case of high noise case of the training image as shown in Fig. 7.11 (d). The segmented results corresponding to the noisy image of SNR 18dB is shown in Figs. 7.11 (e), (f) and (g). The same model is validated for two other brain MR images as shown in Figs. 7.12 (a) and 7.13 (a). The results obtained for the second brain MR image of two noisy cases are shown in Fig 7.12. Satisfactory results could obtained in case all the algorithms but the proposed algorithms converged faster than that of SA shown in Fig. 7.14 (b).

The second test brain MR image is shown in Fig. 7.13 (a) and the noisy versions are shown in Figs. 7.13 (b) and (c). Since, four classes were assumed, the segmented results obtained in case of all the three algorithms showed four classes as shown in Figs. 7.13 (d), (e) and (f). With high noise of SNR 20dB, the performance of the algorithm deteriorated as shown in Figs. 7.13 (g), (h) and (i). As in the previous cases also, the proposed algorithms converged faster than that of SA as shown in Fig. 7.14 (c). Thus, the model having learnt for one case could be tested for other two brain MR images. This implies that the two test brain MR images belong to the same class from which training brain MR image is derived.

7.9 Conclusions

The problem of Markov Random Field model learning is addressed in supervised image segmentation framework. The model learning is accomplished using homotopy continuation algorithm. This proposed notion is validated for real indoor and outdoor images as well. The model is trained for a given image derived from a class and the model, having learnt, is employed for segmentation of images supposed to be members of the same class as that of the training image. We have considered first order isotropic MRF model and estimated the model parameters α *and* β learn the given image. It could be perceived that the trained model yielded satisfactory results for indoor as well as outdoor scenes. Hence in the supervised image segmentation mode, once the training phase is over, the model can be employed for a set of images from which the training image is derived. This notion could be extended to brain MR images. It is found that the brain MR images belong to one class of images. This concept avoids the estimation of model parameters for each and every individual image of a given class. The only bottleneck is the computational burden due to the learning by homotopy continuation method.

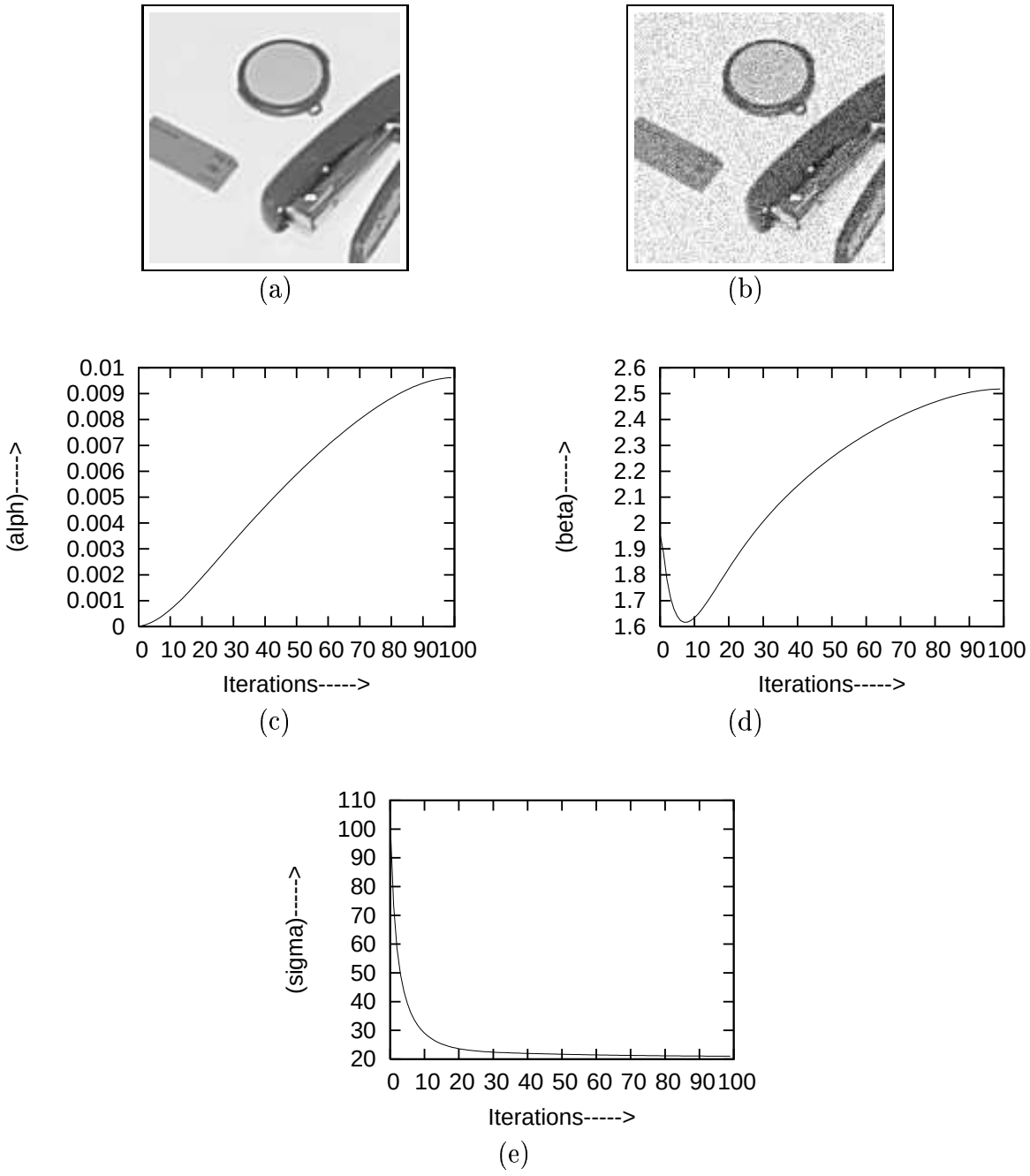

Figure 7.1: *(a)original training real image of size* (128×128)*, (b)noisy image of SNR* $20dB$*; (c),(d) and (e) show the convergence of model parameters alpha, beta and sigma respectively using homotopy continuation method.*

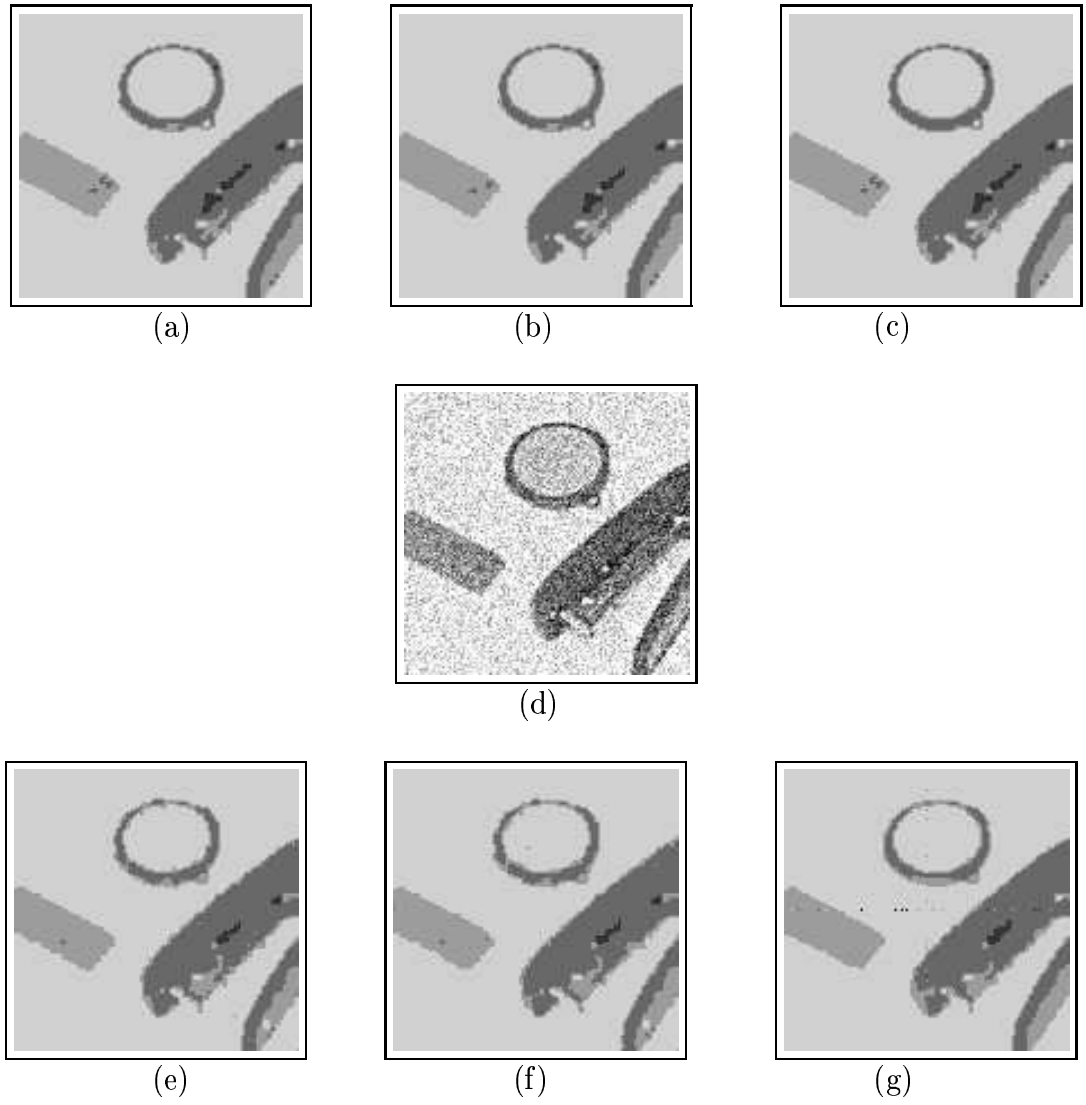

Figure 7.2: *Supervised Segmentation of training real image(object) of size* (128×128) *; (a),(b) and (c) : segmented images of Fig.7.1(b) using SA Algo., HTS Algo. and PHTS Algo. respectively; (d) noisy image of SNR* $15dB$*; (e),(f) and (g) : segmented images of (d) using SA Algo., HTS Algo. and PHTS Algo. respectively*

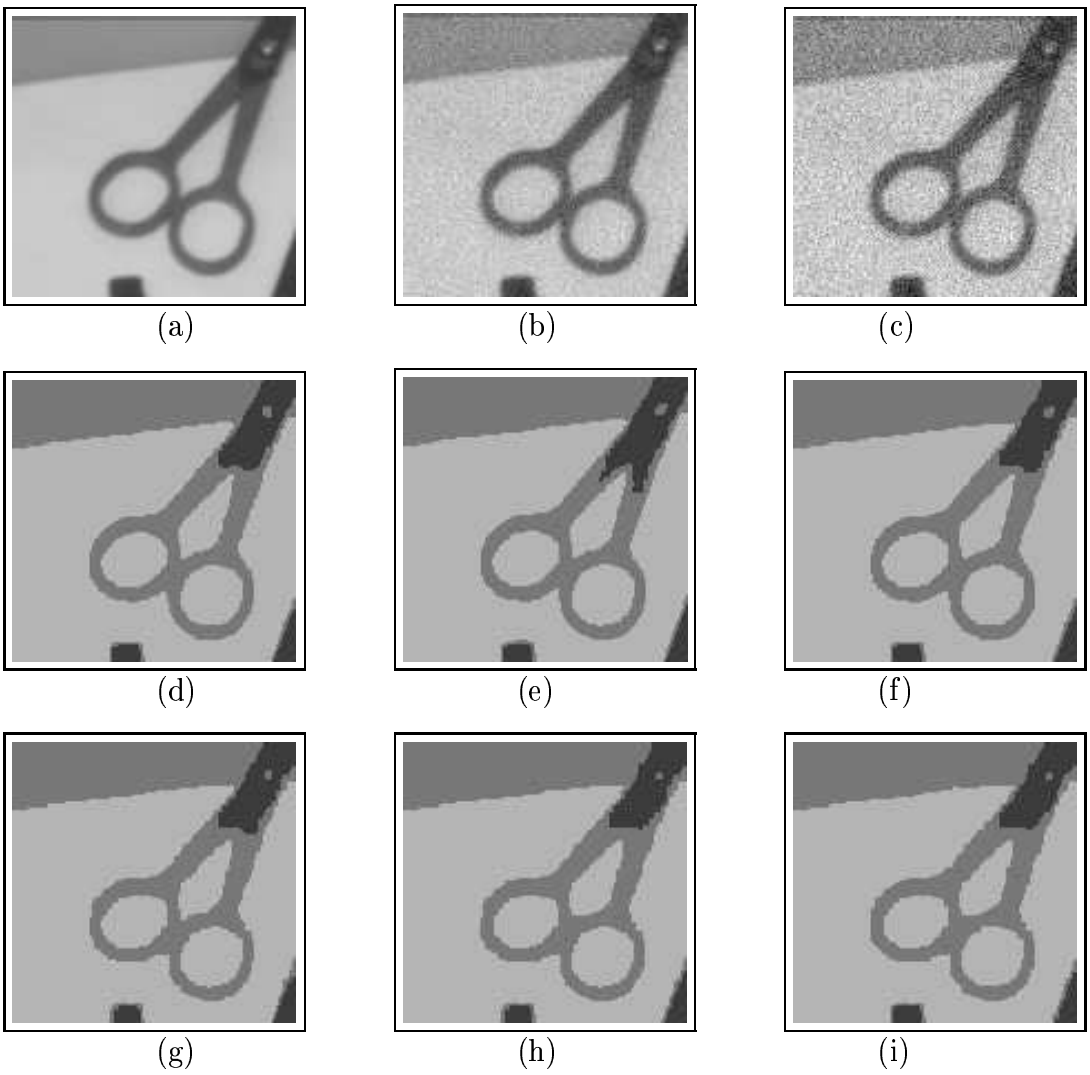

Figure 7.3: *Supervised Segmentation of a test real image of size* (128×128) *: (a) original image; (b),(c) : noisy images with SNR* $25dB$, $20dB$ *respectively; (d),(e) and (f) : segmented images of (b) using SA Algo., HTS Algo., PHTS Algo. respectively; (g),(h) and (i) : segmented images of (c) using SA Algo., HTS Algo. and PHTS Algo. respectively*

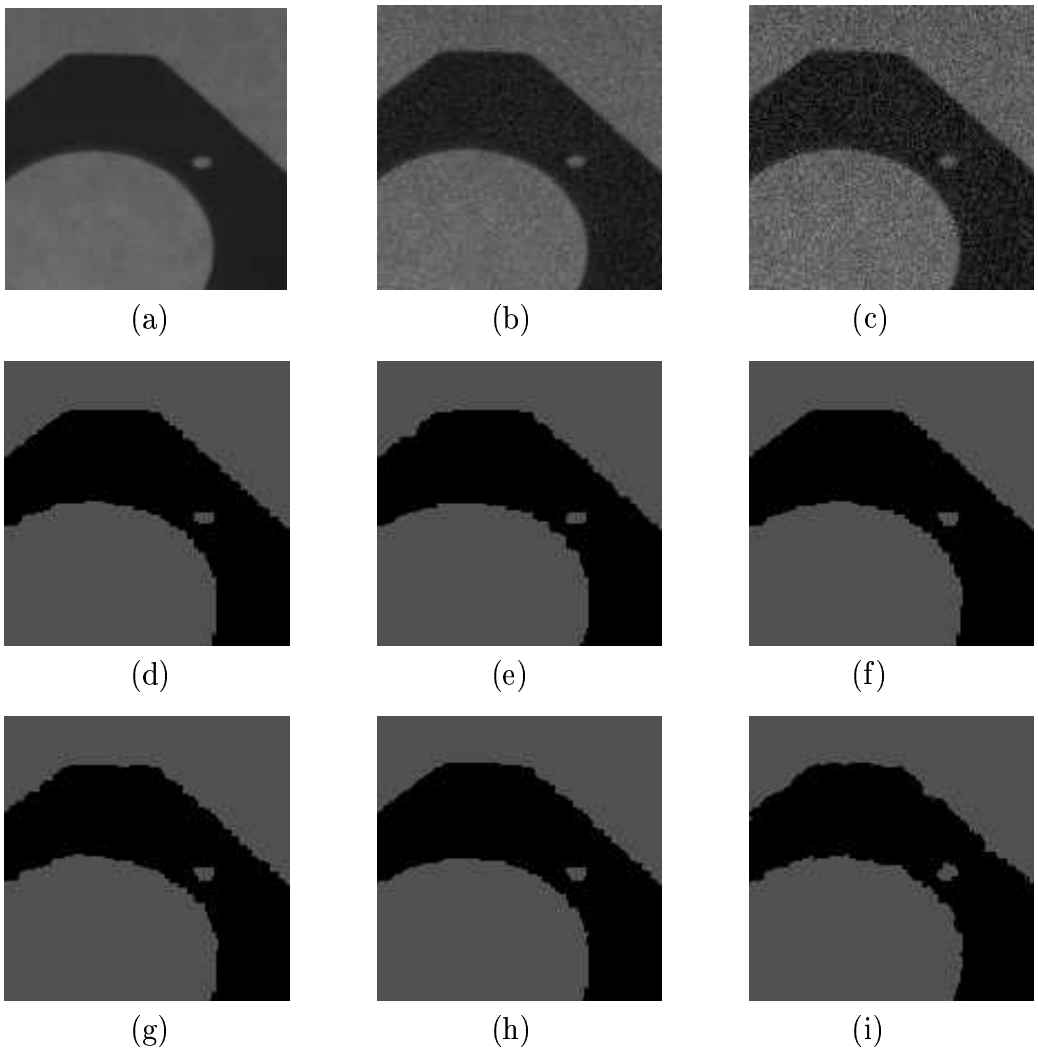

Figure 7.4: *Supervised segmentation of test real image of size* (128×128) *: (a) original image; (b),(c) : noisy images with SNR* $20dB$, $15dB$ *respectively; (d),(e) and (f) : segmented images of (b) using SA Algo., HTS Algo., PHTS Algo. respectively; (g),(h) and (i) : segmented images of (c) using SA Algo., HTS Algo. and PHTS Algo. respectively*

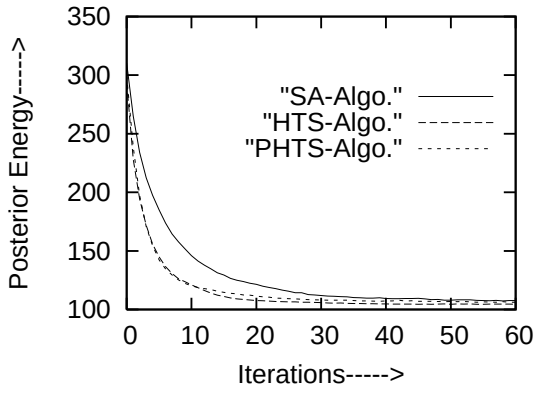

(a)*Posterior Energy plots of Fig. 7.1(b).*

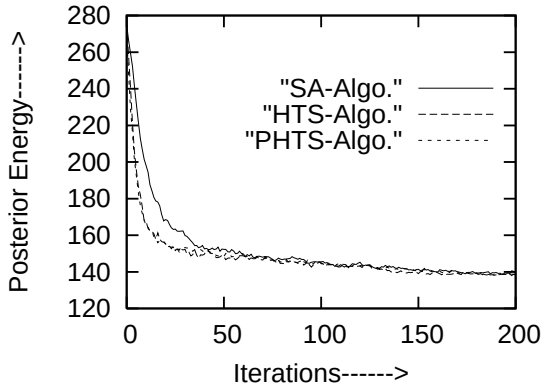

(b)*Posterior Energy plots of Fig. 7.3(b).*

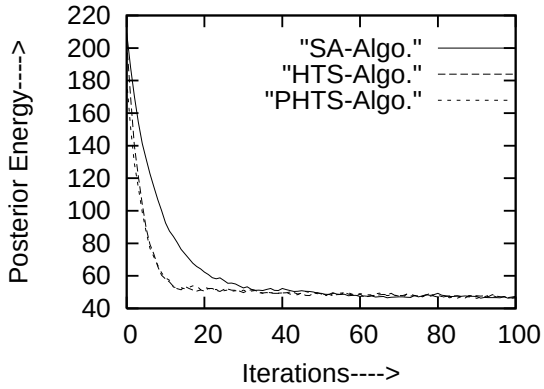

(c)*Posterior Energy plots of Fig. 7.4(c).*

Figure 7.5: *Posterior Energy plots of object images.*

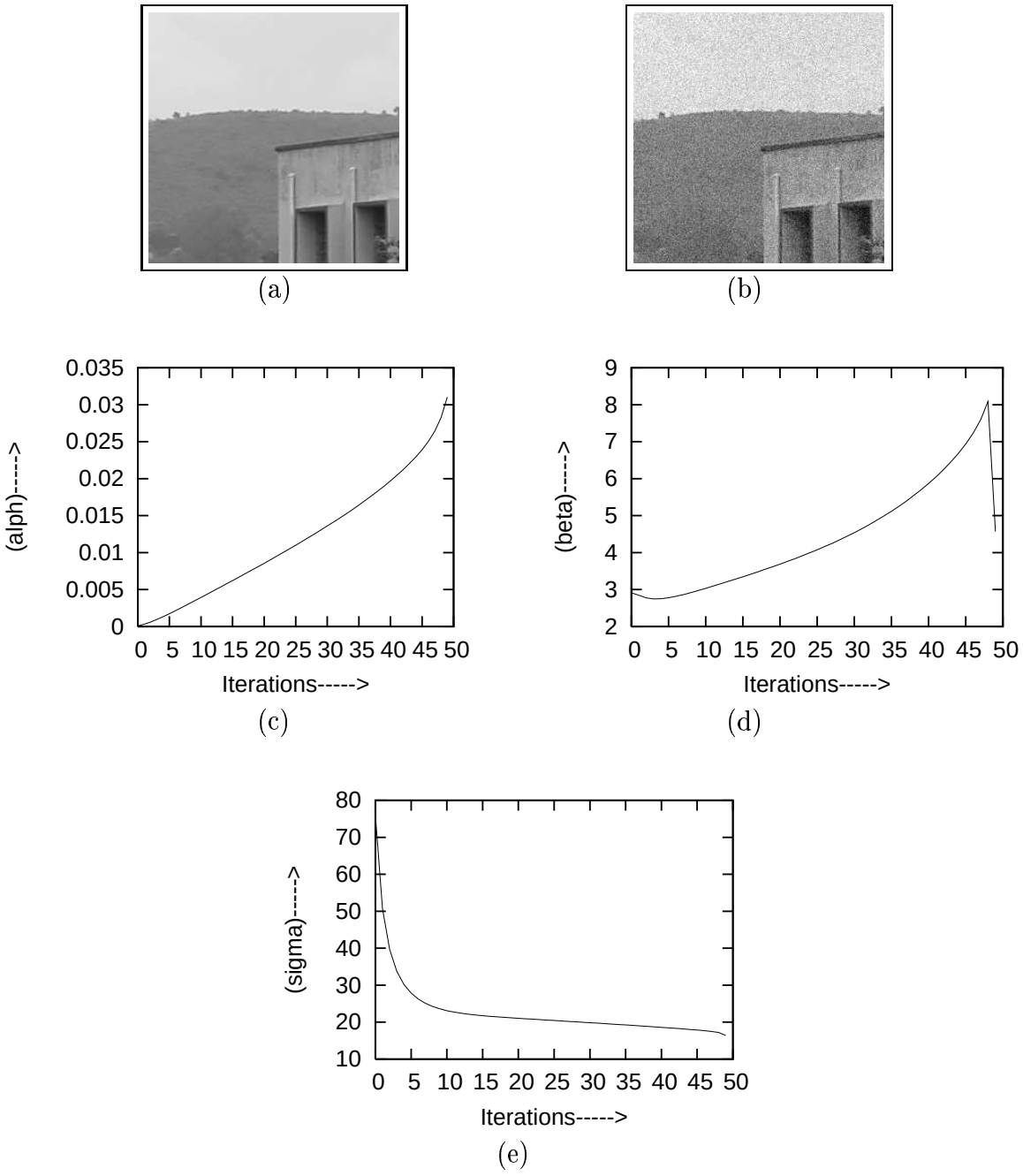

Figure 7.6: *(a) original training real building image of size* (256×256)*, (b) noisy image of SNR* $20dB$*; (c),(d) and (e) show the convergence of model parameters alpha, beta and sigma respectively using homotopy continuation method.*

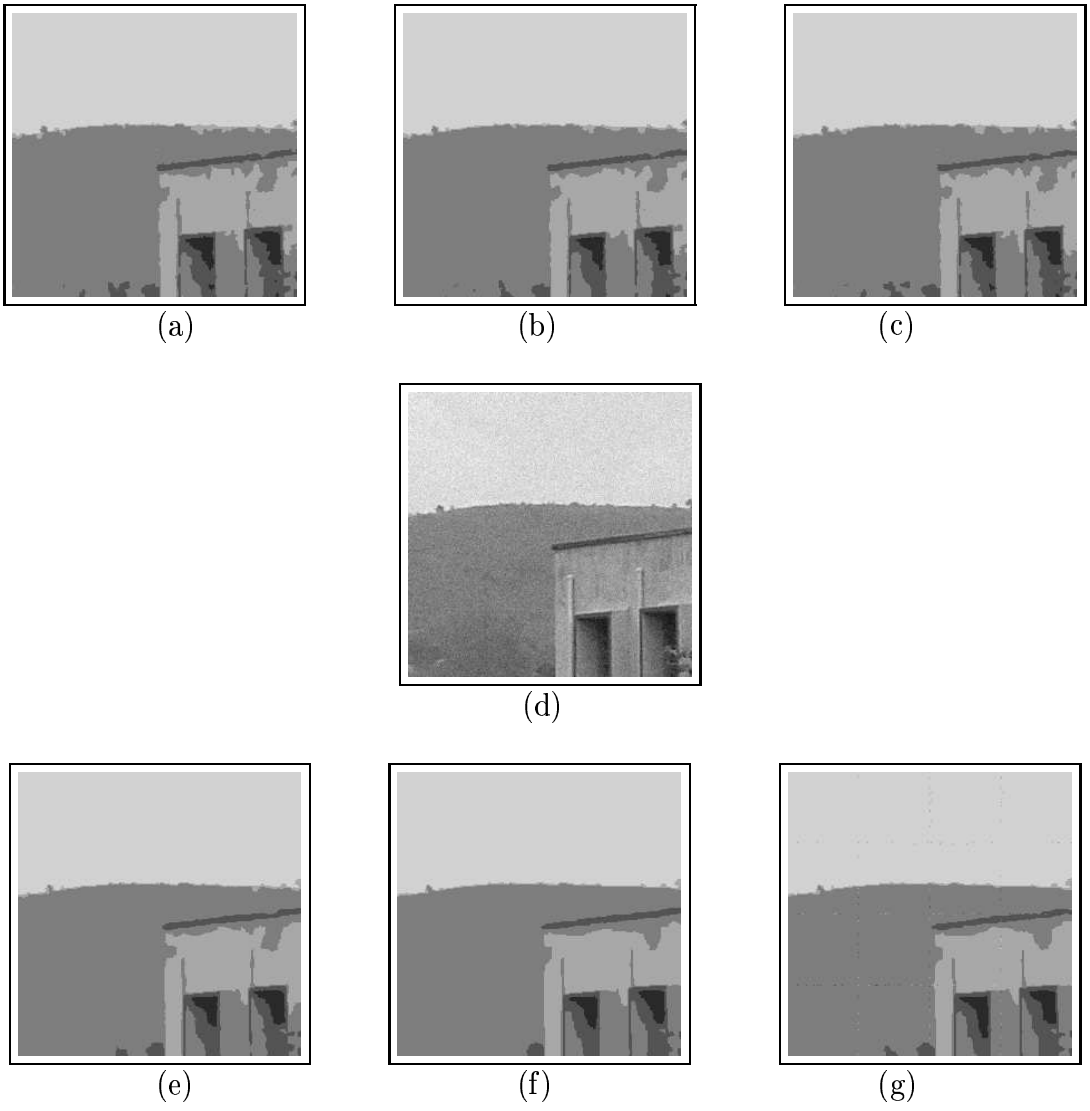

Figure 7.7: *Supervised Segmentation of training real image of size* (256×256) *; (a),(b) and (c) : segmented images of Fig.7.1(b) using SA Algo., HTS Algo. and PHTS Algo. respectively; (d) noisy image of SNR* $25dB$*; (e),(f) and (g) : segmented images of (d) using SA Algo., HTS Algo. and PHTS Algo. respectively*

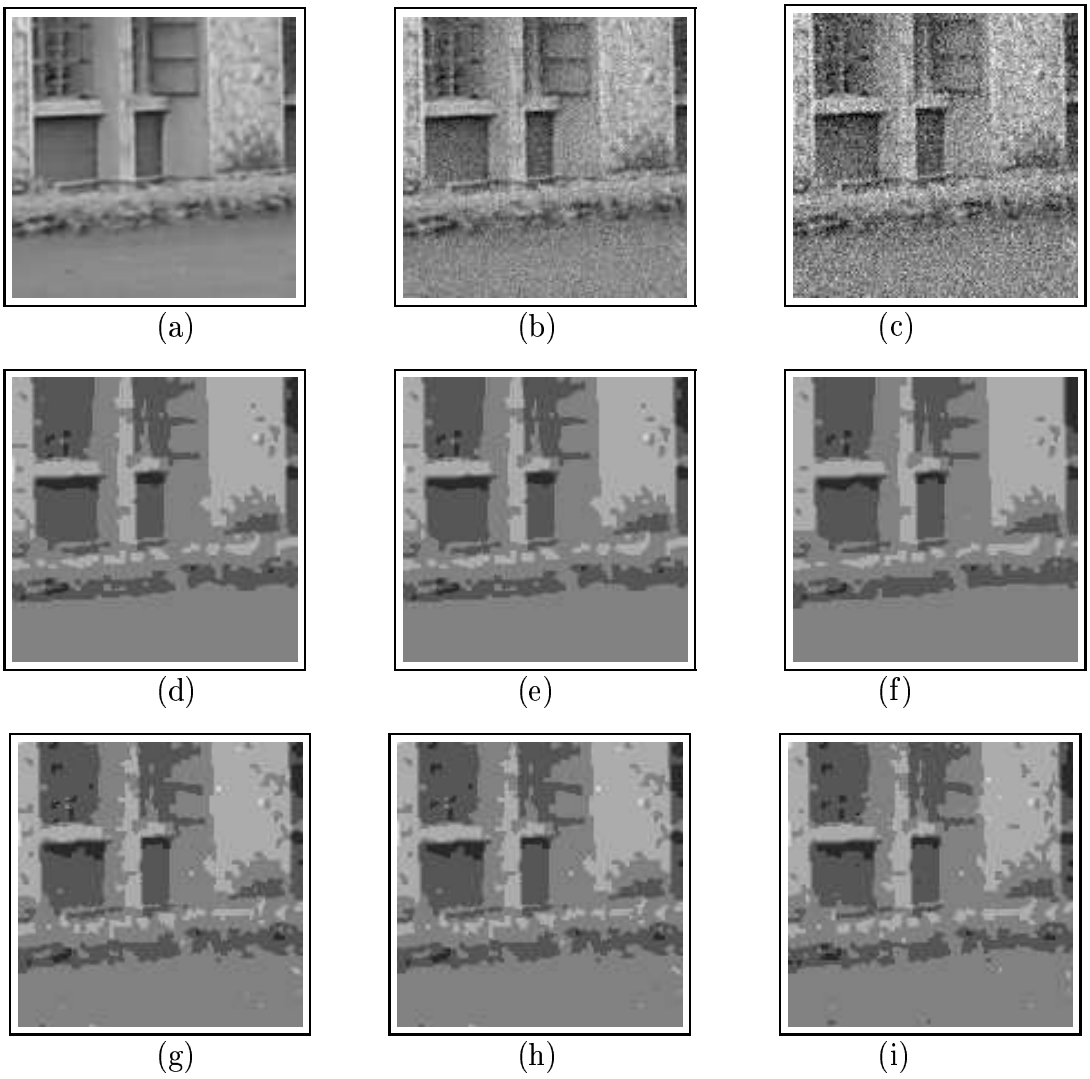

Figure 7.8: *Supervised segmentation of test real image of size* (128×128) *: (a) original image; (b),(c) : noisy images with SNR* $20dB$, $15dB$ *respectively; (d),(e) and (f) : segmented images of (b) using SA Algo., HTS Algo., PHTS Algo. respectively; (g),(h) and (i): segmented images of (c) using SA Algo., HTS Algo., PHTS Algo. respectively*

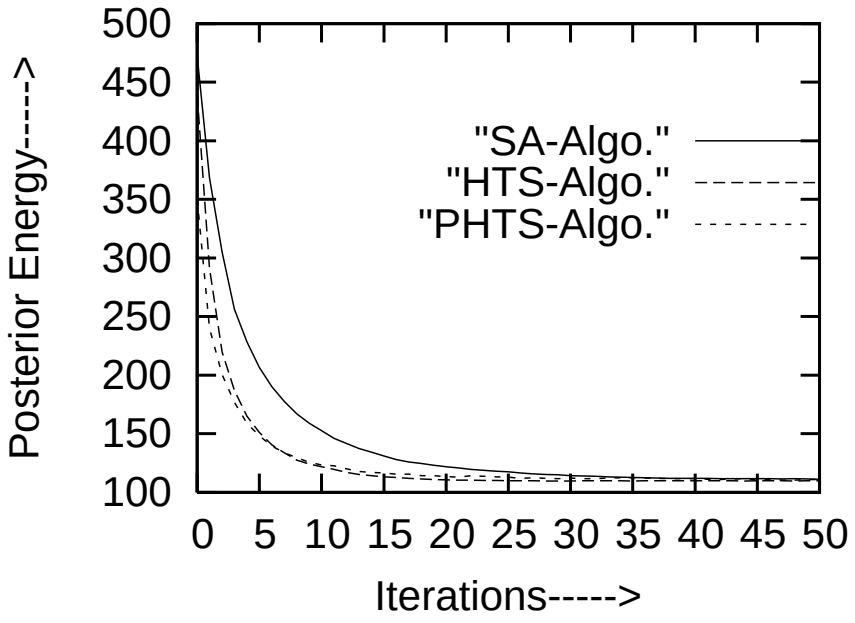

(a)*Posterior Energy plots of Fig. 7.6(b).*

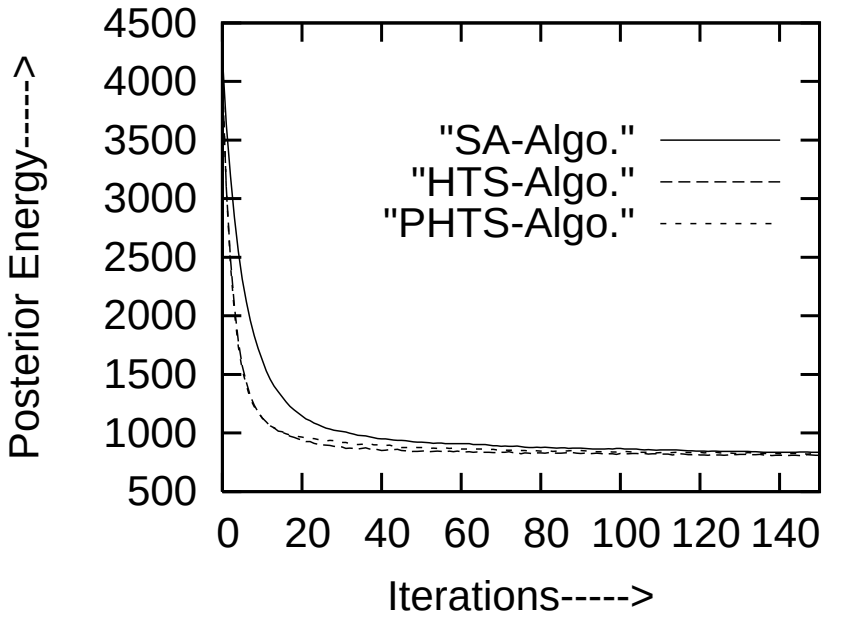

(b)*Posterior Energy plots of Fig. 7.8(b).*

Figure 7.9: *Posterior energy plots of building images*

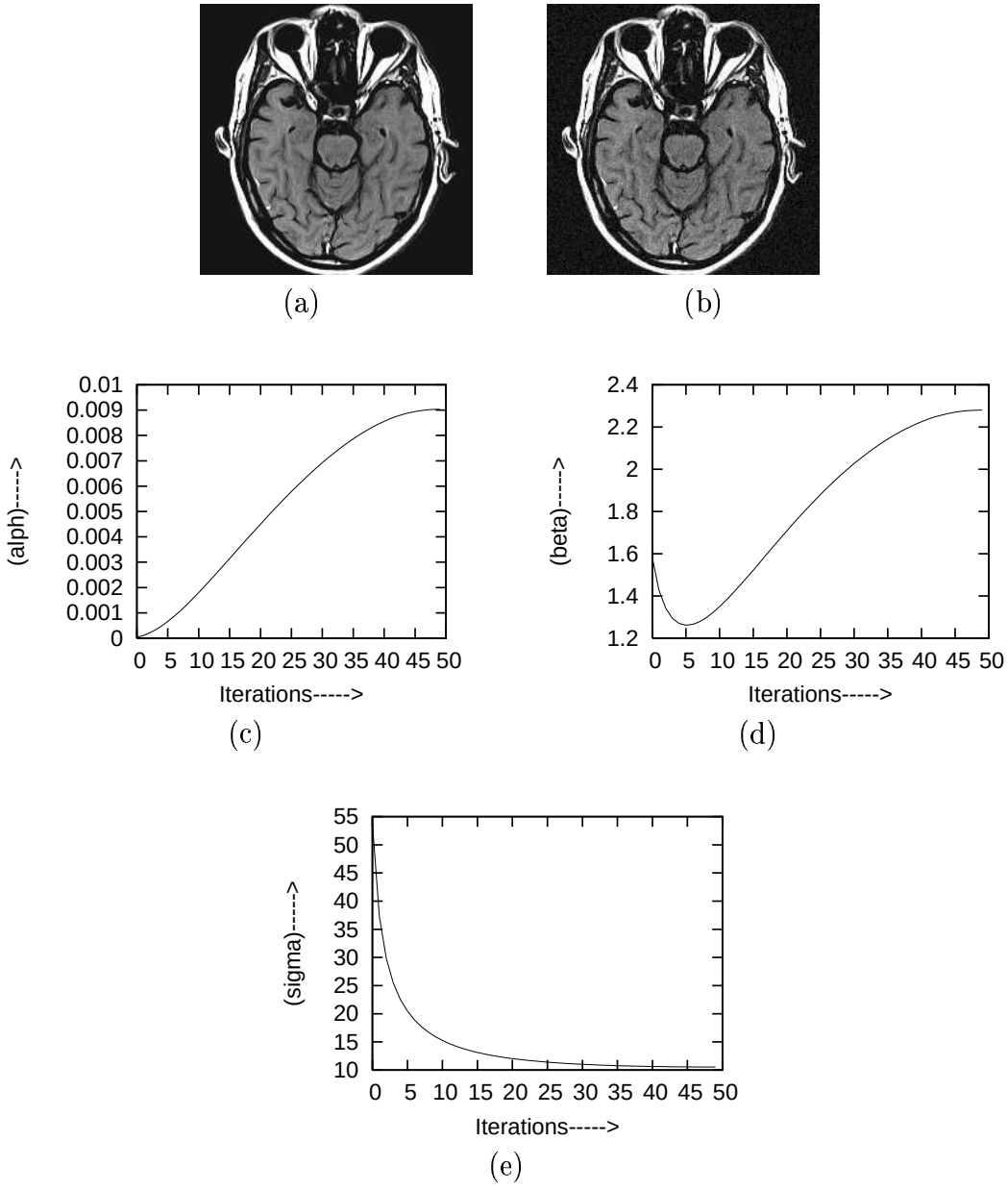

Figure 7.10: *(a)original training brain MR image of size* (214×214)*, (b)noisy image of SNR* $20dB$*; (c),(d) and (e) show the convergence of model parameters alpha, beta and sigma respectively using homotopy continuation method.*

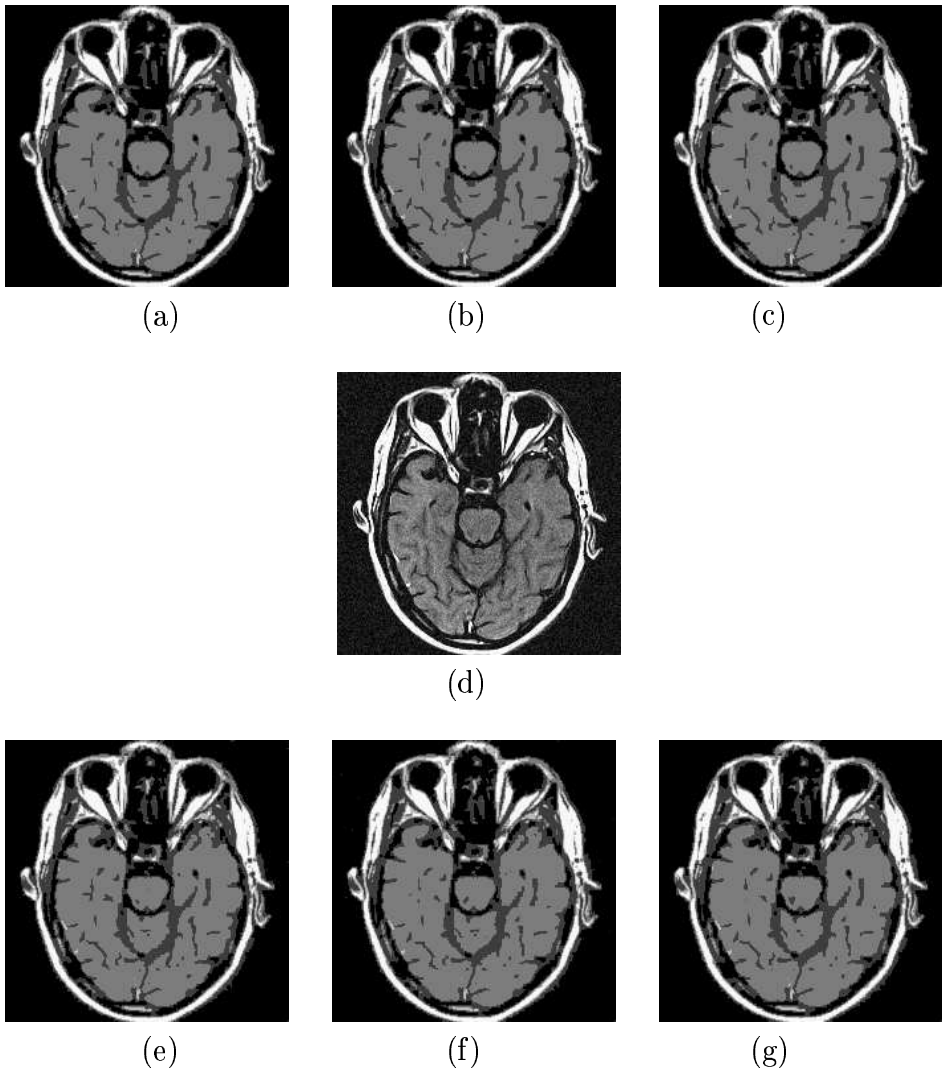

Figure 7.11: *(a),(b) and (c) show the segmented images of training brain MR image using SA Algo., HTS Algo. and PHTS Algo. respectively; (d) noisy image of SNR* $18dB$*.; (e),(f) and (g)show the segmented images of (d) using SA Algo., HTS Algo. and PHTS Algo. respectively*

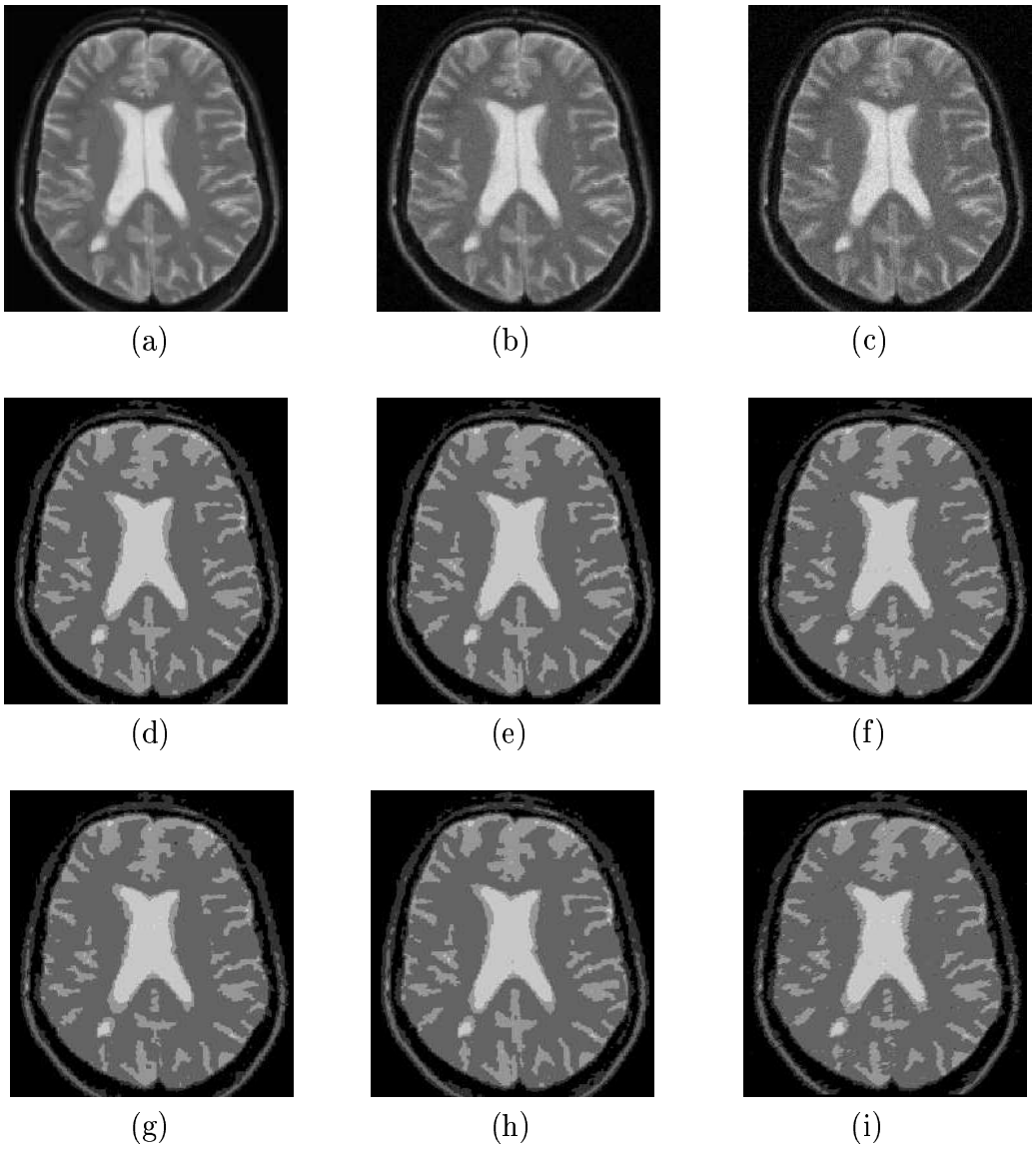

Figure 7.12: *Supervised segmentation of a test brain MR Image of size* (219×238) *: (a) original image; (b),(c) : noisy images with SNR* $25dB$*,* $20dB$ *respectively; (d),(e) and (f) : segmented images of (b) using SA Algo., HTS Algo. and PHTS Algo. respectively; (g),(h) and (i) : segmented images of (c) using SA Algo., HTS Algo. and PHTS Algo. respectively*

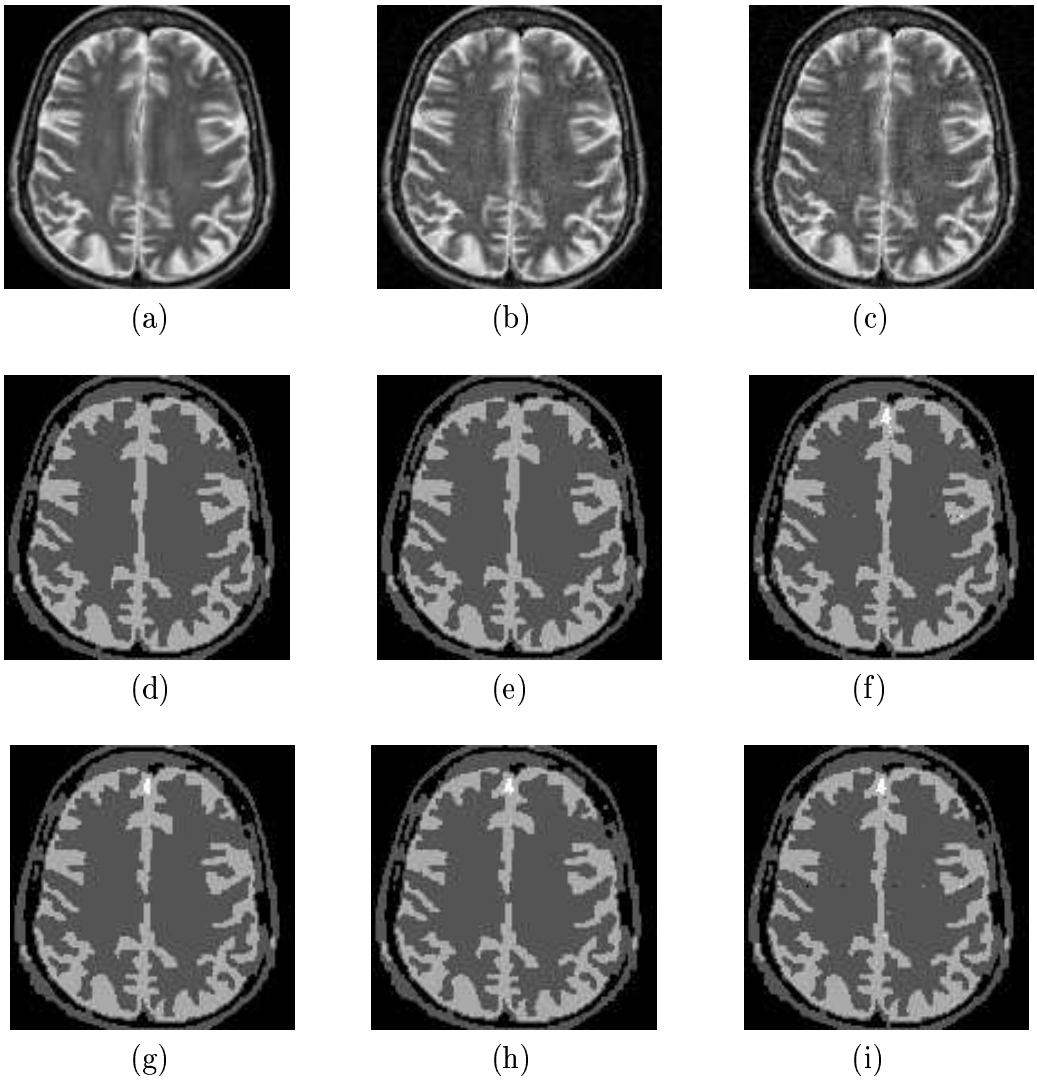

Figure 7.13: *Supervised segmentation of test brain MR Image of size* (128×128) *: (a) original image; (b),(c) : noisy images with SNR* $22dB$, $20dB$ *respectively; (d),(e) and (f) : segmented images of (b) using SA Algo., HTS Algo. and PHTS Algo. respectively; (g),(h) and (i) : segmented images of (c) using SA Algo., HTS Algo. and PHTS Algo. respectively*

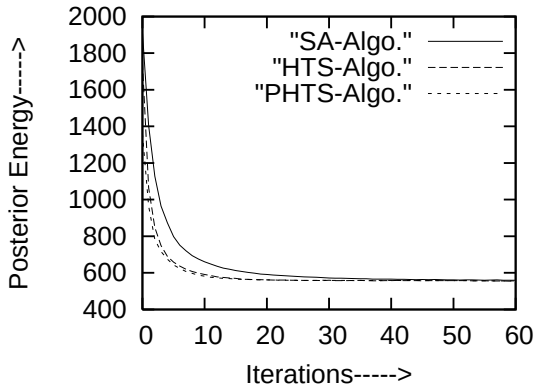

(a)*Posterior Energy plots of Fig. 7.10(b).*

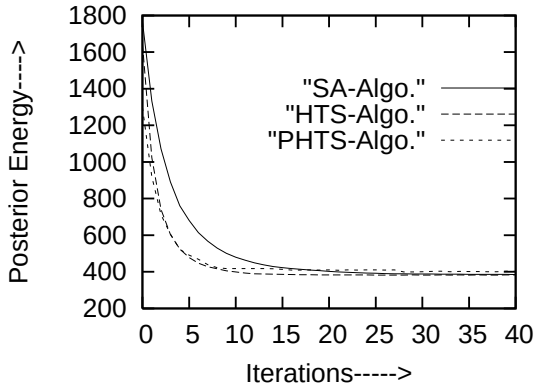

(b)*Posterior Energy plots of Fig. 7.12(c).*

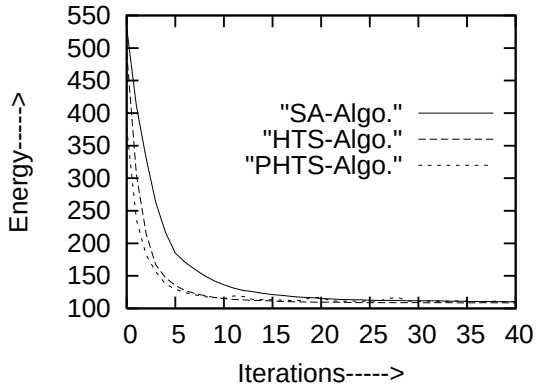

(c)*Posterior Energy plots of Fig. 7.13(c).*

Figure 7.14: *Posterior energy plots of brain MR images.*

Chapter 8

Conclusions

Segmentation of brain MR images is the objective of this dissertation. Although segmentation of brain MR images has been addressed in the literature for quite some time, many challenging issues still remains open to be investigated. This work makes a systematic attempt to devise and develop supervised and unsupervised brain MR image segmentation schemes that would augment the automated vision system and which in turn will facilitate the clinical experts for an accurate diagnosis.

The initial portion of this thesis is devoted to provide a background on Magnetic Resonance Imaging, MRF and HMRF models, and Tabu Search Technique.

The initial part of this research work is directed towards developing supervised image segmentation scheme. In this framework, the problem is cast as a pixel labeling problem, and MRF and HMRF models are employed to model the *a priori* class label and the observed degraded image respectively. The GHMRF model parameters μ, σ for each tissue class and the MRF model parameters δ are selected on an ad hoc basis. This image label estimation problem is formulated in Bayesian framework using MAP criterion. Often, SA algorithm is employed to obtain the MAP estimates and hence segmentation. SA algorithm converges to the optimal solution at the cost of high computational burden. This could be due to the cycling of the moves in the search space. In order to overcome the above bottleneck, a HTS algorithm is proposed exploiting the notion of annealing blended with the concept of Tabu search. This was employed for estimation of image labels. The algorithm is found to converge faster than that of SA algorithm. The results obtained by the proposed algorithm are in some cases, found to be better than those obtained by SA. The algorithm could be successfully tested with the synthetic as well as brain MR images. These synthetic images are generated using GHMRF model and Gibb's sampler. Satisfactory results could be obtained in both synthetic as well as brain MR images. The only bottleneck in this scheme is to choose model

parameters for each tissue class. Hence, with increase in the number of classes, the selection of the model parameters will be a horrendous task. The performance of the globally convergent algorithms is also compared with ICM algorithm, a locally convergent one. As expected, the proposed algorithm outperformed ICM algorithm. The algorithm yielded satisfactory results even under high noisy conditions.

In this supervised framework, the problem of selection of model parameters becomes a horrendous task with increase in number of classes, and hence the algorithm may be constrained to problems having moderate number of classes. Future work includes developing methodologies of selection of these initial parameters for any number of classes. Also, computation of the time complexity of the proposed algorithm and other stochastic algorithm is worth pursuing.

The bottleneck of selection of model parameters is overcome by addressing the problem in unsupervised framework in Chapter 6. In this framework, the number of classes, GHMRF model parameters μ and σ for every class, and the image labels are assumed to be unknown. Since the optimal image label estimates depend upon optimal parameters and the optimal parameter estimate depends upon optimal image labels, this problem may be viewed as incomplete data problem. Here also GHMRF model is used to model the observed degraded images.

While the MRF model is used to model unknown class labels, the MRF model parameters δ, of course, is assumed to be known. Motivated by the work of Dempster et. al.[36] and also Zhang[95], this problem is also formulated in EM frame work. Zhang et. al. have addressed this problem where the image label estimates are obtained by ICM algorithm in the E-step of the EM algorithm. Thus, performance of their algorithm is very much dependent upon the choice of initial parameters. Zhang et. al. have suggested a histogram based strategy to determine the initial parameters. This problem of selection of initial parameters is overcome by proposing a TEM algorithm where the hybrid Tabu search algorithm is used to obtain the image estimates. Because of the globally convergent property of HTS algorithm, TEM algorithm does not need to have a proper choice of initial parameters. Indeed, the algorithm performed satisfactory even when starting from different arbitrary initial conditions. Here, the term "arbitrary" does not mean any complete random ones, rather from a set of parameters. This may be intuitively acceptable, because the algorithm may not operate with initial model parameters without a bound. The results obtained by our algorithm are visibly comparable to that of Zhang's approach, but the potentiality of our algorithm is that no computation of initial parameters are necessary. This is indeed a step towards making a complete automated brain MR image segmentation scheme. The only limitation of the algorithm is that the

MRF model parameter δ is selected on an ad hoc basis. It is worth pursuing to reformulate the parameter estimation problem to estimate the MRF model parameter together with the GHMRF model parameters. This will make the scheme a complete unsupervised one. Our algorithm starts with assuming more number of classes than that the actual ones and converges to the required number of classes. Since the actual number of classes are unknown, the selected number of initial classes are also on trial and error basis. Large number of initial classes means estimation of large number of parameters which in turn increases computational burden. It will be worth pursuing in future to develop strategies to overcome these problems. However, the proposed algorithm could be successfully tested for synthetic as well as real brain MR images. Estimation of Bias field would enhance the worth of the work.

Segmentation based on a new notion of model learning is introduced in Chapter 7. Although this segmentation scheme may be viewed as supervised, the model parameters are not chosen on trial and error basis rather are estimated to be subsequently used for image label estimation. The problem addressed may be viewed as supervised learning. In this scheme, the model learns or in other words the model parameters learn a given image as opposed to a class of images. The model, thus learnt, is used as the model for all the images of a class from which the training image is derived. Here, the weak membrane model is considered as the image model. The parameter estimation problem is formulated in MPCL framework and the estimation of the parameters reduces to solving highly nonlinear equations. Since, no *a priori* knowledge of the parameters are available, the globally convergent homotopy continuation based algorithm is used to determine the optimal estimates of the parameters. There after these estimated parameters are used to obtain the image label estimates for a set of images which are assumed to belong to the same class as that of the training image.

The model learning problem could be successfully tested with real indoor, outdoor and brain MR images. It is to be noted that model that the learned one indoor scene yielded satisfactory results for other indoor images. Analogous observations are also made for outdoor as well as brain MR images. This notion avoids the ad hoc selection of the model parameters as well as parameter estimation for each and every individual image. The image estimation is achieved by MAP principles and the determination of MAP estimates are computationally involved. In order to reduce the computational burden, a Parallel Hybrid Tabu Search (PHTS) algorithm is developed. The performance of the PHTS and HTS algorithm are compared with that of SA algorithm and it was found that the proposed ones converged faster than

that of SA. Furthermore, in some cases, the edge preserving capability of PHTS algorithm is found to be better than that of SA and HTS algorithm.

This supervised learning can be extended to unsupervised learning and hence both parameter estimation and image label estimation can be accomplished simultaneously. This problem is worth pursuing and computational burden of parameter estimation can be reduced by pursuing the notion of learning of sub images.

Bibliography

[1] Nikhil R. Pal and Sankar K. Pal, "A review on image segmentation techniques," *Pattern Recognition*, vol. 26, No. 9, pp. 1277-1294, Sept. 1993.

[2] R. C. Gonzalez, R. E. Woods, *Digital Image Processing*, Pearson Education, 2001.

[3] Anil K. Jain, *Fundamentals of Digital Image Processing*, Prentice-Hall of India Pvt. Ltd., 2001.

[4] Alan C. Bovik, *Hand Book of Image and Video Processing*, Academic Press, 2000.

[5] Nobuyuki Otsu, "A threshold selection method from gray-level histograms," *IEEE Transc. Systems,Man and Cybe5rnetics*, vol. 9, pp. 62-66, Jan. 1979.

[6] J. T. Tou, R. C. Gonzalez, *Pattern Recognition Principles*, Addison-Wesley, 1974.

[7] S. Sanjay Gopal and J. J. Hebert, "Maximum likelihood pixel labeling using a spatially variant finite mixture model," *IEEE Transc. Nuclear Science*, vol. 44, No. 4, pp. 1578-1582, Aug. 1997.

[8] Todd R. Reed and J. M. Hans Du Buf, "A review of recent texture segmentation and feature extraction techniques," *CVGIP: Image Understanding*, vol. 57, No. 3, pp. 359-372, 1993.

[9] Stan Z. Li, *Markov Random Field Modelling in Image Analysis*, Springer-Verlag, 2001.

[10] K. S. Shanmugan, A. M. Breipohl, *Random Signals: Detection Estimation and Data Analysis*, John Wiley, 1988.

[11] S. Geman and D. Geman, "Stochastic relaxation, Gibbs distributions, and the Bayesian restoration of images," *IEEE Trans. Pattern Analysis and Machine Intelligence*, vol.6 ,no. 6, pp 721-741,1984.

[12] D. Geman, S. Geman, C. Graffigne and P. Dong, "Boundary detection by constrained optimization," *IEEE Trans. Pattern Recognition and Machine Intelligence*, vol. 12, no. 7, pp 609-628, July 1990.

[13] D. Geman and G. Reynolds, "Constrained restoration and recovery of discontinuities," *IEEE Trans. Pattern Analysis and Machine Intelligence*, vol. 14, No. 3, pp 367-383, Mar. 1992.

[14] Julian Besag, "Spatial interaction and the statistical analysis of latice systems (with discussion)," *J. Royal Statistical Society*, ser. B., vol. 36, No.2, pp. 192-326, 1974.

[15] Julian Besag, "On the statistical Analysis of Dirty pictures," *J. Royal Statistical Society*, 48, No. 3, pp. 259-302, 1986.

[16] F. R. Hansen and H. Elliott, "Image segmentation using simple Markov Field Models," *Computer Graphics and Image Processing*, 20, pp. 101-132, 1982.

[17] H. Elliott, H. Derin, R. Cristi, D. Geman, "Application of the Gibbs distribution to Image Segmentation," *IEEE Proc. Int. Conf. Acoustics, Sound and Signal Processing, ICASSP'84*, vol. 9, pp. 678-681,Mar. 1984.

[18] H. Derin, H. Elliott, R. Cristi, D. Geman, "Bayes smoothing algorithms for segmentation of images modeled by Markov Random Fields," *IEEE Proc. Int. Conf. Acoustics, Sound and Signal Processing, ICASSP'84*, vol. 9, pp. ,Mar. 1984.

[19] H. Derin, H. Elliott and J. Kuang, "A new approach to parameter estimation for Gibbs random fields," *IEEE Proc. Int. Conf. Acoustics, Sound and Signal Processing, ICASSP'85*, vol. 10, pp. 913-916, 1985.

[20] J. L. Marroquin, E. A. Santana and S. Botello, "Hidden markov Measure Field Models for Image Segmentation," *IEEE Trans. Pattern Analysis and Machine Intelligence*, vol. 25, No. 11, pp. 1380-1387, 2003.

[21] Chaur-Chin Chen and Richard C. Dubes, "Environmental Studies of ICM Segmentation Algorithm," *Jour. of Information Science and Engineering*, vol.6, pp. 325-337, 1990.

[22] S. A. Barker and P. J. W. Rayner, "Unsupervised image segmentation using Markov random field models," *Pattern Recognition*, vol. 33, No. 4, pp. 587-602, April. 2000.

[23] C. D'Elia, G. Poggi and G. Scarpa, "A Tree Structured Markov Random Field Model for Bayesian Image Segmentation," *IEEE Trans. Image Processing*, vol. 12, No. 10, pp. 1259-1273, 2004.

[24] Chee Sun Won and H. Derin, "Segmentation of noisy textured images using Simulated Annealing," *IEEE Proc. Int. Conf. Acoustics, Sound and Signal Processing, ICASSP'87*, vol. 12, pp. 563-566, Apr. 1987.

[25] L. R. Rabiner and B. H. Juang, "An Introduction to hidden Markov models," *IEEE ASSP Magazine*, vol. 3, No. 1, pp. 4-6, Jan. 1986.

[26] L. R. Rabiner, "A Tutorial on hidden Markov models and selected applications in speech recognition," *IEEE Proceedings.* , vol. 77, No. 2, pp. 257-286, Feb. 1989.

[27] Magdi A. Mohamed and Paul Gader, "Generalized hidden Markov models-Part I: Theoretical Frameworks," *IEEE Transaction on Fuzzy Systems*, vol. 8, No. 1, Feb. 2000.

[28] H. Yang and K. Alman, "Two-dimensional shape classification using hidden Markov model," *IEEE Trans. on Pattern Analysis and Machine Intelligence*, vol. 13, pp. 1172-1184, Nov. 1991.

[29] P. Andrey and P. Tarroux, "Unsupervised Segmentation of Markov Random Field Modeled Textured Images Using Selecetionist Relaxation," *IEEE Trans. Pattern Analysis and Machine Intelligence*, vol. 20, no. 3, pp. 252-262, 1998.

[30] J. Luo, C. W. Chen and K. J. Parker, "On the application of Gibbs random field in Image Processing: from segmentation to enhancement," *J.Electron Imaging*, vol. 4, pp. 187-198, 1995.

[31] S. A. Kirkpatrick, C. D. Gellatt Jr. and M. P. Vecchi, "Optimization by Simulated Annealing," *Science*, vol. 220, pp. 671-680, 1983.

[32] A. Kirkpatrick, "Optimization by Simulated Annealing: Quantitative studies," *Statistical physics*, vol. 34, pp. 975-986, 1984.

[33] E. Arts and J. Korst, "Simulated Annealing and Boltzmann Machine", *Wiely,New York*, 1989.

[34] J. A. Vlontzos and S. Y. Kung, "Hidden Markov Models for character recognition," *IEEE Trans. Image Processing*, vol. 1, pp. 539-543,Oct. 1992.

[35] M. Vannier, R. Butterfield, D. Jordan, W. Murphy, "Multi-Spectral Analysis of Magnetic Resonance Images," *radiology*,vol. 154, pp. 221-224, 1985.

[36] A. P. Dempster, N. M. Laird and D. B. Rubin, "Maximum Likelihood from Incomplete Data via the EM algorithm," *J.Royal Statistical Society*, vol. 39, pp. 1-38, 1977.

[37] Jun Zhang, "The mean field theory in EM procedures for Markov Random Fields," *IEEE Transc. Signal Processing*, vol. 40, No. 10, Oct. 1992.

[38] Jun Zhang, "The mean field theory in EM procedures for blind Markov Random Field image restoration," *IEEE Transc. Image Processing*, vol. 2, No. 1, Jan. 1993.

[39] L. Xu and M. I. Jordan, "On convergence properties of the EM algorithm for gaussian mixtures," *Neural Computation*, vol. 8, pp. 129-151, 1996.

[40] J. Zhang, J. W. Modestino and D. A. Langan, "Maximum Likelihood parameter estimation for unsupervised stochastic model-based image segmentation," *IEEE Trans. Image Processing*, 3(4), pp. 404-420, 1994.

[41] C. A. Bouman and M. Shapiro, "A multiscale random field model for Bayesian image segmentation," *IEEE Trans. Image Processing*, 3(2), pp. 162-177, 1994.

[42] P. K. Nanda, "MRF model learning and application to image restoration and segmentation," *Ph.D. Dissertation, IIT Bombay*, 1995.

[43] Zhenyu Zhou, Richard M.Leahy and Jinyi Qi, "Approximate Maximum Likelihood Hyperparameter Estimator for Gibbs Priors," *IEEE Trans. Image Processing*, vol. 6, No. 6, June 1997.

[44] H. Cheng and C. A. Bouman, "Multiscale Bayesian segmentation using a trainable context model," *IEEE Trans. Image Processing*, 10(9), pp. 511-525, 2001.

[45] R. Fjortoft, Y. Delignon, W. Pieczynski, M. Sigelle and F. Tupin, "Unsupervised classification of radar images using hidden Markov chains and hidden Markov random fields," *IEEE Transc. Geoscience and Remote Sensing*, vol. 41, No. 3, pp. 675-686, Mar. 2003.

[46] F. Forbes, N. Peyrard, "Hidden Markov random field model selection criteria based on mean-field-like approximations," *IEEE Pattern Analysis and Machine Intelligence*, vol. 25, No.9, pp. 1089-1101, Sept. 2003.

[47] Huawu Deng and David A. Clausi, "Unsupervised image segmentation using a simple MRF model with a new implementation scheme," *Pattern Recognition*, vol. 37, No. 12, pp. 2323-2335, Dec. 2004.

[48] Shu-Kay Ng and Geoffrey J. McLachlan, "Speeding up the EM algorithm for mixture model-based segmentation of Magnetic resonance images," *Pattern Recognition* vol. 37, No. 8, pp. 1573-1589, Aug. 2004.

[49] Tamas Sziranyi, Josiane Zerubia, Laszlo Czuni, David Geldreich and Zoltan Kato, "Image segmentation using Markov random field model in fully parallel cellular network architectures," *Real-Time Imaging*, vol. 6, No. 3, pp. 195-211, June 2000.

[50] Fabien Salzenstein and Wojciech Pieczynski, "Parameter estimation in hidden Fuzzy Markov random fields and image segmentation," *Graphical Models and Image Processing*, vol. 59, No. 4, pp.205-220, July 1997.

[51] Yongyue Zhang, Michael Brady and Stephen Smith, "A hidden markov random field model for partial volume classification," *Neuro Image*, vol. 13, No. 6, Supplement 1, pp.291, June 2001.

[52] Padhraic Smyth, "Belief networks, hidden Markov models and Markov random fields: A unifying view," *Pattern Recognition Letters*, vol. 18, No. 11, pp. 1261-1268, Nov. 1997.

[53] L. Aggoun, L. Benkherouf and A. Benmerzouga, "Optimal filters for a hidden Markov random field model," *Mathematical and Computer Modelling*, vol. 31, No. 13, pp. 1-9, June 2000.

[54] Todd K. Moon, "The Expectation-Maximization Algorithm," *IEEE Signal Processing*, Nov. 1996, pp. 47-59.

[55] Fred Glover, "Tabu-Search-Part-I," *ORSA Journal on Computing*, vol. 1, No. 3, pp. 190-206, 1989.

[56] Fred Glover, "Tabu-Search-Part-II," *ORSA Journal on Computing*, vol. 2, No. 1, 1990.

[57] F. Glover and M. Laguna, *Tabu Search*, Kluwer Academic Publishers, Boston, 1997.

[58] K. S. Al-Sultan, "A Tabu search approach to the clustering problem," *Pattern Recognition*, vol. 28, No. 9, pp. 1443-1451, 1995.

[59] D. Kavabage, D. H. Howocks, W. Karalooga and A. Kaliant, "Designing digital FIR filters using Tabu search algorithm," *Proc. IEEE Int. Symposium on Circuits and Systems*, June 9-12, pp. 2236-2239, 1997.

[60] P. K. Nanda and D. Patra, "Parallel Hybrid Tabu Search algorithm for Image Restoration," *Proc. International Conference on Communications, Devices and Intelligent Systems*, pp. 532-535, 2004.

[61] Tianzi Jiang and Fagud Yang, "An evolutionary Tabu Search for Cell Image Segmentation," *IEEE Transc. Systems, Man and Cybernetics*, vol. 32, No. 5, pp. 675-678, 2002.

[62] Samuel Pierre and Fabien Houeto, "Assigning cells to switches in cellular mobile networks using Taboo search," *IEEE Transc. on Systems,Man and Cybernetics-PartB*, vol. 32, No. 3, pp. 351-356, June 2002.

[63] M. Hasan, T. Alkhamis and J. Ali, "A comparision between simulated annealing, genetic algorithm and tabu search methods for the unconstrained quadratic Pseudo-Boolean function," *Elsevier Science Ltd. Computers and Industrial Engineering*, 38, pp. 323-340, 2000.

[64] Jong-Kae Fwu and Petar M. Djuric, "EM Algorithm for Image Segmentation initialized by a tree structure scheme," *IEEE Transc. Medical Imaging*, vol.6, No.2, pp. 349-352, Feb. 1997.

[65] Tsong-Yi Chen, Xiao-Dan Mei, Jeng-Shyang Pan and Sheng-He Sun, "Optimization of HMM by the Tabu Search algorithm," *Journal of Information Science and Engineering*, vol. 20, pp.949-957, 2004.

[66] Atam P. Dhawan, *Medical Image Analysis*, IEEE press series in Biomedical Engineering, New Jersy, Wiley Interscience 2003.

[67] Harison H. Barrett and Kyle J. Myers, "Foundations of Image Science," *Wiley Series in Pure and Applied Optics*, 2004.

[68] Joseph P. Hornak, *Encyclopedia of Imaging Science and Technology, Vol-2*, Wiley Interscience Publication, 2002, Chapter- "*Magnetic Resonance Imaging*" by Robert W. Prost, pp. 977-1002.

[69] Joseph P. Hornak, *The Basics of MRI*, Wiley Interscience Publication, 2000.

[70] Yong Yang, Xianggno Yan, Chongxun Zheng, Pan Lin, "A novel statistical method for segmentation of brain MRI," *IEEE Proc. Int. Conf. Communications,Circuits and Systems-2004*, vol. 2, 27-29 June, pp. 946-949, 2004

[71] F. Liu, S. Gao and X. Gao, "Segmentation of MR Image based on Maximum a posterior," *IEEE Proc. 23rd Annual Int. Conf. Engineering in Medicine and Biology Society*, vol. 3, pp. 2661-2664, Oct. 2001.

[72] Juin Der Lee, P. E. Cheng, M. Liou, "MR brain Image segmentation by adaptive mixture distribution," *Proc. 9th Int. Conf. on Neural Information Processing 2002*, vol. 1, pp. 216-218, 18-22 Nov. 2002.

[73] Choong Leon Tan and Jagath C. Rajapakse, "Bayesian tissue segmentation on multi spectral brain images," *Proc. 9th Int. Conf. on Neural Information Processing 2002*, vol. 1, pp. 206-210, 18-22 Nov. 2002.

[74] S. A. Hojjatoleslami and F. Kruggel, "Segmentation of large brain lesions," *IEEE Transc. Medical Imaging*, vol. 20, No. 7, pp. 666-669, July 2001.

[75] Akin Pitiot, Herve Delingette, Paul M. Thompson and Nicholas Ayache, "Expert knowledge-guided segmentation system for brain MRI," *NeuroImage*, vol. 23, pp. S85-S96, 2004.

[76] C. Tsai, B. S. Manjunath and R. Jagdeesan, "Automated segmentation of brain MR images," *Pattern Recognition*, vol. 28, No. 12, pp. 1825-1837, 1995.

[77] Jussi Tohka, Alex Zijdenbas and Alan Evans, "Fast and robust parameter estimation for statistical partial volume models in brain MRI," *NeuroImage*, vol. 23, pp. 84-97, 2004.

[78] Mara Cercignani, Matilde Inglese, Malgorzata Sigor-Zajdel, Massimo Filippi, "Segmenting brain white matter, gray matter and cerebro-spinal fluid using diffusion tenson-MRI derived indicies," *Magnetic Resonance Imaging*, vol. 19, pp. 1167-1172, 2001.

[79] Miguel Angel Gonzalez Ballester, Andrew Zisserman, Michael Brady, "Segmentation and measurements of brain stuctures in MRI including confidence bounds," *Medical Image Analysis*, vol. 4, pp. 189-200, 2000.

[80] Gabor Szekely, Andras Kelemen, Christian Brechbuhler and Guido Gerig, "Segmentation of 2-D and 3-D objects from MRI volume data using constrained elastic deformations of flexible Fourier Contour and surface models," *Medical Image Analysis*, vol. 1, No. 1, pp. 19-34, 1996.

[81] Jing-Hao Xue, Su Ruan, Bruno Moretti, Marinette Revenu and Daniel Bloyet, "Knowledge-based segmentation and labeling of brain structures from MRI images," *pattern Recognition Letters*, vol. 22, pp. 395-405, 2001.

[82] Su Ruan, Bruno Moretti, Jalal Fadili and Daniel Bloyet, "Fuzzy Markovian Segmentation in Application of Magnetic Resonance Images," *Computer Vision and Image Understanding*, vol. 85, pp. 54-69, 2002.

[83] Zu. Y. Shan, Jing Z. Liu, Guang H. Yue, "Automated human frontal lobe identification in MR images based on fuzzy-logic encoded expert anatomic knowledge," *Magnetic Resonance Imaging*, vol. 22, pp. 607-617, 2004.

[84] James D. Christensen, "Normalization of brain magnetic resonance images using histogram even-order derivative analysis," *Magnetic Resonance Imaging*, vol. 21, pp. 817-820, 2003.

[85] Chris A.Cocosco, Alex P. Zijdenbos, Alan C. Evans, "A fully automatic and robust brain MRI tissue classification method," *Medical Image Analysis*, vol. 7, pp. 513-527, 2003.

[86] Jagath C. Rajapakse and Frithjof Kruggel, " Segmentation of MR images with intensity inhomogeneities," *Image and Vision Computing*, vol. 16, No. 3, pp. 165-180, March. 1998.

[87] Jose J. Amador, "Markov random field approach to region extraction using Tabu search," *Journal of Visual Communication and Image Representation*, vol. 16, No. 2, pp. 134-158, April 2005.

[88] Ziji Wu, Keith D. Paulsen and John M. Sullivan Jr., "Adaptive model initialization and deformation for automatic segmentation of T1-weighted Brain MRI data," *IEEE Transc. on Biomedical Engineering*, vol. 52, No. 6, pp. 1128-1131, June 2005.

[89] Dzung L. Pham, jerry L. Prince, "An adaptive fuzzy c-means algorithm for image segmentation in the presence of intensity inhomogeneities," *Pattern Recognition Letters*, vol. 20, pp. 57-68, 1999.

[90] L. Q. Zhou, C. Bergot, A. M. Laval-Jeantet, V. Boussan, J. D. Laredo, M. Laval-Jeantet, "A method of radio frequency inhomogeneity correction for brain tissue segmentation in MRI," *Computerized Medical Imaging and graphics*, vol. 25, pp. 379-389, 2001.

[91] Morgan Alexander, *Solving polynomial systems using continuation for Engineering and Scientific problems*, Englewood Cliffs: Prentice-Hall, 1987.

[92] N. Chow, J. Mallet-Paret and J. A. Yorke, "Finding zeros of maps: homotopy methods that are constructive with probability one," *Math. Computation*, vol. 32, No. 143, pp. 887-899, 1978.

[93] V. L. Stonick and S. T. Alexander, "A Relationship between recursive least sqare update and homotopy continuation methods," *IEEE Trans. Signal Processing*, vol. 39, No. 2, pp. 530-532, 1991.

[94] James S. Duncan and Nicholas Ayache, "Medical Image Analysis: Progress over Two Decades and the Challenges Ahead," *IEEE Trans. Pattern Analysis and Machine Intelligence*, vol. 22, No. 1, pp. 85-106, 2000.

[95] Yongyue Zhang, Michael Brady and Stephen Smith, "Segmentation of brain MR images through a hidden Markov random field model and the Expectation-Maximization algorithm," *IEEE Trans. Medical Imaging*, vol. 20, No.1, pp. 45-57, 2001.

[96] D. B. Gu and J. X. Sun, "EM Image Segmentation Algorithm based on an inhomogeneous hidden MRF model," *IEE Proc. Vis. Image Signal Processing*, vol. 152, No. 2, pp. 184-190, April 2005.

[97] M. Y. Siyal and Lin Yu, "An intelligent modified fuzzy c-means based algorithm for bias estimation and segmentation of brain MRI," *Pattern Recognition Letters*, vol. 26, pp. 2052-2062, 2005.

[98] M. Prastawa, J. H. Gilmore, W. Limand and G. Gerig, "Automatic segmentation of MR images of the developing newborn brain," *Medical Image Analysis*, vol. 9, pp. 457-466, 2005.

[99] W. M. Wells, W. E. L. Grimson, R. Kikinis, F. A. Jolesz, "Adaptive Segmentation of MRI Data," *IEEE Trans. Medical Imaging*, vol. 15, pp. 429-442, Aug. 1996.

[100] K. Held, E. R. Kops, B. J. Krause, W. M. Wells III, R. Kikinis, H. W. M. Gartner, "Markov Random Field Segmentation of Brain MR Images," *IEEE Trans. Medical Imaging*, vol. 16, pp. 878-886, Dec. 1997.

[101] R.Guillemaud and Michael Brady, "Estimating the Bias Field of MR Images," *IEEE Trans. Medical Imaging*, vol. 16, pp. 238-251, June. 1997.

[102] J. L. Marroquin, B. C. Vemuri, S. Botello, F. Calderon, A. F. Bouzas, "An Accurate and Efficient Bayesian Method for Automatic Segmentation of Brain MRI," *IEEE Trans. Medical Imaging*, vol. 21, No. 8, pp. 934-945, 2002.

[103] J. H. Xue, A. Pizurica, W. Philips, E. Kerre, R. V. D. Walle, I. Lemahieu, "An Integrated method of Adaptive Enhancement for Unsupervised Segmentation of MRI Brain Images," *Pattern Recognition Letters*, vol. 24, pp. 2549-2560, 2003.

[104] Z. Chaozhe and T. Jiang, "Multicontext fuzzy clustering for separation of brain tissues in magnetic resonance images," *Neuroimage*, vol. 18, No. 3, pp. 685-696, 2003.

[105] B. Johnston, M. S. Atkins, B. Mackiewich and M. Anderson, "Segmentation of multiple sclerosis lesions in intensity corrected multispectral MRI," *IEEE Transc. Medical Imaging*, vol. 15, pp. 154-169, Apr.1996.

[106] B. Dawant, A. Zijidenbos and R. Margolin, "Correction of intensity variations in MR images for computer-aided tissue classification," *IEEE Transc. Medical Imaging*, vol. 12, pp. 770-781, Dec. 1993.

[107] J. Bezdek, L. hall and L. Clarke, "Review of MR image segmentation techniques using Pattern recognition," *Medical Physics*, vol. 20, pp. 1033-1048, 1993.

[108] D. A. G. Wicks, G. J. Barker and P. S. Tofts, "Correction of intensity nonuniformity in MR images of any orientation," *Magnetic Resonance Imaging*, vol. 11, pp. 183-196, 1993.

[109] Koen Van Leemput, Frederik Maes, Dirk Vander meulen and Paul Suetens, "Automated model based bias field correction of MR Images of the Brain," *IEEE Trans. Medical Imaging*, vol. 18, No. 10, pp.885-896, Oct.1999.

[110] Koen Van Leemput, Frederik Maes, Dirk Vander meulen and Paul Suetens, "Automated model based tissue classification of MR Images of the Brain," *IEEE Trans. Medical Imaging*, vol. 18, No. 10, pp.897-908, Oct.1999.

[111] T. Taxt and A. Laundervold, "Multispectral analysis of the brain using Magetic Resonance Imaging," *IEEE Trans. Medical Imaging*, vol. 13, pp.470-481, 1994.

[112] M. N. Ahmed, S. M. Yamany, A. A. Farag and T. Moriarty, "Bias field estimation and adaptive segmentation of MRI data using a modified Fuzzy C-means algorithm," *Proc.IEEE Int. Conf. Computer Vision and Pattern Recognition*, vol. 1, Fort Collins, CO, pp.250-255, June 1999.

[113] M. N. Ahmed, S. M. Yamany, Nevin Mohamed, A. A. Farag and T. Moriarty, "A modified fuzzy C-means algorithm for bias-field estimation and segmentation of MRI data," *IEEE Trans. Medical Imaging*, vol. 21, No. 3, pp. 193-199, Mar. 2002.

[114] P. K. Nanda and D. Patra, "Image Segmentation using Parallel Tabu Search Algorithm and MRF Model," *Proceedings of National Conference on Communications (NCC-2005)*, pp. 336-340, 2005.

[115] P. K. Nanda, D. Patra and A. Pradhan, "Brain MR Image Segmentation using Tabu Search and Hidden Markov Random Field Model," *Proceedings of 2nd Indian International Conference on Artificial Intelligence (IICAI-05)*, pp. 3143-3160, 2005.

[116] Richard S.Snell, *Clinical Anatomy by Systems*, Lippincott Willians & Wikins, June 2003.

[117] K.O.Lim and A.Pfefferbaum, "Segmentation of MR brain images into cerebrospinal fluid spaces, white and gray matter," *Jounal of Computer Assisted Tomography*, vol. 13, No. 4, 1989.

[118] Tim Mclnerney and Demetri Terzopoulos, "Deformable models in Medical Image Analysis," *IEEE Proceedings of Mathematical Methods in Biomedical Image Analysis*, pp. 171-180, 1996.

[119] T.Ernst, R.Kreis and B.D.Ross, "Absolute Quantitation of Water and Metabolites in the Human Brain; Compartments and Water," *Journal of Magnetic Resonance Ser. B*, vol. 102, No. 1, pp.1-8, 1993.

[120] P.K.Nanda, P.G.Poonacha and U.B.Desai, "A supervised image segmentation scheme using MRF model and homotopy continuation method," *Proceedings of Indian Conference on CVGIP'98*, pp. 15-20, 1998.

[121] P.K.Nanda, K.Sunil Kumar, S.Ghokale, U.B.Desai, "A multiresolution approach to color image restoration and parameter estimation using homotopy continuation method," *Proceedings of ICIP'95*, pp. 2045-2048, 1995.

[122] K.Sunil kumar, U.B.Desai, "Joint segmentation and image interpretation," *Pattern Recognition*, vol. 32, No. 4, pp. 577-589, 1999.